UNIVERSITAET HAMBURG
FACHBEREICH PHYSIK

Pulsed Electrodeposited p- and n-Doped Chalcogenide Semiconductors for Thermoelectric Applications: From Films to Nanowires

Dissertation zur Erlangung des Doktorgrades des Fachbereichs Physik der Universitaet Hamburg

vorgelegt von

Christian Schumacher

aus Minden (Westf.)

Hamburg

2012

revievers of the dissertation:	Prof. Dr. Kornelius Nielsch Prof. Dr. Peter Woias
reviewers of the disputation:	Prof. Dr. Kornelius Nielsch JP Dr. Julien Bachmann
date of the disputation:	25.05.2012
head of the examinations board:	Prof. Dr. Hans-Peter Oepen
head of the promotion board:	Prof. Dr. Peter Hauschildt
dean of the department:	Prof. Dr. Heinrich Graener

0.1 Abstract

In this work, a comprehensive study of thermoelectric chalcogenide materials is presented and the systematic optimization of n-type Bi_2Te_3, p-type Sb_2Te_3 and their ternary compounds is performed. Thermoelectric films and nanowires are synthesized by potentiostatic electrodeposition on Au/Pt, stainless steel substrates and in AAO membranes. The influence of the preparative parameters such as the composition of the electrolyte bath and the deposition potential is investigated in a nitric acid solution. A novel deposition method is developed using millisecond potentiostatic pulses, which improves both the morphology and the composition of the material.
As a post-deposition step, the influence of annealing is investigated. The optimized p-doped $(Bi_xSb_{1-x})_2Te_3$ and the n-doped $Bi_2(Te_xSe_{1-x})_3$ materials are annealed for a period of about 1 h under helium atmosphere and also under tellurium atmosphere at 550 K for 60 h. The samples are characterized in terms of composition, crystallinity, Seebeck coefficient, thermal and electrical resistivity. p-Doped pulsed deposited films exhibit Seebeck coefficients up to approximately $+160$ μV K^{-1} (Sb_2Te_3) and $+208$ μVK^{-1} ($(Bi_xSb_{1-x})_2Te_3$). For the n-doped films, approximately -100 μVK^{-1} (Bi_2Te_3) and -130 μVK^{-1} ($Bi_2(Te_xSe_{1-x})_3$) are achieved. Power factors and ZT values of up to 1325 $\mu Wm^{-1}K^{-2}$ (ZT 0.4) and 825 $\mu Wm^{-1}K^{-2}$ (ZT 0.25) are realized at room temperature.

0.2 Zusammenfassung

In der vorliegenden Arbeit wird eine systematische Studie ueber die Herstellung thermoelektrischer Chalkogenid-Materialien mittels elektrochemischer Abscheidung praesentiert. Dabei wird die Fabrikation von sowohl n-, als auch p-dotierten Halbleitern auf Bi_2Te_3-Basis auf Au/Pt, sowie Stahlsubstraten und in poroese AAO Membranen untersucht. Die abgeschiedenen Materialien in Form von Filmen und Nanowires werden dabei hinsichtlich Ihrer thermoelektrischen Eigenschaften, wie Seebeck Koeffizient, sowie elektrische und thermische Leitfaehigkeit hin optimiert.Dabei wird der Einfluss von Parametern wie der Zusammensetzung des verwendeten Elektrolytbades, des verwendeten Abscheidepotentiales, sowie der elektrochemischen Abscheidemethode (DC, konstant) untersucht. Die optimierte gepulste Abscheidung im Millisekundenbereich fuehrt dabei zu einer deutlichen Verbesserung hinsichtlich Morphologie und Zusammensetzung der abgeschiedenen Materialien.
Wesentliche Verbesserungen der thermoelektrischen Eigenschaften koennen zudem durch optimierte thermische Behandlung der abgeschiedenen Schichten erreicht werden. Dabei werden die elektrochemisch abgeschiedenen Schichten unter He oder Te Atmosphaere bei ca. 550 K ueber einen Zeitraum von bis zu 60 h annealt. Die Proben werden hinsichtlich ihrer chemischen Zusammensetzung, Kristallinitaet und Transportparameter hin charakterisiert und die thermoelektrische Leistungsfaehigkeit bestimmt. P-dotierte Filme erreichen dabei Seebeck Koeffizienten von ca. $+160\ \mu V\ K^{-1}$ (Sb_2Te_3) und $+208\ \mu V\ K^{-1}$ ($(Bi_xSb_{1-x})_2Te_3$) - n-dotierte Materialien $-100\ \mu VK^{-1}$ (Bi_2Te_3) and $-130\ \mu VK^{-1}$ ($Bi_2(Te_xSe_{1-x})_3$). Power Faktoren und ZT Werte von bis zu $1325\ \mu Wm^{-1}K^{-2}$ (ZT 0.4) und $825\ \mu Wm^{-1}K^{-2}$ (ZT 0.25) werden dabei erreicht.

Contents

Chapter 1

Motivation

During the past two decades, the advantages of thermoelectricity have become more interesting for various kinds of applications. Due to the presence of extensive waste heat sources and due to manufacturing trends such as the abdication of moving parts, the interest in the development of thermoelectric generators has quickly increased. The principles of thermoelectricity are simple, the components can be scaled up easily to any kind of demand and the durability as well as the reliability are on a high level. Thermoelectricity not only is used for energy harvesting, but also for the cooling of highly sensitive electronic components, but most famous applications for thermoelectric generators (TEG) have been extraterrestrial space missions such as NASA's "Cassini" (fig. 1.1 (a)). With this application, the demand for a continuously working electrical power source has been realized by a TEG powered by a radionuclide as a heat source. Although the generator could prove its reliability during several missions, to date, the low efficiency of thermoelectric materials has inhibited the broad use of TEGs for energy harvesting.

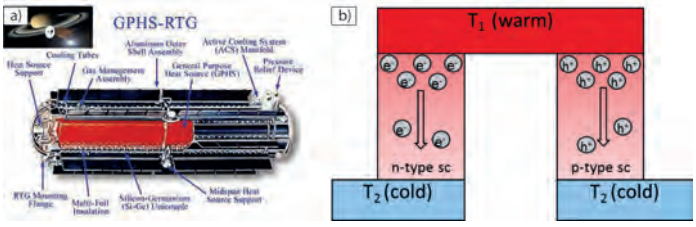

Figure 1.1: (a) "Cassini" mission, inlay: illustration of the radionuclide thermoelectric generator [DoE 1990a]; (b) illustration of semiconductor thermocouple

Due to their peak performance between 300-400 K, both p- and n-doped

semiconductors are of high interest for thermoelectric applications at room temperature (compare fig. 1.1 b).
Since several methods are available to fabricate such thermoelectric semiconductor materials, the advantages and disadvantages of some of them should be pointed out in more detail. Best results in terms of material quality are obtained by fabrication from the gaseous phase. Thus, methods such as molecular beam epitaxy (MBE) and atomic layer deposition (ALD) are commonly accepted, since they exhibit good control over process parameters and materials' attributes such as the chemical composition and crystal structure. The thermoelectric performance is well defined and of high standard.
Due to high costs of these high-vacuum based methods, low-cost alternatives with comparable quality are of particular interest. Thus, electrodeposition of the materials may offer a convenient alternative to easily realize the production of high-quality thermoelectric materials.

The main advantages of the electrochemical deposition of thermoelectric materials are the comparably facile control over process parameters and low costs due to the absence of high-vacuum systems, deposition at room temperature and relatively simple technical requirements. Electrodeposited materials such as these Bi_2Te_3-based compounds can be integrated into commercialized microdevices. Particularly, the electrodeposition of Bi_2Te_3 films [BBC$^+$09] [MBL96] [LTS$^+$06] and nanostructures [PSMG$^+$01] [JXJ$^+$04] [SGSS03] [MBL$^+$06] [LJW09] is well reported in the literature. Most references report that electrodeposited Bi_2Te_3 is typically obtained in n-doped form. Even though the type of doping theoretically also can be of p-type, that has been reported exclusively by Glatz et al.[GSDH09] In order to make the deposited materials applicable to energy harvesting of waste heat, a second, p-doped material is necessary for implementation into a thermoelectric generator.[SGDH08] The knowledge base on electrochemically deposited Sb_2Te_3 as corresponding p-type material is not as extensive by far, but also of high interest, because of the possibility to combine both materials for generator use. Sb_2Te_3 is isostructural with Bi_2Te_3 (R3m) whereby the Bi lattice sites are occupied by Sb.[XHY$^+$08] The preparation of electrolytes is more difficult due to lower solubility of antimony ions in aqueous solutions.[Lid92] [Che11] Furthermore, the deposition process is challenging due to lesser driving force for the formation of Sb_2Te_3 compared to Bi_2Te_3, since the binding energy is significantly lower.[SRA$^+$12] Nevertheless, the deposition of Sb_2Te_3 also is of high interest, since this material could act as a dopant for Bi_2Te_3 compounds in order to form p-doped ternary chalcogenide compounds.[SS59] The deposition of polycrystalline films on indium tin oxide (ITO) substrates was first reported by Leimkuehler et al. from a

HCl-based electrolyte bath at pH 4.25 with a focus on the structural analysis of the films.[LKRK02] The preparation of Sb_2Te_3 films from solutions based on perchloric acid was reported by Del Frari et al., whereby a satisfactory control of the film composition was achieved.[FDS+05] However, power factors were found to be dependent on the length of the deposition pulses ("on"-time). Pulse times in the range of 3-9 s were investigated and the best results were found for short times. Electroplating of $(Bi_{1-x}Sb_x)_2Te_3$ films using electrolytes based on nitric acid was reported by Martin-Gonzales et al. and the deposition mechanism was found to be similar to that of Bi_2Te_3.[MGSP+03] The Seebeck values of as-deposited films were reported to be in the range of 20-55 μVK^{-1} with power factors of up to 200 $\mu Wm^{-1}K^{-2}$, i.e. 10 % of bulk values. Annealing of the films led to moderate increases in performance (decrease of sheet resistance down to 10 % of the initial value) [KO09],[JPL+10],[PXY+09]. Seebeck coefficients of up to 250 μVK^{-1} were reported for (amorphous) materials deposited with diaminourea polymer (DAUP) and uniaxial pressing as post-treatment process with low electrical conductivity causing also relatively low power factors [LKO09] [KO10] [QYZ+11].

Several works report on the fabrication of $(Bi_xSb_{1-x})_2Te_3$ using various deposition methods such as pulsed laser deposition (PLD) [KAY+11] or solution growth.[SOV+10] It exhibits the same crystal structure as Bi_2Te_3 with Sb atoms randomly occupying the Bi lattice places, forming a different type of doping causing higher thermoelectric performances.[XHY+08] Many previous works also report on the electrodeposition of $(Bi_xSb_{1-x})_2Te_3$, although the deposition process is more challenging compared to binary compounds due to limited control of the film composition by the deposition potential or charge density. The simultaneous control of three materials during the deposition requires the optimization of the electrolyte more carefully. However, a successful deposition was reported by several groups. Del Frari et al. reported the deposition of $(Bi_xSb_{1-x})_2Te_3$ films from solutions based on perchloric acid on stainless steel disks.[FDS+05] The results indicated good control over the films compositions, but poor control of the films morphology. Thermoelectric performance was reported in later works, exhibiting Seebeck coefficients up to +180 μVK^{-1} after annealing for about 1 h in argon atmosphere.[DFDS+06] Potentiostatic electrodeposition from electrolytes based on nitric acid with tartaric acid in order to increase the solubility of Sb in the aqueous solutions was reported by Xiao et al.[XYLM07] Works by Tittes et al. [TP07] and in 2008 of Li et al. [LSZ+08] report on the successful deposition of $(Bi_xSb_{1-x})_2Te_3$ films, but they lack the thermoelectric characterization of the deposited materials. Nedelcu et al. and Li et al

(2009) reported on $(Bi_xSb_{1-x})_2Te_3$ films with Seebeck coefficients of +150 μVK^{-1} and +119 μVK^{-1} and power factors of 322 $\mu WK^{-2}m^{-1}$ and 112 $\mu WK^{-2}m^{-1}$, respectively. The knowledge of the electrochemical deposition of the corresponding ternary n-doped material, $Bi_2(Te_xSe_{1-x})_3$ is not extensive by far, but also of high interest in order to combine both ternary materials, e.g. for generator use. However, some works already reported on the deposition of this thermoelectric material. Michel et al. deposited $Bi_2(Te_xSe_{1-x})_3$ thin films and concluded that the key factor of the deposition is the electrolyte composition as well as the deposition potential.[MSS+03] Films deposited by Bu et al. on Au and stainless steel substrates exhibited strongly preferred orientations in (110) direction.[BWW07] [BWW08] However, also these works lack the thermoelectric characterization of the deposited films. In a later work, Michel et al. followed up with up the electrical characterizations by reporting thermopowers of $-70/-150$ μVK^{-1}.[MDS+08] Consistent with this, Zimmer et al. deposited $Bi_2(Te_xSe_{1-x})_3$ with a Te:Se -Ratio of 10:1 and Seebeck coefficients of -40 μVK^{-1} and Martin-Gonzales et al. reported about thermopowers between -40 to -55 μVK^{-1} for nanowires and films. [ZSTB07], [MGSP+03] Very few of these works report on annealing treatments on the electrochemically deposited materials $(Bi_xSb_{1-x})_2Te_3$ and $Bi_2(Te_xSe_{1-x})_3$.

Since the thermal treatment of as-deposited samples can achieve significant improvements due to a decrease in structural defects [LSZ+08], in this work, samples fabricated over a wide range of deposition potentials are annealed in He atmosphere during in situ XRD measurement for structural analysis. In order to further improve the thermoelectric performance of the films, the materials were annealed for 60 h at 250 °C in an equilibrium Te atmosphere, since this treatment proved its ability to improve the stoichiometry of V-VI in semiconductors.[RSW11]

In this work, the development and synthesis of high-performance chalcogenide semiconductors based on reported knowledge on the electrochemical deposition of Bi_2Te_3 is presented. Not only it is the ambition to synthesize and optimize materials with a significantly improved thermoelectric performance, but also to develop both n-doped and p-doped ternary materials, which are ready to be integrated to thermoelectric applications such as microstructured thermogenerators. In addition, the materials should be manufacturable at low costs and their geometry should be customizable to any kind of applications, thus also the upscaling of the materials should be proven.
The development of suitable electrolyte baths and substrates is performed first in chapt. 3. In order to optimize the chemical and physical proper-

ties, the deposited materials are characterized systematically using various characterization methods, which are presented in chapt. 4.
These methods are used in order to optimize both the n-doped and the p-doped binary and ternary materials in chapt. 5 and 6. Further optimization of the materials' quality is achieved subsequently by the thermal treatment of the electrodeposited materials in He and Te equilibrium atmosphere reported in chapt. 7.
The optimized materials are then used for the deposition of nanostructured wires with diameters ranging from 80 to 200 nm (chapt. 8). The nanostructured materials exhibit an improved thermoelectric performance in terms of electrical conductivity and higher thermoelectric power factors. The nanowires are characterized using single nanowire measurements reported in chapt. 8. A compendium followed by a concept of perspectives will conclude the work in chapt. 9.

Chapter 2

An Introduction into Thermoelectrics and Electrochemistry

In order to understand about the complex conditions of the thermoelectric materials, the basic principles and correlations of transport parameters contributing to the thermoelectric performance are presented. Figure 2.1 shows the principle of the Seebeck effect: As long as two (semi)conductors have two common contacts with a temperature difference ΔT between both contacts, they exhibit a potential difference V, which is dependent on ΔT [Row06].

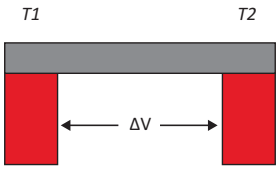

Figure 2.1: Seebeck effect

The differential Seebeck coefficient S is defined as the ratio of ΔV to ΔT [Gol09]:

$$S = \frac{\Delta V}{\Delta T} \tag{2.1}$$

Since the charge carriers within the conductor will have a higher velocity with increasing temperature, the velocity distribution of carriers (electrons or holes) exhibits higher values for particles located at the hot junction of the conductors. Therefore, there will be a continuous diffusion of carriers to the colder junction, causing an electromotive force that

tends to generate an electric current from the hot to the cold junction. Conversely to this, a current forced by an external source will cause heating at one and cooling at the other junction of the conductors. This is named the Peltier effect and can be quantified by:

$$\Pi = \frac{Q}{It} \tag{2.2}$$

with the heat affiliated/set out at the junctions Q, the electrical current I and the duration of the current t. The Peltier effect often becomes important in case of cooling sensitive electronic components by the cold side of a thermoelectric module. Since the Seebeck effect is reverse to the Peltier effect, it alternatively can be described with the Kelvin equation

$$S = \frac{\Pi}{T}. \tag{2.3}$$

These effects appear at all types of conductors, but increase significantly for semiconductors, making them the main focus of investigations in the field of thermoelectrics. In order to analyze the differences, one must understand the principles of the electrical transport mechanism of such materials [Gol09]. The interactions of electrons and periodic lattice structures within a crystal are important for the investigation of the differences between conductors, semiconductors and isolators. It is well known that the energy of electrons has to be within "energy-bands", which exhibit discrete levels with gaps in between. The Fermi distribution reports on the chance of an electron state E to be occupied by

$$F_0(E) = [1 + \exp(\frac{E - E_f}{k_B T})]^{-1} \tag{2.4}$$

with the Fermi energy E_f and the Boltzmann constant k. Since the Fermi energy depends on the temperature T, the probability $F(E)$ also changes with T, exhibiting values of 0 for $T = 0K$ and at $T > 0$ at the Fermi level it is $\frac{1}{2}$. To calculate the number n of occupating electrons of a certain energy level, $F(E)$ has to be multiplied by the density of states $G(E)$, which depends on the position within the band structure:

$$n = \int_0^\infty G(E) F_0(E) dE \tag{2.5}$$

$$n = \int_0^\infty G(E) \frac{1}{1 + e^{\frac{E - E_f}{k_B T}}} \tag{2.6}$$

This equation for the density of charge carriers (electrons or holes) is required for the discussion of n- and p-doped semiconductors in more

detail in chapt. 5 and 6. It exhibits small values around the band edges, which significantly increase within the band. Each state is characterized by its wave function, belonging to the corresponding electron. Thus there are gaps in the energy bands which correspond to energy states "not allowed" for occupation of carriers. Crystals, that allow the electrons to move between energy levels exhibit electrical (and thermal) conductivity. Completely filled or completely empty bands do not contribute to the electrical conductivity. For metals, the Fermi level lies within the conduction band, so that a high number of electrons can easily move into vacant states, causing a high conductivity. For insulators, the Fermi level directly lies between two allowed bands, causing no free carriers in the conduction band. (Extrinsic) semiconductors also show Fermi levels within the band gap, but here it is located closer to the edge of either the conduction or the valence band. Thus, unless the total amount of carriers is relatively low, all carriers can contribute to the electrical conduction — in case of a Fermi lever near to the conduction band edge, the electrons are able to perform conduction in the conduction band. One can promote this by adding impurities (donor atoms) to the structure, which will increase the amount of negative carriers (electrons). If the Fermi level is located near the valence band, there will be empty states in the valence band, i.e. positive holes can perform conductance in the valence band. This p-doping can be induced by adding acceptor atoms to the crystal structure. If the band gap is small enough, the Fermi level is located near both the conducting and the valence band and both type of carriers can contribute to the conduction, these materials are so called intrinsic semiconductors.

Together with the electrical conductivity σ and the thermal conductivity κ, the major value, the figure of merit ZT, is defined as:

$$ZT = \frac{S^2\sigma}{\kappa}T \tag{2.7}$$

Since the electrical conductivity σ and the thermal conductivity κ are linked directly, they can not optimized separately. The Wiedemann-Franz law describes the link of these two values:

$$\frac{\kappa}{\sigma_{el}} = LT \tag{2.8}$$

with the Lorentz-number

$$L = \frac{\kappa}{\sigma T} = \frac{\pi^2}{3}(\frac{k_B}{e})^2$$

which is constant for metals, but fluctuates due to the thermal conductivity κ to be dependent on electrons and the lattice structure (phonons):

$\kappa = \kappa_{el} + \kappa_{lat}$. Thus, the main challenge of thermoelectric materials is the optimization of the ratio between electrical and thermal conductivity.

Recently, thermoelectricity has become more interesting for terrestrial applications, there is also a steadily growing interest in miniaturized thermoelectric generators for small-scale applications such as wireless sensors based on waste heat recovery. Since there are many possible applications, at which the harvesting of waste heat energy leads to significant improvements in energy yield, there also is a growing demand for different types of thermoelectric converters. Dependent on the thermoelectric material used, the conversion works best at different temperatures based on the peak performances of the particular material used (compare figure 2.2).

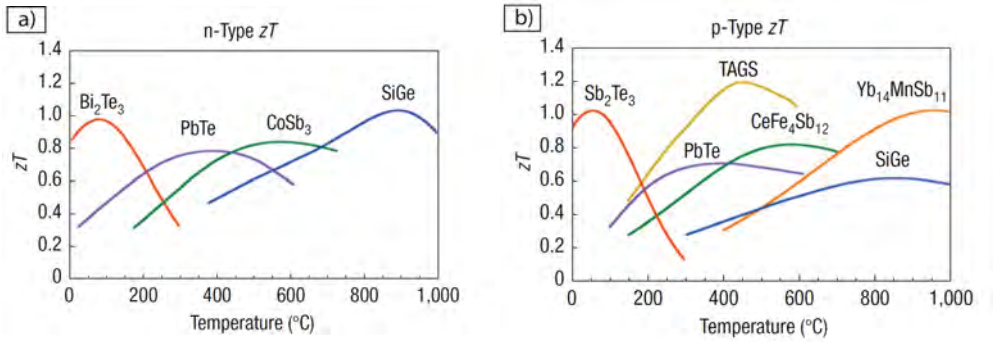

Figure 2.2: Thermoelectric Materials [ST08]

For high-temperature applications such as energy harvesting at power plants or exhaust heat converters in vehicles, materials such as Skutterudites (e.g. $CoSb_3$), SiGe alloys and $Yb_{14}MnSb_{11}$ are ideal, due to their peak performances at temperatures between 550 and 1000 °C. For applications at mid-range temperatures, thermoelectric materials such as GeTe-AgSbTe alloys (TAGS) and also lead telluride compounds work best, since their performance shows a maximum at temperatures within 300-450 °C. [Row95]
Last but not least, chalcogenide compounds not only exhibit high thermoelectric performances, they also appear at slightly elevated temperatures within 0-200 °C. Thus, Bi_2Te_3/Sb_2Te_3 based materials are highly interesting for all types of applications at room temperature, such as self-sufficient sensor networks. Such sensors are employed e.g. in medicine or aeronautical environments. Chalcogenide compounds to date are widely fabricated by multiple deposition methods, such as high-vacuum methods, e.g. molecular beam epitaxy (MBE), atomic layer deposition (ALD) or thermal co-evaporation. In contrast, the technical requirements for the electrochemical deposition of Bi_2Te_3 based compounds is not extensive by

far, but also produces high performance thermoelectric materials. Thus, the electroplating of thermoelectric materials is of high interest and worth the extensive investigations reported in this work.

In figure 2.3, the principle of the electrochemical deposition process is illustrated. The cell contains two electrodes in an electrolyte bath. The deposition of the thermoelectric material takes place at the cathode by reduction of (positive) ions in the solution.

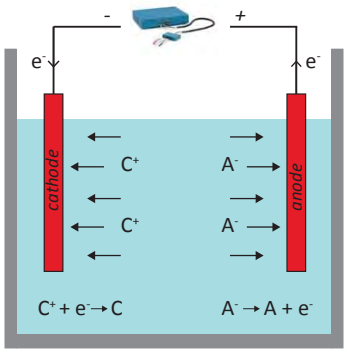

Figure 2.3: Illustration of the electrochemical deposition

Thermodynamics of solids and solutions describes the equilibrium of two chemical phases for equal chemical potentials μ_i. [Pet]

The electrochemical potential is defined as: [Pet]

$$\mu_i = \mu_i^0 + \underbrace{RT \ln a_i}_{A} + \underbrace{z_i F \varphi_i}_{B} \tag{2.9}$$

with the chemical standard potential μ_i^0. Part A of the equation is dependent on the concentration/activity a_i, part B to the charge of the ions z_i, the Farady constant F and the electrical potential φ_i. B is equal to 0 as long as the particles' charge is equal to 0.
A solid that comes in contact with a solution of its ions causes an electric current, if

$$\mu^{solid} \neq \mu^{electrolyte}.$$

Thus, electrons move from the solid to the solution and ions move from the solution to the solid until the chemical potentials are equal. Equilibrium may be reached upon application of an electrical potential difference between solid and solution:

$$\mu^{solid} = \mu^{electrolyte}$$

$$\mu^{0,solid}+RT\ln a^{solid}+zF\varphi^{solid} = \mu^{0,electrolyte}+RTlna^{electrolyte}+zF\varphi^{electrolyte}$$

$$\Delta\varphi = \varphi^{solid} - \varphi^{electrolyte}$$

$$\Delta\varphi = \frac{\mu^{0,electrolyte} - \mu^{0,solid}}{zF} + \frac{RT}{zF}\ln\frac{a^{electrolyte}}{a^{solid}} \tag{2.10}$$

This is the potential of a half-cell, but the potential difference only can be measured between two electrodes in the solution. In order to compare half cells based on different materials, the potential is defined to be measured against a standard electrode, that is defined as zero point (standard H_2 electrode).

Thus, the potential is defined as [Pet]:

$$\varphi_{M^{z+}/M} = \varphi^{solid} - \varphi^{electrolyte} = \frac{\mu^{0,electrolyte} - \mu^{0,solid}}{zF} - \frac{RT}{zF}ln\frac{a^M}{a^{M^{z+}}}$$

and with respect to the H_2 electrode:

$$\varphi_{2H^+/H_2} = 0$$

$$E = \Delta\varphi_{M^{z+}/M} - \Delta\varphi_{2H^+/H_2}$$

$$= \frac{\mu^{0,electrolyte} - \mu^{0,solid}}{zF} - \frac{RT}{zF}\ln\frac{a^M}{a^{M^{z+}}}$$

$$E = E^0 + \frac{RT}{zF}\ln a^{M^{z+}}$$

Once more than one type of ions υ_i contributes to the reaction, the equation becomes [Pet]

$$\Delta E = E_{cathode} - E_{anode} = E^0_{cathode} - E^0_{anode} - \frac{RT}{zF}\,ln\prod_i a_i^{s_i}$$

with the the coefficient of stoichiometry s, the convention E=$E_{cathode}$-E_{anode} and the free enthalpy

$$\Delta G = -zF\Delta E.$$

The half-cell potential then can be described as

$$E = E^0 + \frac{RT}{zF} \ln \frac{a_{oxidation}}{a_{reduction}} \tag{2.11}$$

With this so called Nernst equation, the potential/energy of reduction or oxidation processes can be calculated for given reactants. (compare calculations made for Bi/Sb/Te in chapt. 3).

Chapter 3

Synthesis

The deposition of all thermoelectric materials investigated and reported in this work is described subsequently. Some contents of this chapter have already recently been published by the author. In order to deposit the materials as films and nanostructures, at first, the deposition process of the particular materials has to be developed. Therefore, the electrolyte baths and deposition conditions for all binary and ternary Bi_2Te_3 alloys have been optimized.

3.1 Electrolyte Baths

The electrolytes used for the electrochemical deposition of the films and nanostructures are aqueous solutions based on 1M nitric acid. Concentrated nitric acid (Merck 69 %) is diluted with clean water (18.2 MO-cm 25 °C, TOC: <10 ppb) until the solution contains 1 M nitric acid. The antimony, tellurium and selenium salts are subsequently dissolved in the acidic solution, tentatively heated up to around 70 °C in order to increase the solubility of the salts.

3.1.1 Bi_2Te_3

The thermoelectric materials used here are based on Bi_2Te_3, since this material has been reported extensively in the literature (compare chapt. 2). Bismuth(III) nitrate pentahydrate $Bi(NO_3)_3 + 5H_2O$ (Sigma Aldrich, 99.999 %) is dissolved in 1 M nitric acid at room temperature. Tellurium-oxide TeO_2 (Sigma Aldrich, 99.995 %) is dissolved subsequently in the solution.
The cyclovoltamogramm displayed in Fig. 3.1 indicates a sharp peak for the deposition of Bi_2Te_3 at a potential more negative than −80 mV vs. a AgAgCl reference electrode (KCl saturated). In order to explain

the differences in energy of both the formation of Bi_2Te_3 and Sb_2Te_3 (compare chapt. 3.1.2), the formation energy of elementary Bi and Te is calculated here.[MGPG+02] One has to keep in mind, that this is not the calculation of the real chemical reaction, since the formation here starts with $Te^{(2-)}$. The external potential applied by the potentiostat is used to transform the existing $Te^{(4+)}$ to $Te^{(2-)}$ first. Then the formation to Bi_2Te_3 takes place:

$$Bi^{3+} + 3e^- \rightharpoonup Bi, \Delta E^0 = 0.308V, \text{and}$$

$$Te^{2-} \rightharpoonup Te + 2e^-, \Delta E^0 = 1.143V^{[\text{Lid92}]}.$$

$$\Rightarrow 2Bi^{3+} + 3Te^{2-} \rightharpoonup 2Bi + 3Te,$$

where

$$\Delta G^0 = -nF\Delta E^0 = -6 \cdot 10^5 \frac{\text{C}}{\text{mol}} \cdot (0.308 + 1.143)V = -870.6 \frac{\text{kJ}}{\text{mol}}.$$

From the elements, the formation of Bi_2Te_3 starts:

$$2Bi + 3Te \rightharpoonup Bi_2Te_3, \Delta G^0 = -899,1 \frac{\text{kJ}}{\text{mol}}$$

combined in one reaction equation:

$$2Bi^{3+} + 3HTeO_2^+ + 9H^+ + 18e^- \rightharpoonup Bi_2Te_3(solid) + 6H_2O, \qquad (3.1)$$

where

$$\Delta G^0 = (-870 - 899,1) \frac{\text{kJ}}{\text{mol}} = -1770 \frac{\text{kJ}}{\text{mol}}$$

Since this energy is high compared to the deposition of other chalcogenide compounds (compare deposition of Sb_2Te_3), here the deposition mechanism is very likely to produce one phase of stoichiometric Bi_2Te_3. Therefore, the electrochemical deposition of Bi_2Te_3 starts with respect to eq. 3.2 at potentiostatic deposition potentials more negative than -120mV vs. AgAgCl (compare fig. 3.1). At more negative reduction potentials than -450 mV, the evolution of hydrogen starts.

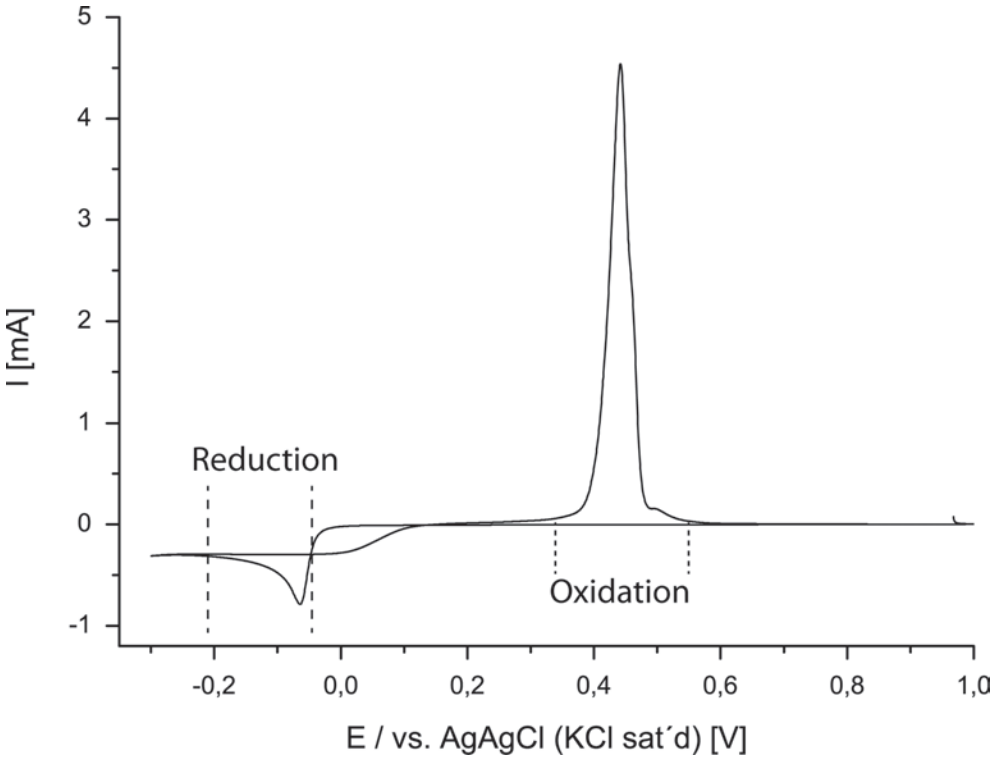

Figure 3.1: Cyclic voltammogram of the Bi_2Te_3 electrolyte containing 0.0075 $\frac{\text{mol}}{\text{L}}$ of $Bi(NO_3)_3 + 5H_2O$ and 0.01 $\frac{\text{mol}}{\text{L}}$ of TeO_2 in 1 M nictric acid at a scan speed of 20 $\frac{\text{mV}}{\text{s}}$.

3.1.2 Sb_2Te_3

The nitric acid solution is separated into two solutions. Tellurium-oxide TeO_2 (Sigma Aldrich, 99.995 %) is dissolved in the first acidic solution similarly than before with the preparation of Bi_2Te_3. Tartaric acid powder ($C_4H_6O_6$) (VWR, L(+)-tartaric acid for analysis) is dissolved in the second solution with subsequently dissolving Sb_2O_3 (Sigma Aldrich, 99.999 %) causing the tartaric acid to act as a complexing agent in order to solve the antimony, although the solubility of Sb-III-salts in aqueous solutions is low.[SRA+12] In case the salts are likely to precipitate from the solution, the solution is heated up to around 70 °C with agitating the solution using a magnetic stirrer. Afterwards, both solutions are mixed. The formation energy of Sb_2Te_3 can be calculated here. One should keep in mind, that this calculation does not correspond to the real chemical reaction (compare chapt. 3.1.1):

$$SbO^+ + 2H^+ + 3e^- \rightharpoonup Sb + H_2O, \Delta E^0 = 0.212V^{[\text{AB02}]}, and$$

$$Te^{2-} \rightharpoonup Te + 2e^-, \Delta E^0 = 1.143V^{[\text{Lid92}]}.$$

$$\Rightarrow 2Sb^+ + 4H^+ + 3Te^{2-} \rightharpoonup 2Sb + 3Te + 2H_2O,$$

where

$$\Delta G^0 = -nF\Delta E^0 = -6 \cdot 10^5 \frac{\text{C}}{\text{mol}} \cdot (0.212 + 1.143)V = -813.0 \frac{\text{kJ}}{\text{mol}}.$$

From the elements, the formation of Sb_2Te_3 starts:

$$2Sb + 3Te \rightharpoonup Sb_2Te_3, \Delta G^0 = -58.35 \frac{\text{kJ}}{\text{mol}}^{[\text{AB02}]}$$

combined in one reaction equation:

$$2SbO^+ + 4H^+ + 3Te^{2-} \rightharpoonup Sb_2Te_3(solid) + 2H_2O, \tag{3.2}$$

where

$$\Delta G^0 = (-813 - 58.35) \frac{\text{kJ}}{\text{mol}} = -871.35 \frac{\text{kJ}}{\text{mol}}$$

Since this energy is significantly lower than the corresponding value for the deposition of Bi_2Te_3, the formation non stoichiometric Sb_2Te_3 compounds and pure Sb and Te phases is more likely. Thus, the reduction peak is less sharp compared to Bi_2Te_3. The deposition starts at potentials more negative than −220 mV vs. AgAgCl (fig. 3.2).

3.1.3 $(Bi_xSb_{1-x})_2Te_3$

The ternary $(Bi_xSb_{1-x})_2Te_3$ compound is very similar to the corresponding binary compound Sb_2Te_3, but with donator atoms of Bi randomly occupying the lattice sites of Sb. [Row95] Thus, the fabrication of the electrolyte is related to the fabrication of the electrolyte for the deposition of Sb_2Te_3 above, although a certain content of Bi^{3+} atoms is added to the solution. However, since the deposition of three elements in parallel is more complicated, the optimization of the electrolyte is much more

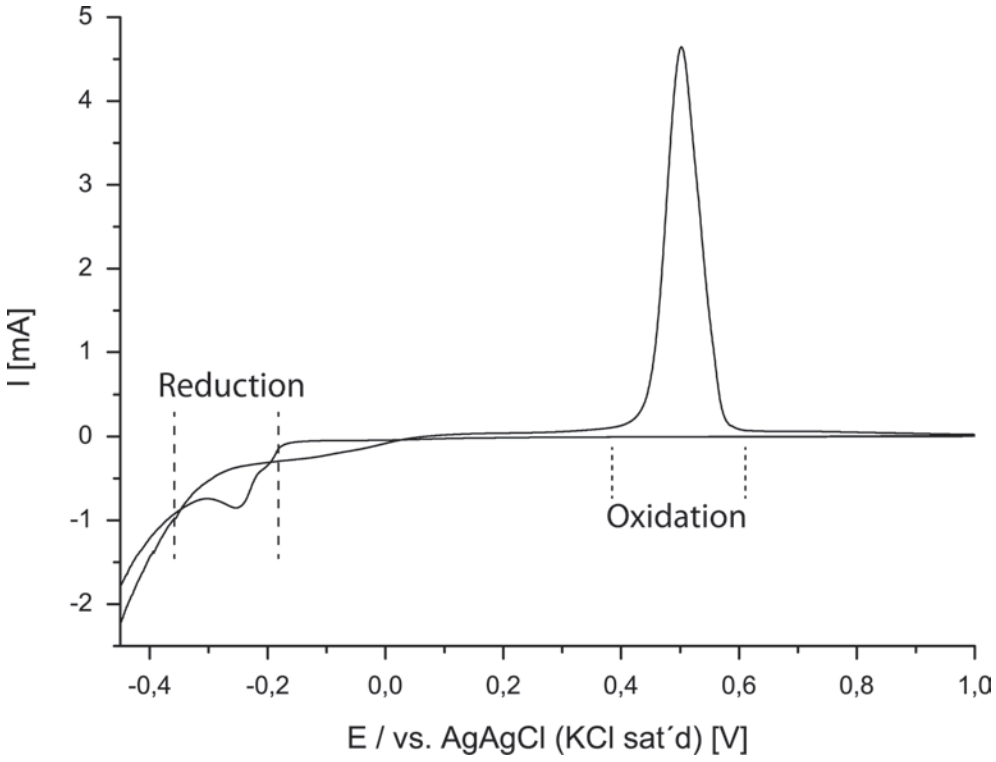

Figure 3.2: Cyclic voltammogram of the Sb_2Te_3 electrolyte containing 0.0056 $\frac{\text{mol}}{\text{L}}$ of SbO_3, 0.01 $\frac{\text{mol}}{\text{L}}$ of TeO_2 and 0.84 $\frac{\text{mol}}{\text{L}}$ of $C_4H_6O_6$ in 1 M nictric acid at a scan speed of 20 $\frac{\text{mV}}{\text{s}}$.

time-consuming. (compare to the results presented in chapt. 6.2)
Analogue to the fabrication procedure of the Sb_2Te_3 solution, the electrolyte for the deposition of $(Bi_xSb_{1-x})_2Te_3$ is prepared from two solutions. One of them contains tellurium-oxide TeO_2 (Sigma Aldrich, 99.995 %) dissolved in 1 M nitric acid and $Bi(NO_3)_3 + 5H_2O$ (Sigma Aldrich, 99.999 %) subsequently dissolved in the solution. The alternative solution contains tartaric acid powder ($C_4H_6O_6$) (VWR, L(+)-tartaric acid for analysis) dissolved in 1 M nitric acid with subsequently dissolving Sb_2O_3 (Sigma Aldrich, 99.999 %). The final electrolyte is fabricated by mixing both solutions.
Figure 3.3 presents the cyclovoltamogramm (CV) of the electrolyte. The deposition process of stoichiometric $(Bi_xSb_{1-x})_2Te_3$ starts at deposition potentials more negative than −280 mV vs. AgAgCl. At deposition potentials between −50 to −280 mV, the deposition of elementary Bi and Sb and mixed phases of them occurs, since they are more likely to be reduced at this potentials. At potentials more negative than −280 mV, the simultaneously deposition of Bi, Sb and Te will occur at the

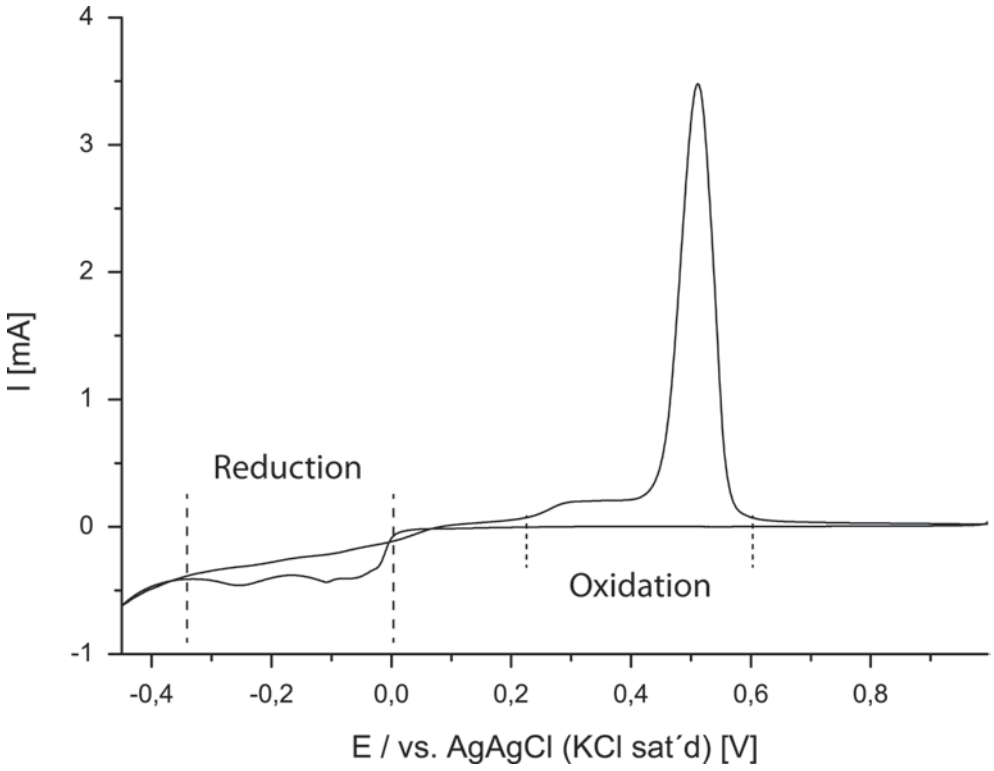

Figure 3.3: Cyclic voltammogram of the $(Bi_xSb_{1-x})_2Te_3$ electrolyte containing 0.002 $\frac{\text{mol}}{\text{L}}$ of $Bi(NO_3)_3 + 5H_2O$, 0.006 $\frac{\text{mol}}{\text{L}}$ of SbO_3, 0.007 $\frac{mol}{L}$ of TeO_2 and 0.9 $\frac{\text{mol}}{\text{L}}$ of $C_4H_6O_6$ in 1 M nictric acid at a scan speed of 20 $\frac{\text{mV}}{\text{s}}$.

electrode surface [BKS10].

3.1.4 $\mathbf{Bi_2(Te_xSe_{1-x})_3}$

This compound is similar to Bi_2Te_3 with Se atoms randomly occupying some Te lattice sites. [Row95] Thus, the fabrication of the electrolyte is prepared by bismuth(III) nitrate pentahydrate $Bi(NO_3)_3 + 5H_2O$ (Sigma Aldrich, 99.999 %) dissolved in 1 M nitric, tellurium-oxide TeO_2 (Sigma Aldrich, 99.995 %) and selenium-oxide (SeO_2) (Strem, 99.95 %) subsequently dissolved in the solution.
The underpotential deposition (UPD) starts at deposition potentials more negative than -50 mV vs. AgAgCl (figure 3.4), while the overpotential deposition (OPD) occurs at reduction potentials more negative than -220 mV. Due to the addition of Se to the electrolyte baths, the deposition potential shifts slightly to more positive potentials, this is consistent

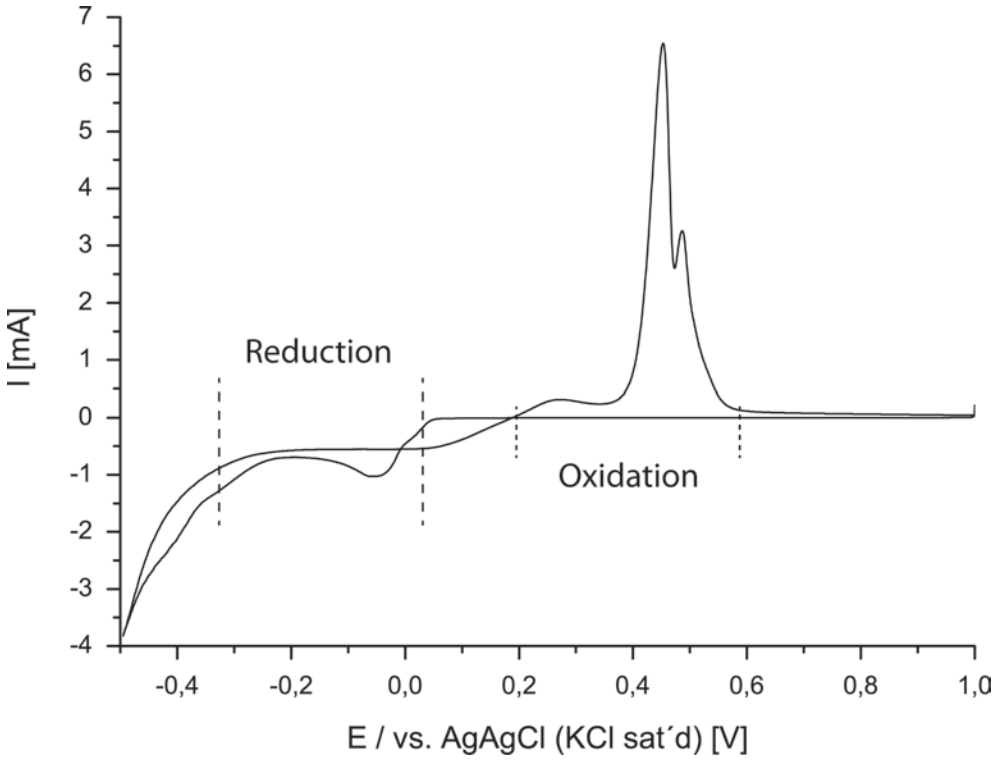

Figure 3.4: Cyclic voltammogram of the $Bi_2(Te_xSe_{1-x})_3$ electrolyte containing 0.01 $\frac{\text{mol}}{\text{L}}$ of $Bi(NO_3)_3 + 5H_2O$ and 0.0011 $\frac{\text{mol}}{\text{L}}$ of SeO_2, 0.01 $\frac{\text{mol}}{\text{L}}$ of TeO_2 in 1 M nictric acid at a scan speed of 20 $\frac{\text{mV}}{\text{s}}$.

to electrolytes previously reported about.[MGSP+03]

3.2 Deposition Parameters

The electrochemical deposition of the thermoelectric films and nanostructures is performed using a Bio-Logic VSP Multichannel Potentiostat System. An illustration of the deposition cell setup used for the electroplating process is presented in figure 3.5.

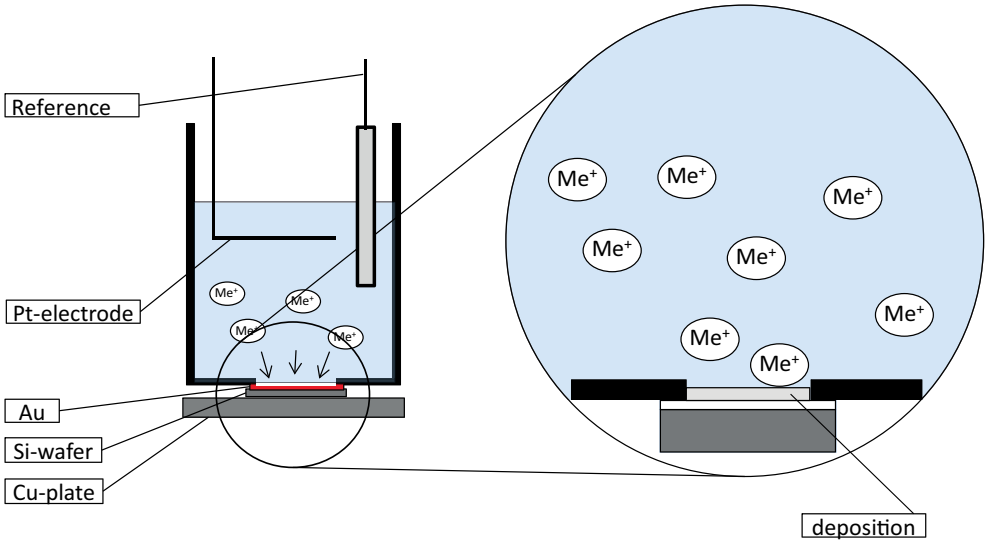

Figure 3.5: Deposition setup used for the electrochemical deposition of films and nanostructures

The deposition process is performed using a three electrode setup corresponding to the conditions presented in fig. 2.3. The deposition potential is applied with respect to a AgAgCl reference electrode (Basi) and a platinum mesh as counter electrode. The samples are mounted between a copper plate and the bottom of the deposition beaker, that has an open gap of circular shape cut out from the bottom. In order to ensure the leak-tightness, an o-ring is mounted between sample and beaker. Then, the copper plate as well as the counter and reference electrode are connected to the potentiostat.

The deposition is performed using the "potentiodynamic millisecond pulsed" method. This method builds up from two different techniques, the potentiostatic and the potentiodynamic deposition methods (figure 3.6 (a) and (b)). The deposition takes place in two steps, periodically repeated as displayed in figure 3.6 (c)). During the on-time, a certain deposition potential is applied for a well defined duration (t_{on} to the system between the working and the reference electrode. The resulting current will be dominated by the electrochemical system. During the off-time (t_{off}), the

deposition potential is fixed to a different value, causing also a change in the resulting current. During the on-time, the deposition of material takes place by the reduction of elemental Bi and Te and co-reaction to Bi_2Te_3 (compare chapt. 3.1.1) at the deposition potential of -120 mV vs. Ref (Ag/AgCl/KCl(sat.)) as determined from fig. 3.1. During the off time, the deposition potential is set to another value. One has to distinguish between three different cases:

(i) The deposition potential is set to a value different from the one applied during the on time, but still able to allow the system to deposit material at the working electrode (but with a different composition due to the changed potential applied). This method may be applicable in order to form multilayered stacks of layers with different compositions.

(ii) The deposition potential is set to much more positive values, where oxidation (compare fig. 3.1) may deplete the material deposited before. This method may be used in order to reach improved morphologies by continuously dissolving and deposition of the material to be deposited.

(iii) The deposition potential is set to the so called "open circuit potential" (OCP), a potential, at which no current flow is observable in the system. Thus, neither reduction nor oxidation occurs. The OCP can be found from the CV displayed in fig. 3.1 at the point, where both lines cross between the reduction and the oxidation and the current is equal to zero.
For the deposition of films and nanostructures presented in this work, the OCP is chosen for the off time. Thus, the current is equal to zero during off time after a certain current peak, which occurs due to capacitive aspects (compare fig. 3.6 (c)).

'Depositions with several different on/off ratios (1/x) are performed and depositions with $x \geq 5$ turned out to work best (compare figs 3.7 and 3.8). Furthermore, it is observed that the absolute value of the on time also has influences the morphology - films deposited with $t_{on}/t_{off} = \frac{1ms}{5ms}$ show less smooth surfaces than the films deposited with $t_{on}/t_{off} = \frac{5ms}{25ms}$ or $t_{on}/t_{off} = \frac{10ms}{50ms}$, which show best results. The advantages of pulsed depositions in the range of milliseconds can be used systematically to improve the quality of deposited thermoelectric films. These improvements result from several different, simultaneous effects during pulsed electrochemical deposition processes, which are not yet fully understood. In principle,

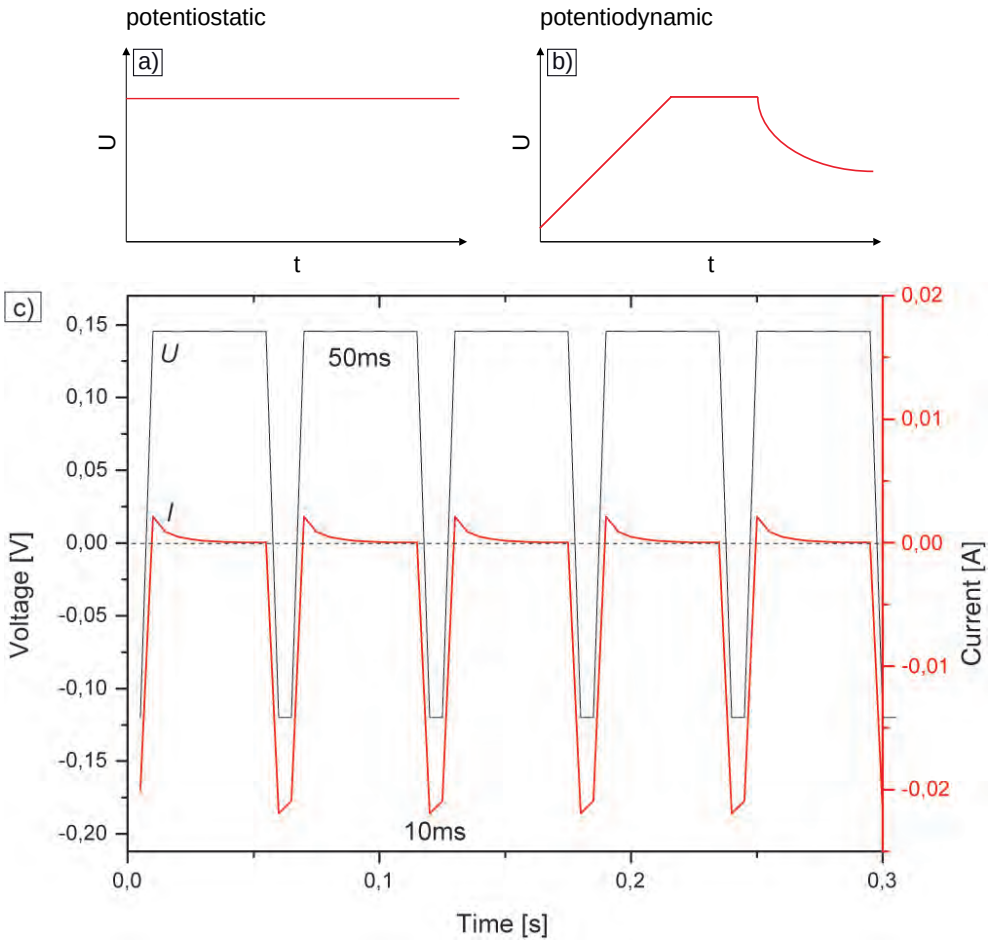

Figure 3.6: Schemes of electrochemical deposition methods (a) potentiostatic, (b) potentiodynamic; (c) deposition potential and -current of a deposition of Bi_2Te_3 with $\frac{t_{on}}{t_{off}} = \frac{10ms}{50ms}$

the advantage of pulsed depositions is to allow the amorphous material deposited during on time to crystallize during the off time [MLP04]. Significant improvements may be due to two different effects of crystal growth: New crystals can grow on the surface in homogeneous distribution or atoms and ions can be added to existing layers [PL90]. A small surface diffusion and a high electrochemical overpotential could possibly abet the growth of new crystals and increase the desorption of defects, while a high surface diffusion and a small electrochemical overpotential could abet the adhesion of deposited atoms to existing layers. During pulsed electrodeposition, a better supply of material within the solution may result in smoother surfaces. As noted above, the absolute time of the deposition cycles is also relevant to the morphology of the deposited

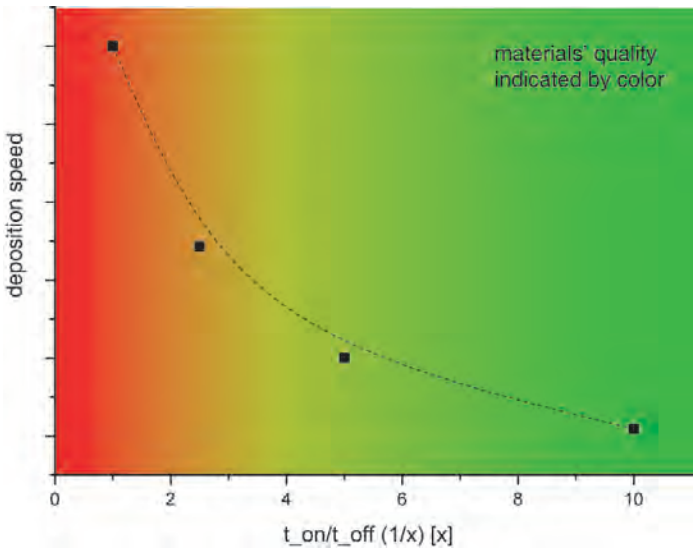

Figure 3.7: Deposition speed, quality and optimum curve in function of the (t_{on}/t_{off})-ratio for t_{on}=10ms

films. Best results are obtained with on times of 10 ms or longer. This is likely due to the timescale of the capacitive currents, which do not contribute to the growth. Based on the currents measured during the "on" time and the concentration of ions in the electrolyte, each pulse must deplete a layer of several micrometers in the solution' [SRA$^+$12]. In figure 3.8, cross section and top views of thermoelectric films deposited with DC potential as well as with different t_{on}/t_{off} ratios are presented.

3.3 Influence of the Substrate

'As a preliminary step for the electrodeposition of thermoelectric films, different substrates were prepared as working electrodes for the deposition. Stainless steel disks as well as Si wafers with layers of gold and platinum using Al, Ni, Co or Cr as an adhesion promoter were used as substrates. Gold with a chromium adhesion layer was found to be most stable during subsequent electrodeposition. These substrates were prepared by using a low-resistance (0.01 $\frac{\Omega}{\text{cm}}$) Si wafer and depositing 20 nm of chromium, followed by 20 nm of gold by magnetron sputtering using a Cressington 308R without exposing the sample to air between both sputter processes. Cr was deposited at I = 20 mA for 1:35 min, Au at I = 40 mA for 4:05 min at pressures of 1 x 10^6 mbar' [SRA$^+$12].

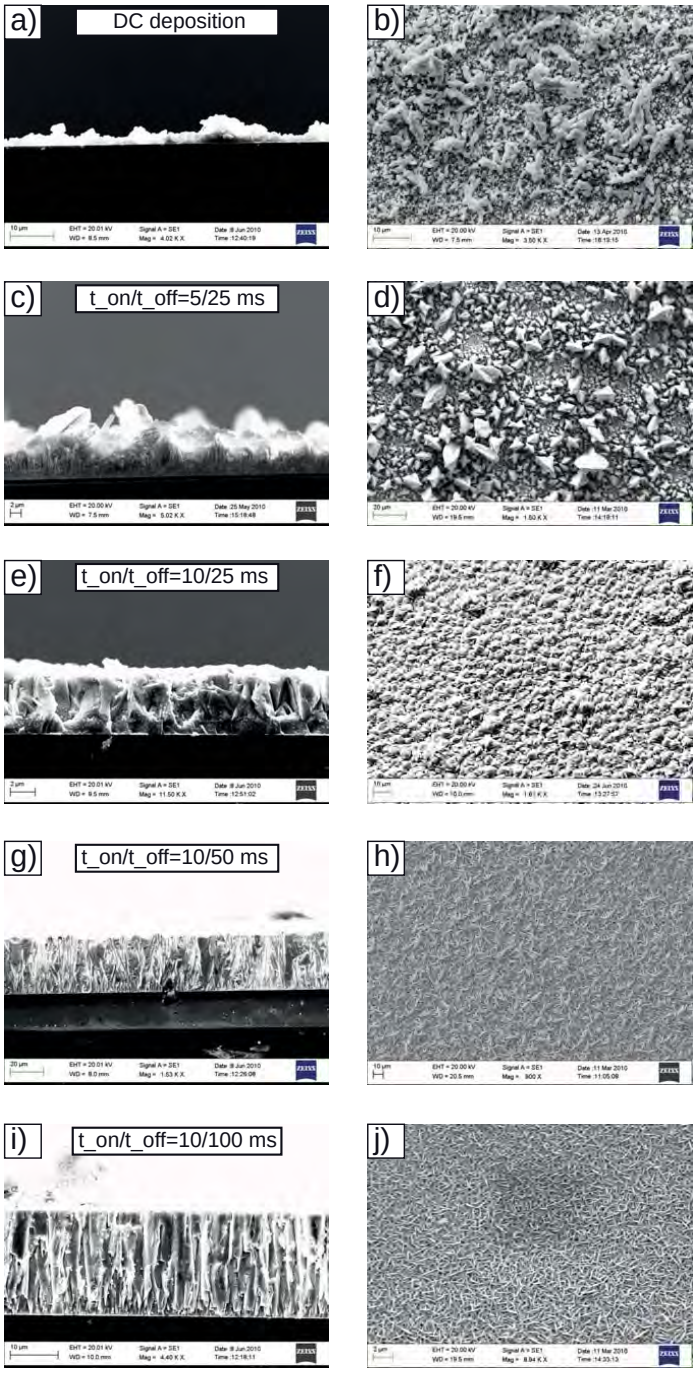

Figure 3.8: Cross section and top views of Bi_2Te_3 films deposited with (a,b) constant (DC) deposition potential of −120 mV vs. Ref (Ag/AgCl/KCl(sat.)); (c,d) a t_{on}/t_{off} ratio of $\frac{5ms}{25ms}$; (e,f) $\frac{10ms}{25ms}$; (g,h) $\frac{10ms}{50ms}$; (i,j) $\frac{10ms}{100ms}$

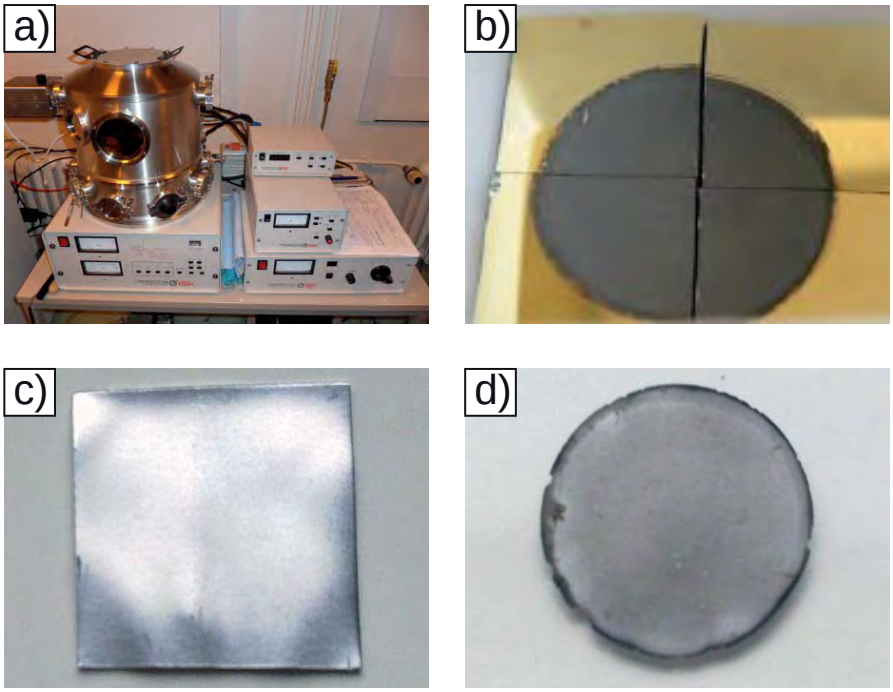

Figure 3.9: (a) magnetron sputter coater Cressington 308R "diver´s bell" for the deposition Cr-(Au/Pt) electrodes; (b) deposited Bi_2Te_3 film on Si-Cr-Au substrate, cleaved and broken sample; (c) stainless steel disc as substrate for the deposition of films; (d) Bi_2Te_3 film after lift-off from the stainless steel substrate

Chapter 4

Characterization

In order to develop and optimize the electrochemical deposition process for thermoelectric materials, an accurately characterization of the materials deposited is highly important. In tab. 4.1, the main methods used for the characterization are listed. The methods are presented in more detail consecutively and exemplary results are presented. The main results for all thermoelectric films are presented subsequently in chapt. 5, 6 and 7. Single nanowire measurements require complex preparation, thus their setups are presented separately in chapt. 8.

	Method	Information	Remarks
chemical& structural	SEM-EDX	composition	accuracy $\approx$ 2-5%
	ICP-OES	composition	accuracy $\approx$ 0.5-1%
	GF-AAS	composition	analysis of nanowires
	XRD	crystal struct.	
	in-situ XRD	crystal struct.	in function of T
	GD-TOF-MS	composition	depth profile (z)
	SIMS	composition	depth profile (z)
Thermo-electric	PSM	Seebeck	cross-plane, in-plane
	LSR/ZEM3	Seebeck & σ	in function of T
	4 point-setup	μ, n & σ	Van der Pauw and Hall
	Laser flash	thermal cond.	at 300 K
	TDTR	thermal cond.	at 300 K - first 300 nm
	4P Single-NW	Seebeck & σ	see chapt. 8
	NW transistor	μ, n & σ,	see chapt. 8

Table 4.1: Survey of methods used for the characterization of the electrodeposited, thermoelectric materials

4.1 Structural Characterization

To achieve information about the structure, not only the composition of the deposited material has to be determined, but also the parameters of the lattice structure, especially for the identification of the materials. The depth profile of the deposits is analyzed in order to prove the homogeneity of the films in z-direction.

4.1.1 Composition

SEM-EDX

The composition of the films and nanowires has been analyzed using an energy dispersive X-Ray spectroscopy (EDX) detector (EDAX) mounted to a scanning electron microscope (SEM - Zeiss Sigma). Figure 4.1 shows the intensities measured for a Sb_2Te_3 films deposited on a Au substrate. The results are presented in tab. 4.2, exhibiting a small amount of tellurium excess (Te [at. %] : 61.87).

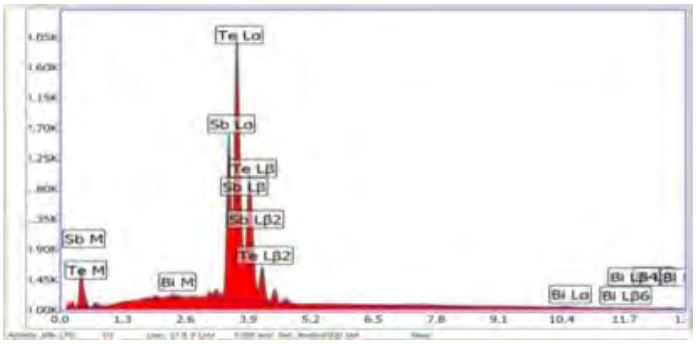

Figure 4.1: EDX graph of intensities of Sb_2Te_3

Element	Line	Weight %	Atomic %	Net. Int.	Net. Int. Error
Bi	M	0,94	0,56	33,68	0,13
Sb	L	37,19	38,43	1015,5	0,01
Te	L	61,87	61,01	1573,55	0,01

Table 4.2: Results of EDX measurement for Sb_2Te_3 (compare fig. 4.1

To prove the composition's homogeneity of the deposited samples, linescans on the surfaces of the thermoelectric films are performed. Exemplarily, the results of a 150-point linescan of Bi_2Te_3 are displayed in fig. 4.2.

At the starting point of the linescan (very right side in fig. 4.2 (a), left side of fig. 4.2 (b)), the substrate without thermoelectric film is scanned. Thus, the counts at this point strongly differ from the rest of the scan. At approximately point #5, the scan of the deposited Bi_2Te_3 film starts. In fig. 4.2 (b), the count intensities presented in (a) are analyzed to inform about the composition. The film exhibits a constant composition of about 57 at. % of Te and 43 at. % of Bi and the homogeneity of the deposition is proved on the surface of the film.

ICP-OES

The analysis using inductively coupled plasma optical emission spectrometry (ICP-OES) has been performed at the department of analytical chemistry (University of Hamburg) and is used for the calibration of the chemical analysis of the films. Dependent to the material reviewed with the EDX method, the specific signals of different materials may overlap, making the interpretation and calculation of the materials composition more difficult or improperly (compare fig.4.1). Therefore, the assistance in determining the compositions by the ICP-OES is used with all samples deposited and reported on in this work. In Fig. 4.3, the functional principle of the ICP-OES is illustrated. In order to achieve the composition of films, a dilution of the thermoelectric materials (films) is nebulized into the inductively coupled plasma. Due to the plasma heater, the digest emitts light with respect to the element-specific wavelength, that is diverted at wavelength-specific angles and detected by multiple CCD detectors, dependent on the angel of refraction.

For this analysis, Bi_2Te_3 films are dissolved in 0.65 mL of 20 % HNO_3 and Sb_2Te_3 films in a mixture of 0.1 mL of 30 % HCl and 0.65 mL of 20 % HNO_3, respectively. After dilution to 10 mL, the analysis was carried out using the Spectro CirosCCD© (Spectro Analytical Instruments, Kleve, Germany). Simultaneous detection of multiple elemental emission lines allowed for the use of a multiline regression procedure, which reduces statistical errors and confidence intervals for the concentrations determined. Further details about the analysis have recently been published in [RSNCB11] and [SRA+12].

GF-AAS

The ICP-OES is not applicable for the analysis of the nanowires' composition, since the concentration of ions for thermoelectric material is insufficiently low in the dilution of nanowires. Therefore, an alternative for the determination of the composition has been used in order to

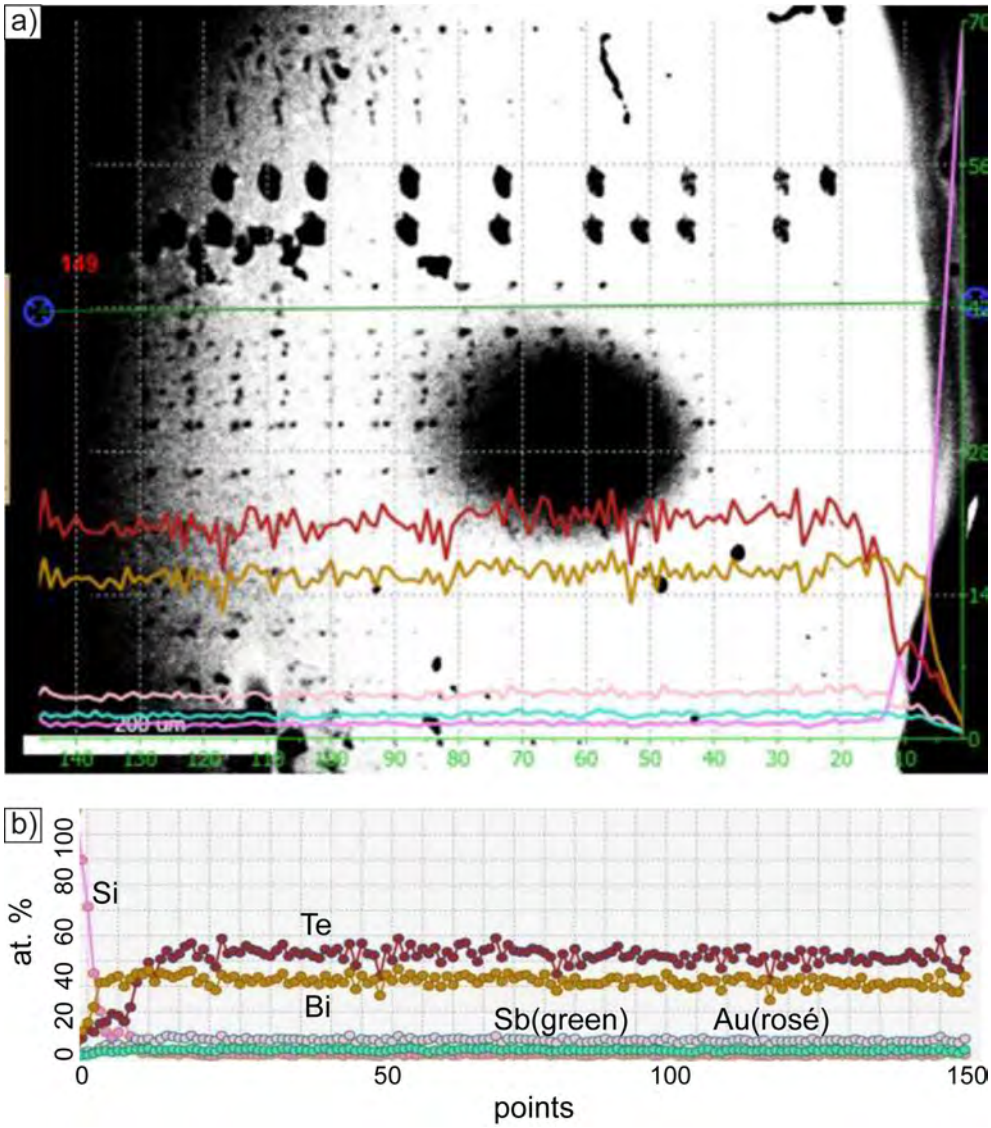

Figure 4.2: Linescan of a Bi_2Te_3 films surface: (a) SEM image of the scanned area (green line) and count-intensities (red,yellow, rose, blue and purple lines) with a total of x=150 points starting with x=0 from the very right side of the drawing; (b) analysis of the linescan , starting with x=0 on the very left side

prove the results achieved with the EDX measurement on nanowire arrays. The graphite furnace atomic absorption spectrometry (GF-AAS) is used, since this method is widely appropriated for high accuracy analysis [BK93]. The principle of this method is illustrated in figure 4.4 (a) - a small amount of sample-dilution is injected into the graphite furnace,

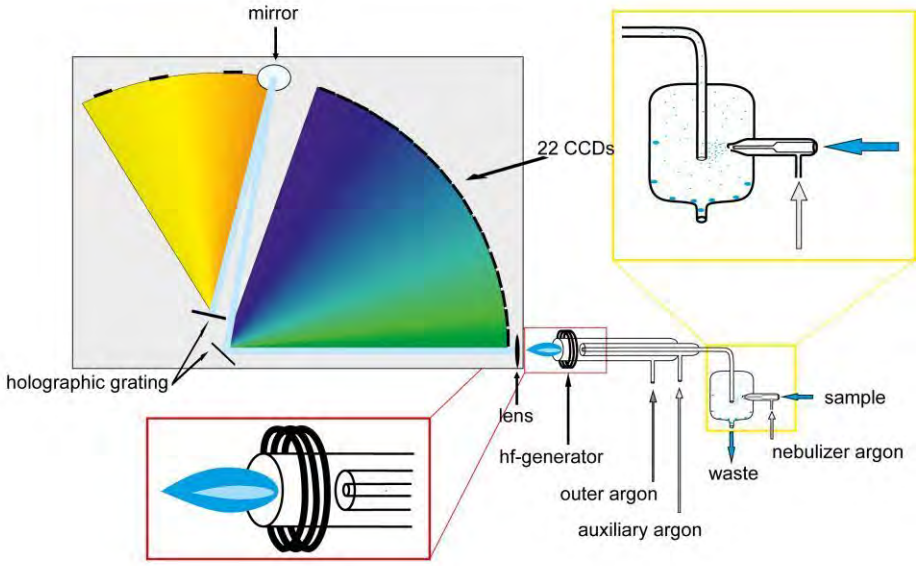

Figure 4.3: Illustration of the ICP-OES [Reinsberg]

where it is vaporized. The exhalation of the sample stays within the furnace, that is located within the course of light with a Xe-specific spectra, created by a Xe arc lamp. The specific wavelengths for the ions located in the sample, are absorbed by the exhalation vapor cloud. The remaining spectrum is dissociated by a prism and an Echelle-grating, focused and headed to a CCD detector. In fig. 4.4 (b), the extinction results for Sb with the analysis of Sb_2Te_3 nanowires are presented. The extinction peak is observable at a wavelength of ≈ 217.59 nm. Therefore it can be determined to be antimony.

Since this method in general is developed for the analysis of solutions with very low concentration, is has to be adapted to the actual requirements. The most difficult part bears on different concentrations of nanowires in the solutions. Since the deposition of nanowires leads to fluctuations of the mass of deposited material (percentage of pores filles during the deposition - compare 8), the amount of nanowires in the solution strongly deviates. The samples were diluted where necessary to 10 $\frac{\mu g}{L}$ to 500 $\frac{\mu g}{L}$ of every main element. In order to ensure the force of expression of the AAS measurement, homogeneous samples are needed to make the injection of the thermoelectric material reproducible, which is necessary, since the elements are not detected simultaneously, but sequentially. However, to ensure the manageability and reproducibility of the dilution and sample introduction into the graphite furnace, samples with concentrations

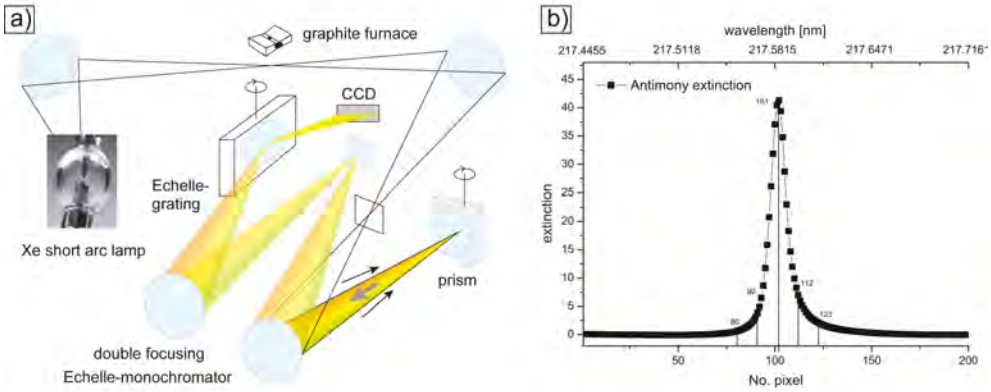

Figure 4.4: Scheme of an GF-AAS detection system used for the characterization of thermoelectric nanowires (a) [RSM+12]; (b) extinction graph of SB, measurement of Sb_2Te_3 nanowire dilution [RSM+12]

higher than 10 $\frac{\text{mg}}{\text{L}}$ and a volume of approximately 1 mL are desirable. General properties of this method for nanowire analysis have recently been reported with [RSM+12].

4.1.2 Lattice Structure

X-Ray Diffraction analysis (XRD)

To date, the X-Ray diffractometry is an often used characterization method to gain information about the crystal structure, e.g. different phases, lattice parameter etc. It is based on the Bragg equation $n\lambda = 2dsin(\theta)$ with the wavelengths of the X-Ray beam λ, the lattice plane distance d, the angle between the lattice plane and the beam θ and the degree of the maximum analysed n. The reflection is illustrated in fig. 4.5, where α is the angle of incidence.

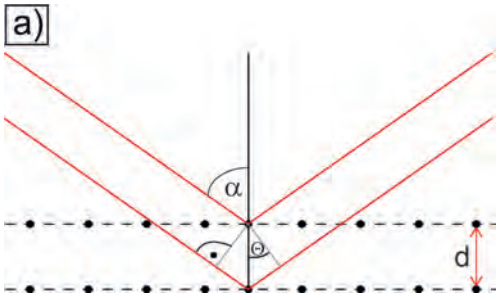

Figure 4.5: Bragg-reflexion

The intensities of the reflected beams are plotted to 2θ by a detector. Since the reflection occurs at multiple lattice layers, the reflected beams exhibit retardations, which show interference in between. Once the reflection takes place at parallel layers, the conditions comply with the Bragg equation causing the interference to be constructive. Thus, the high intensities induce peak maximums indicating the X-Rays to be reflected at the preferred crystal orientations.

In-situ XRD

Since the crystal structure of the thermoelectric materials is supposed to be highly dependent to thermal treatment (compare chapt. 7), the films lattice structure is investigated during annealing in Helium atmosphere, using an experimental heating chamber mounted to a Bruker D8 Discover XRD system. All in-situ XRD measurements are performed at the University of Ghent, Belgium - Department of Solid State Sciences (Christophe Detavernier/Geert Rampelberg). CuKα radiation and a linear Vantec detector is used for characterization, while the sample is heated up from room temperature up to 300 °C at a heating rate of 0.2 $\frac{°C}{s}$. A diffraction pattern is recorded every 5 s in a 2 θ range of 20 ° [RSM+11]. The setup is shown in fig. 4.6. During the in-situ XRD

measurement, the electrical resistivity is measured using a 2 point setup. The results observed during the annealing process exhibit major surveillances, which will be presented and discussed in more detail in chapt. 7.

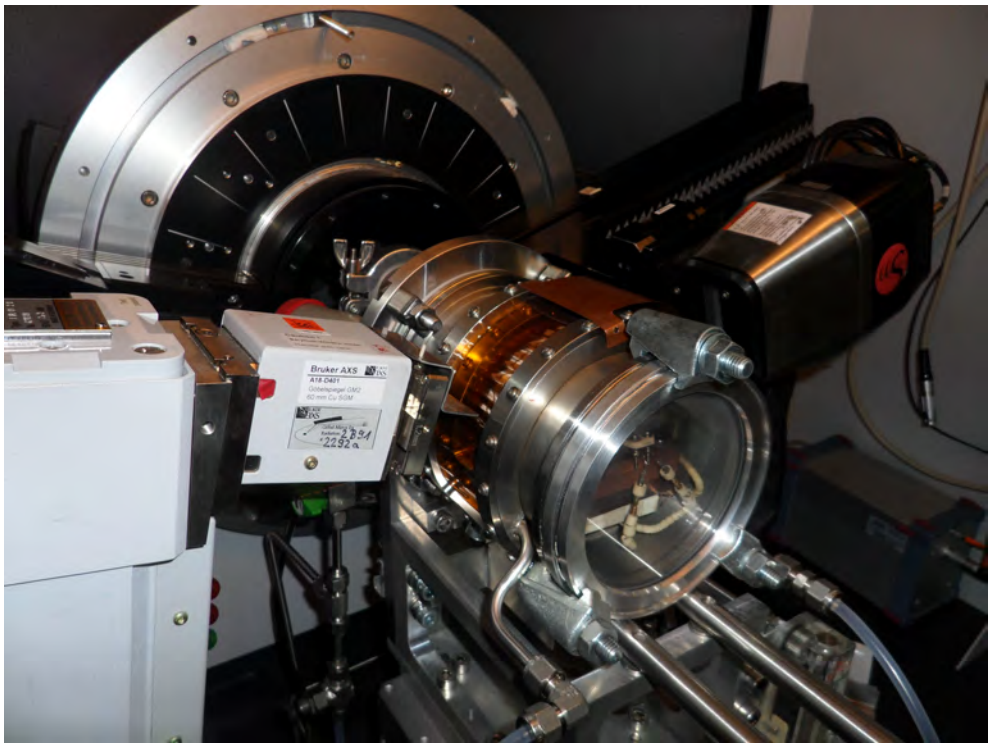

Figure 4.6: Experimental heating chamber mounted to a Bruker D8 Discover System

4.1.3 Depth Profile

In addition to the results presented in chapt. 4.1.1, which prove the homogeneity of the films' composition on the surface (in x- and y-direction) the homogeneity of the deposition in z-direction has to be investigated as well. Since the deposition is accomplished by the control of the reduction potential, the resistance due to the steadily increasing film thickness also may change the effective reduction potential and therefore the films' composition may change as well. The changes may be estimated for instance as:

- resistivity of the deposited material: $\approx 50\ \mu\Omega{\cdot}\mathrm{m}$ [ZSTB07]

- thickness of the deposition: $h = 1 \cdot 10^{-6}$m
- deposition area: $r = 0.8$ cm;$A = \pi r^2 = \pi\ (0.8)^2$ cm^2 $= 2.01 \cdot 10^{-4}$ m^{-4}

$$R = \frac{h}{A} = 0.01 \cdot \frac{100 \cdot 10^{-4}}{2 \cdot 10^{-4}}\ \Omega = 0.5\ \Omega$$

$$\Delta U = R \cdot I = 0.5\ \Omega \cdot 0.01\ \text{A} = 5 \cdot 10^{-3}\ \text{V}$$

$$\Rightarrow \Delta U = -5\ \text{mV}$$

Since the calculation exhibits relatively small amounts of potential changes during the deposition, the chance for significant changes in the films' compositions also is small compared to the uncertainty of the control of the deposition potential. However, in order to prove the film-compositions' changes to be negligible, depth profile measurements in z-direction are carried out using the Glow-Discharge Time of Flight Mass Spectrometry (GD-TOF-MS) and the Secondary Ion Mass Spectrometry (SIMS).

The sample is mounted between an RF-generator and an o-ring in front of a copper anode. The discharge, which is formed as soon as the RF-power is applied abates the samples' surface and the ions from the sample surface are transferred into a time of flight mass spectrometer.

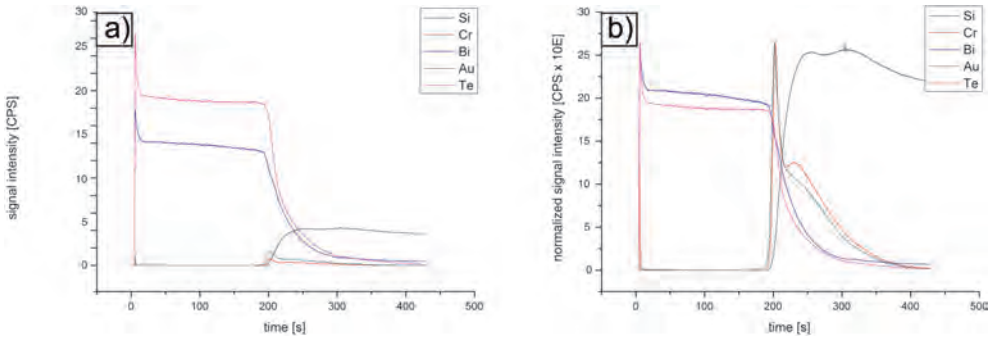

Figure 4.7: Depth profiles of a Bi_2Te_4 film deposited on Si/Cr/Au substrate achieved with GD-TOF-MS, (a) intensities vs. time (depth); (b) normalized intensities vs. time (depth)

In figure 4.7 (a), the depth profile of a Bi_2Te_3 film is shown by the specific element intensities detected over the depth in z-direction. Figure 4.7 (b) presents the data normalized to the maximum. Both graphs exhibit a constant Bi:Te ratio, that indicates a constant composition of Bi_2Te_3 over the whole depth of the electrochemical deposited material. This is constant until the bottom end of the deposition is reached, which is indicated by the increasing intensities of the seed layer materials Au and Cr. Due to their small thickness of 20 nm each, the intensities exhibit sharp peaks. With further increasing depth, the Si intensity becomes dominant due to the Si wafer beyond.
At the very beginning of the measurement, the intensity curves exhibit very high values. This is most likely due to phenomena caused by the starting of the plasma, since the control of the output power is related to the plasma current, which may be higher after engaging. In addition, it also may take time to reach a constant ion concentration in the detection chamber.

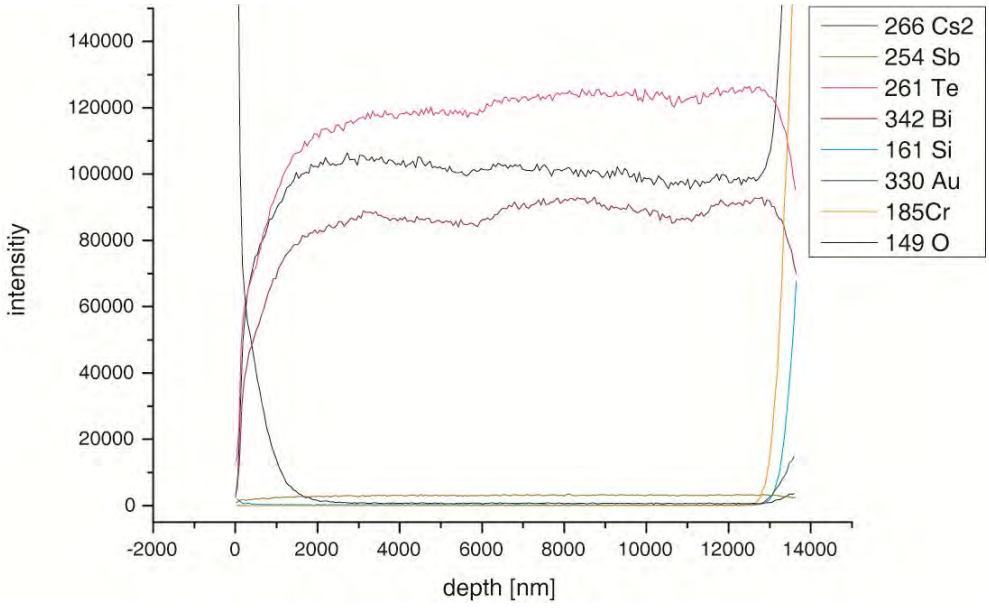

Figure 4.8: Depth profiles of a Bi_2Te_4 film deposited on Si/Cr/Au substrate achieved with SIMS

In addition, measurements by Secondary Ion Mass Spectrometry (SIMS) are performed. In figure 4.8, the depth profile is presented for the same sample as above. In the very beginning of the measurement (surface of the film), the intensities for Bi and Te strongly increase. After reaching the depth, at which the seed layers are detected, both the Au and the

Cr counts strongly increase. For the measurement, Cs ions are used for sputtering the sample, therefore, a significant amount of Cs counts is observable. With this measurement, the existence of an oxide layer can be assumed, since there is is a significant amount of counts for O in the very beginning of the measurement. This may due to the long storage time between both measurements. The SIMS measurement is disrupted after reaching the significant depth, at which the underlying Si wafer becomes observable. However, the results of both the GD-TOF-MS and the SIMS measurements show comparable results, that indicate the good homogeneity of the electrochemically deposited thermoelectric material in z-direction.

4.2 Thermoelectric Characterization

In order to optimize the deposited materials, the Seebeck coefficient S, electrical conductivity σ and the thermal conductivity κ have to be investigated and optimized in order to maximize the figure of merit ZT.

4.2.1 Seebeck Coefficient

Potential Seebeck Microprobe (PSM)

The Seebeck coefficients (compare to eq. 2.1) are analyzed using different setups in order to minimize the standard deviation of the measurement. Standard measurements are performed using a potential Seebeck microprobe PSM (Panco, Germany [Pan07]), which is illustrated in fig. 4.9.

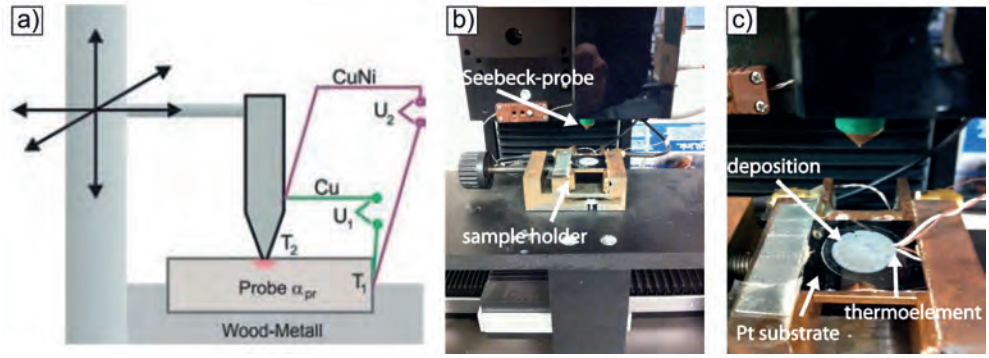

Figure 4.9: (a) Illustration of the Seebeck Microprobe [Panco/DLR]; pictures of the measurement setup with mounted sample deposited on a Si/Cr/Pt substrate: (b) without thermoelement, (c) with thermoelement contacted to the sample

The system originally is designed to measure bulk samples using a low frequent alternating current (AC) by a lock-in amplifier. The sample is contacted by a heated probe tip (fig. 4.9 (b,c)) and the temperature T_2 is determined by a thermocouple. In order to measure the corrected Seebeck coefficient, two measurements are performed with Cu and CuNi thermoelements (compare fig. 4.9 (a)) and the Seebeck coefficient then is calculated by:

$$U_1 = (T_2 - T_1) \cdot (S - S_{\mathrm{Cu}})$$
$$U_2 = (T_2 - T_1) \cdot (S - S_{\mathrm{CuNi}})$$

$$S = \frac{U_1}{U_2 - U_1} \cdot (S_{\mathrm{Cu}} - S_{\mathrm{CuNi}}) + S_{\mathrm{Cu}} \tag{4.1}$$

Since the tip is located on a 3 axis micro positioning stage, scans of the surface of three dimensional samples can be performed. An area of up to 150 mm x 50 mm can be scanned with a max. resolution in the μm range (dependent to the tip used) with samples, that exhibit small thermal conductivity. The films are deposited onto Pt- and Au-substrates with carefully control of height and homogeneity. The films are measured in in-plane and in cross-plane direction. For in-plane measurements, the 'heat sink thermocouple' is connected to the surface of the film with the probe tip scanning the remaining area of the surface (compare fig. 4.9 (c). With this method, free-standing films without substrates can be measured. For cross-plane measurements, the films remains on the conductive substrate used for the electrochemical deposition. The substrate then is connected to the 'heat sink thermocouple' and the probe tip scans the surface of the film (compare fig. 4.9 (b)).

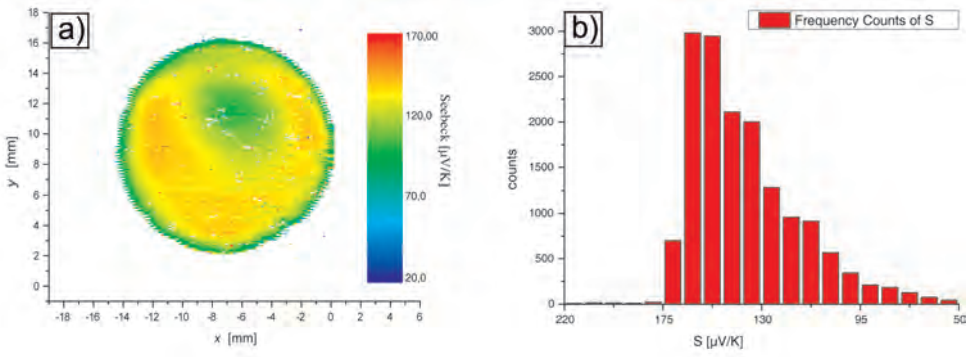

Figure 4.10: (a) 2D distribution of the Seebeck coefficient on the surface of a Sb_2Te_3 film; (b) distribution of counts during the Seebeck measurement

With this method, the homogeneity of the surface with respect to the Seebeck coefficient can be determined. Figure 4.10 (a) presents the distribution of the Seebeck coefficient on the surface of a Sb_2Te_3 films deposited with pulsed deposition ($\frac{T_{on}}{t_{off}} = \frac{10ms}{50ms}$) at a resolution of 100 μm. Although there are slight changes in the Seebeck values observable, the film's composition may assumed to be quite homogeneous due to the good homogeneity of the Seebeck coefficient. In figure 4.10 (b), the count distribution of the measurement is displayed. It exhibits a good allocation of the single-measurements, although there is a slight shift to higher Seebeck coefficients. One may find the reason with the fact, that the highest Seebeck values are observed, the closer the distance to the border of the film becomes. This behaviour is observable until a certain distance $D = D_0$ from the border. At positions $D \leq D_0$, the ion concentration during the

deposition process significantly decreases due to the limited electrolyte diffusion caused by the O-ring (compare fig. 3.5). Thus, the gradient of the diffusion is more negative than towards the middle of the film. The use of a laminar flow of the electrolyte is likely to further improve the homogeneity of the deposition. In order to realize a laminar flow, a complex cell design is required.

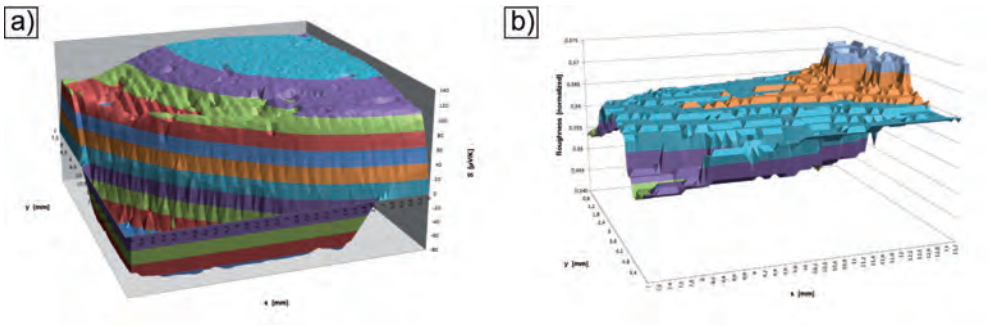

Figure 4.11: 3D plots of a Sb_2Te_3 electrodeposited thermoelectric film (quarter); (a) distribution of the Seebeck coefficient on the surface of the sample; (b) roughness (normalized) of the surface of the deposition.

In figure 4.11, the Seebeck coefficients and the roughness of a quarter of another Sb_2Te_3 sample is presented. As discussed above, the distribution of the Seebeck coefficient is homogeneous, although the fringe and the far right corner of the graph (middle of the sample) exhibit slightly decreasing values due to deviating concentration conditions. This is consistent with the results presented above - due to stirring with a magnetic stirrer, the rotation axis of the stirrer is located above the center of the film. Therefore, the circulation of the electrolyte is limited here. This is also consistent with the roughness of the film presented in fig 4.11 (b). Here, an increased roughness due to limited ion concentrations is observable.

Linseis LSR/Ulvac ZEM-3

For measurements of the films' power factors dependent on the temperature, Linseis LSR and Ulvac ZEM-3 systems are used to perform the measurements of the Seebeck coefficients and the electrical conductivities dependent to the samples' temperature in in-plane direction. Figure 4.12 (a) illustrates the Linseis LSR System and a Seebeck measurement of a free-standing, electrodeposited Bi_2Te_3 film is presented in (b). the measurement is performed mesuring the Seebeck coefficient starting at RT, heating the sample up to about 450 K, annealing of the sample for 50 h and decreasing the temperature back to RT. The measurement

exhibit an increasing Seebeck coefficient with the temperature, a further increase during the long-term annealing process and an improved Seebeck coefficient ($\approx +20$ %) decreasing with decreasing temperature after annealing. Effects observed during annealing lack a discussion in more detail, accomplished thereinafter in chapt. 7.

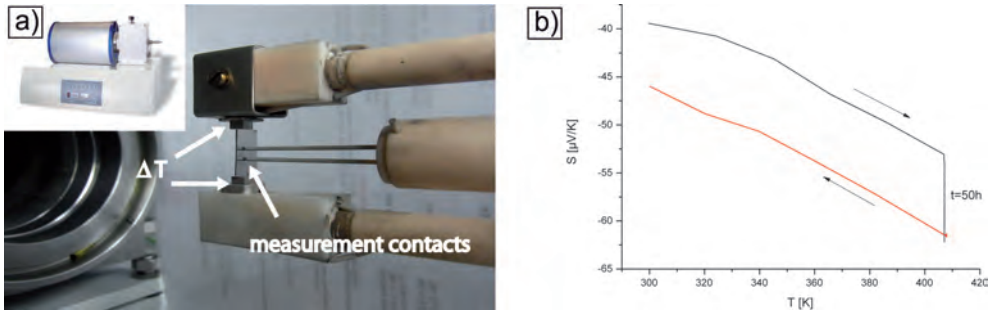

Figure 4.12: (a) Linseis Seebeck measurement setup LSR; (b) Seebeck coefficient vs. sample temperature (measurement with positive/negative temperature gradient) of a free-standing Bi_2Te_3 film

4.2.2 Transport Measurements

Electrical Conductivity & Hall Effect

In order to get a better understanding of the transport processes occurring in the material, it is required to understand the thermoelectric performances' behavior in function of the transport parameter such as charge carrier mobility and density. Thus Hall measurements are performed which allow for the determination of these values. The electrical conductivity is measured using the van der Pauw setup displayed in fig. 4.13. Thereby, a current flows between two directly neighbored contacts (e.g. between 1 and 2 or 4 and 1), while a magnetic field is applied perpendicular to the plane. The Lorentz force then causes a magnetic deflection of the charge carriers, i.e. electrons and holes in the conductor. Therefore, the charge carrier density becomes inhomogeneous and a resulting potential difference can be measured as voltage between the both remaining contacts.
With the following assumptions, the measurement of the electrical resistivity of the sample can be performed:

- The sample must have a flat shape of uniform thickness
- All four contacts must be located at the edges of the sample

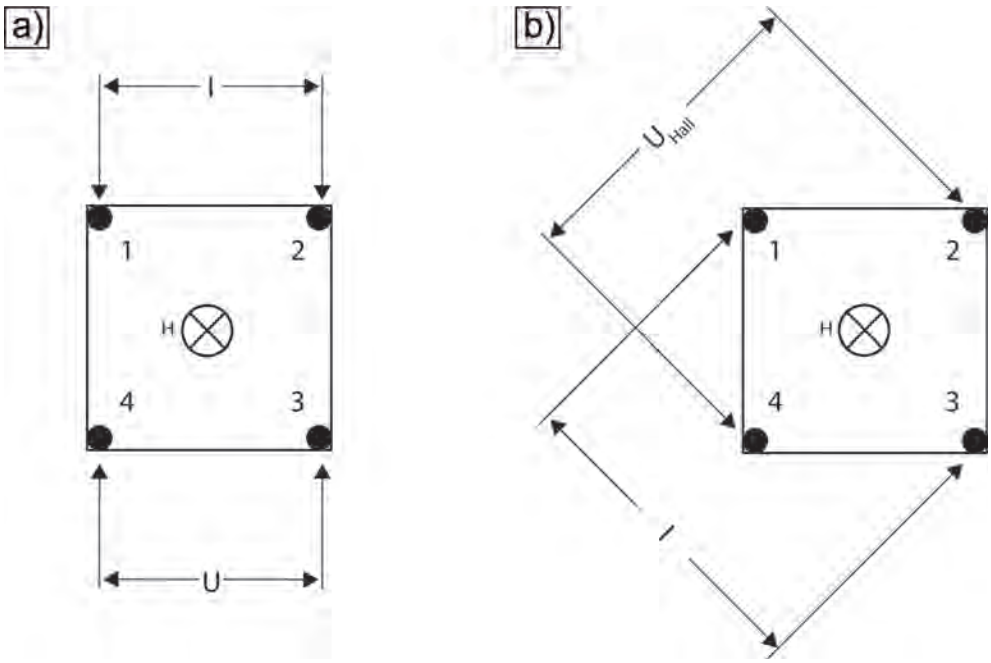

Figure 4.13: Geometry of the van der Pauw method for the characterization of (a) the electrical resistivity, (b) the Hall coefficient

- The sample must not have any isolated holes
- The sample must be homogeneous and isotropic

Then, the resistance

$$R_{12,34} = \frac{U_{34}}{I_{12}}$$

is measured for all pairs of next-neighbor contacts. Van der Pauw [vdP58] found

$$1 = \exp(-\frac{\pi d}{\rho} \cdot R_{12,34}) + \exp(-\frac{\pi}{\rho} \cdot R_{23,41})$$

with the specific resistance ρ, that can be determined by

$$\rho = \frac{\pi d}{\ln 2} \cdot \frac{R_{12,34} + R_{23,41}}{2} \cdot f \tag{4.2}$$

with the correction f, that is given for $\frac{R_{12,34}}{R_{23,41}}$ from [vdP58].
This equation is valid for any type of surface area. Here, the surface area is has two axes of symmetry, since the contacted films exhibit a quadratic shape. Thus, f becomes equal to 1 and 4.2 can be reduced to

$$\rho = \frac{\pi d}{ln2} \cdot R_{12,34}. \tag{4.3}$$

The sheet resistivity then can be determined by

$$\rho_{\text{sheet}} = \frac{\rho}{d} \tag{4.4}$$

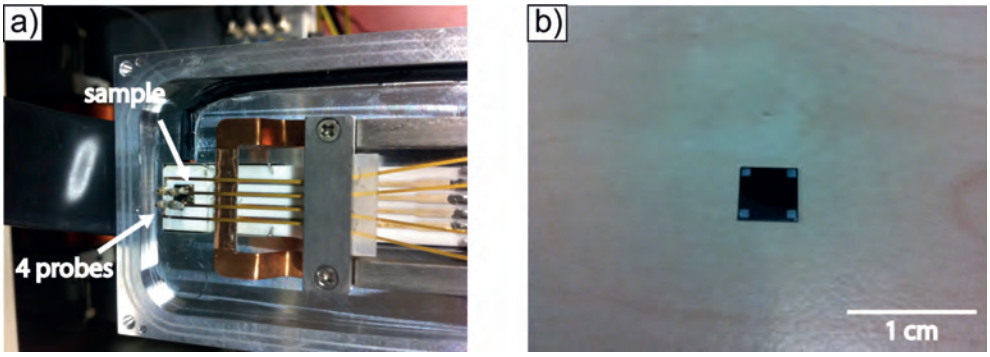

Figure 4.14: (a) geometry of the specimen holder of the H50 System (MMR Technologies); (b) ITO sample with sputtered contacts - length of the edges: 5 mm

Also the Hall coefficient of the sample can be measured using the same geometry, but with a different contacting geometry. The current flow is forced between two contacts in opposite corners of the sample, while the voltage is measured between the remaining contacts. Once the Hall coefficient is determined, one can easily calculate the charge carrier density and the charge carrier mobility.
A more detailed discussion of the correlation between these variables is given in chapt. 7. Since this method is widely used as a standard characterization, more information can be found in the literature, e.g. [vdP58].

The films are measured using the Hall H50 System (MMR Technologies, CA, USA) and a self assembled 4 point setup. The geometry used is displayed in fig. 4.14. Therefore, the samples are prepared in a quadratical shape with a length of the edges of 0.5 cm (compare fig. 4.14 (b). First samples are measured with and without sputtered Au contacts, finding the results to be identically. The samples are mounted into the chamber using the 4 probes to fix the sample (Figure 4.14 (b)) before mounting the whole chamber to the external magnet in order to apply the magnetic field required for the measurements at 300 K. The magnetic field was applied with ±1 Tesla (T) perpendicular to the film's surface in both directions.

4.2.3 Thermal Conductivity

The thermal conductivity of the electrochemically deposited thermoelectric films perpendicular to the films' surface is analyzed with the Xenon Flash method system XFA 500 (Linseis, Germany). Therefore, free-standing samples are prepared by electrochemical deposition of thermoelectric material on stainless steel substrates. After the lift off process (compare 3.3), the samples are coated with graphite spray on both sides. Thus, the samples no longer exhibit significant reflectivity. The samples are mounted to the sample cylinder (fig. 4.15) and a xenon flash shot is sent to the bottom of the sample. Thus, the sample's temperature increases and an infrared (IR) detector is measuring the characteristic temperature gradient on the top surface of the film. Then, the thermal diffusivity $a(T)$ can be calculated. Since this method is widely used for thermal analysis, one may compare to [Lin]. Once the specific heat C_p and the density ρ is known, the thermal conductivity κ may be calculated by:

$$\kappa(T) = a(T) \cdot \rho(T) \cdot C_p(T) \tag{4.5}$$

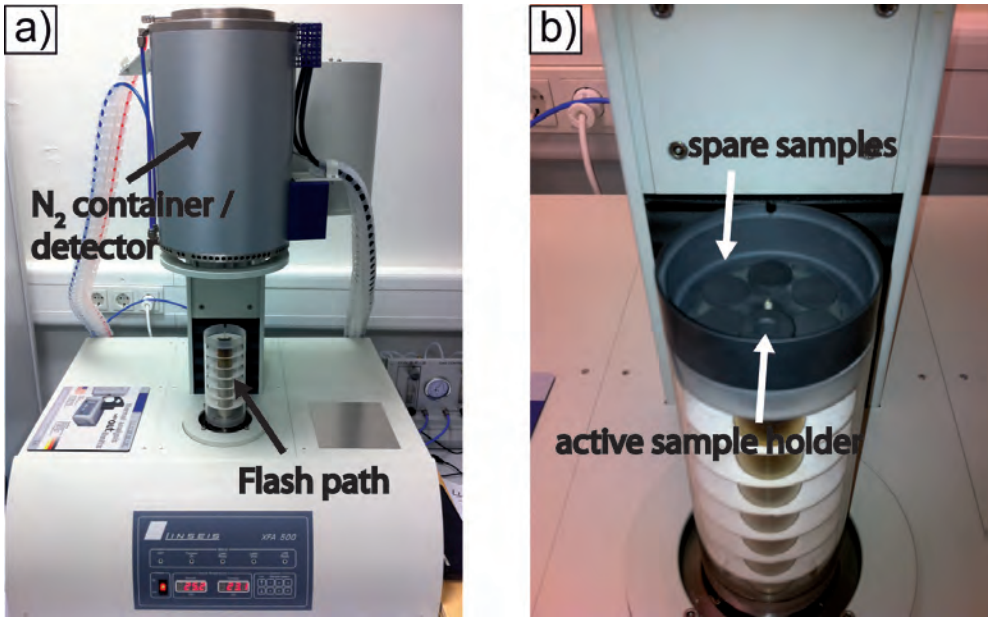

Figure 4.15: (a) Linseis Xenon Flash measurement setup XFA 500; (b) tube for the optical path of the xenon flash with mounted sample cylinder of XFA 500

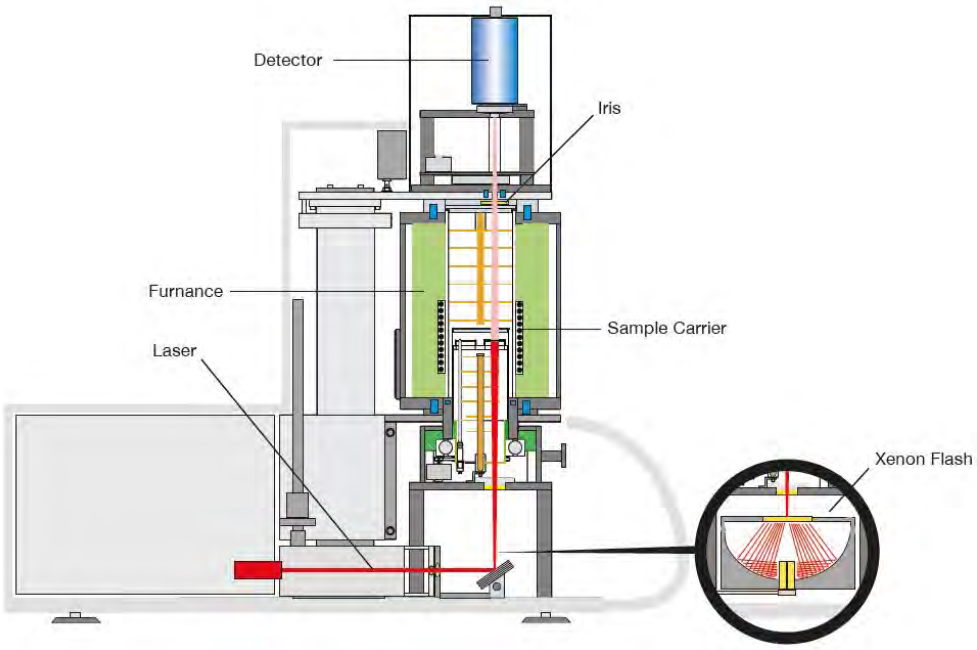

Figure 4.16: Illustration of the Linseis Xenon Flash System XFA 500 [Linseis]

Time Domain Thermoreflectance measurement (TDTR) Using the time domain thermoreflectance measurement (TDTR) first developed by David Cahill, the electrodeposited films are characterized in terms of thermal conductivity as well. This method is applicable especially for thin films, since the thermal conductivity up to thicknesses around a few hundred nanometers can be determined. All measurements presented in this work are performed by D. Cahill.
A pulsed laser heats up the sample localized to a defined surface area. This localized change in T will cause local thermal stresses, which cause a change in reflectance R_F of the surface. This change is measured by a secondary laser. The change in R_F can be expressed by [Cahill et al., 2003]

$$\Delta T = (1 - R_F)\frac{Q}{C_p(go)}\exp(-b/g)$$

with the optical pulse energy Q, the specific heat C_p, optical absorption length g, the spot size o and the in-sample distance b. By applying a model, these values can be expressed in terms of the thermal conductivity.

4.2.4 Discussion of the Thermoelectric Analysis

'The measurement of the thermoelectric performance always requires several measurements, each of them exhibiting uncertainties of around 5 - 10 %, which cannot be neglected. The composed uncertainty for the whole thermoelectrical characterization can be estimated [ST08] by:

$$\frac{\Delta Z}{Z} = 2\frac{\Delta S}{S} + \frac{\Delta \sigma}{\sigma} + \frac{\Delta \kappa}{\kappa} \tag{4.6}$$

with the thermoelectric figure of merit ZT, the Seebeck coefficient S, the electrical conductivity σ, and the thermal conductivity κ. Since the samples were prepared on Au/Pt-substrates as well as on stainless steel substrates, which allow for the lift-off of the films after the deposition, the influence of the conductive substrate to the Seebeck coefficients could be determined, finding it to be negligible for our system, due to the small thickness of the substrate compared to the films' thicknesses. Although this is consistent to the theoretical calculations presented in [NSW+11], the error due to the measurement itself is somewhat higher at around 6 %. Since the measurement of the Seebeck coefficients was performed in in-plane direction as well as in cross-plane direction, finding the differences to be negligible ($\Delta S \leq 3\%$) with respect to the accuracy of the measurement itself, here $S_{=} = S_{\perp}$ can be assumed leading to

$$(ZT)^{*} = \frac{S_{=}^{2} \cdot \sigma_{=}}{\kappa_{\perp}} T = \frac{S_{\perp}^{2} \cdot \sigma_{=}}{\kappa_{\perp}} T \tag{4.7}$$

with the thermoelectric figure of merit $(ZT)^{*}$, which is actually identical to to ZT, but with some contributing parameters measured in different directions. The thermal conductivities in this work are measured with the xenon flash method on free-standing films. The need for the knowledge of density, heat capacity C_p and thermal diffusivity a in order to determine the thermal conductivity again decreases the accuracy of the determination of ZT. The uncertainties of a and C_p are in the order of $\pm$ 10 % each and the density's accuracy is assumed to be $\pm$ 15 % due to the possibility of significant porosity of the deposited films [SOV+10]. Thus, the accuracy of ZT can easily reach $\pm$ 40 % [SRA+12]'.

Now, that the main characterization methods are known, subsequently they are used in order to analyze both the n-doped and the p-doped thermoelectric films and nanowires in chapt. 6, 5, 7 and 8.

Chapter 5

N-doped Materials

The successful integration of thermoelectric materials requires the development of n- and p-doped materials (compare chapt. 1), which exhibit both majority charge carriers. Materials with electrons as charge carriers are well reported in the literature. One of the major characteristics of intrinsic semiconductor material is the Fermi-level to be located in the middle on the gap between the energy bands. Since the wave vectors of the charge carrier states has to be fair enough at the band edges, the band gap has to be relatively small. Although the Fermi-level still lies within the band gap at n-dopes extrinsic materials, it is located near to the edge of the conductance band (compare chapt. 1) as it is illustrated in fig. 5.1. Thus, the wave functions of the electron states remain at significantly high values, causing free electrons located at the lower edge of the conduction band, which are contributing to the electrical conduction.

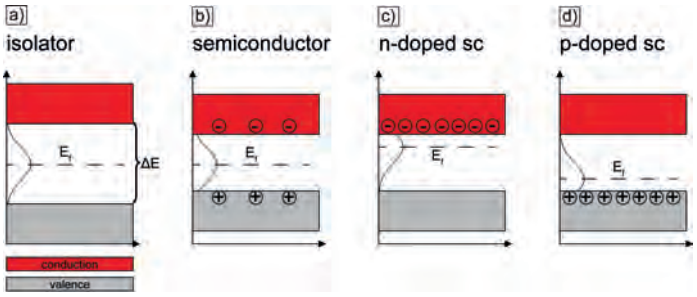

Figure 5.1: Energy bands of (a) an isolator, (b) an intrinsic semiconductor, (c) an extrinsic n-doped semiconductor, (d) an extrinsic p-doped semiconductor

The quantity of charge carriers (electrons for n-doped semiconductors) can be specified using the density of states (DOS) near the band gap

$$G(E)dE = \frac{4\pi(2m^*)^{\frac{3}{2}}dE}{h^3}, \tag{5.1}$$

with the effective mass m^*. Together with equation 2.6, the total number is calculated as

$$n = \int_0^\infty \frac{4\pi(2m^*)^{\frac{3}{2}}}{h^3(1+e^{\frac{E-E_f}{k_BT}})}dE \tag{5.2}$$

Although here the number of electrons near the conduction band is calculated, this can be done in parallel, if the Fermi-level is located near the valence band. Thus, the calculation then is performed for p-doped semiconductors (compare chapt. 6).

5.1 Binary Bi_2Te_3

Bismuth telluride has a rhombohedral unit cell consisting of five atoms per unit cell. It crystallizes in the R$\bar{3}$m point group and the crystallographic structure is observed to be a hexagonal primitive cell. This cell contains multiple layers perpendicular to the c-axis (symmetry axis). These identical layers are to form the hexagonal lattice exhibiting the sequence

$$-Te^1 - Bi - Te^2 - Bi - Te^1- \tag{5.3}$$

presented in fig. 5.2 (a). In (b), the Brillouin zone is illustrated. [Row06].

Symbol	Value	Dim.	Description
a_0	10.418	$\mathring{A}$	Rhombohedral vector at 0 K
α	24° 12' 40"		Rhombohedral angle at 0k
b_0	1.6731	$\mathring{A}^{-1}$	Reciprocal lattice vector
β	61° 30' 37"		Rhombohedral angle for reciprocal lattice
V	169.11	$\mathring{A}^3$	Unit Cell Volume
Γ_A	0.8366	$\mathring{A}^{-1}$	1/2 (100)
Γ_D	0.8556	$\mathring{A}^{-1}$	1/2 (100)
Γ_Z	0.3108	$\mathring{A}^{-1}$	1/2 (111)
Θ_1	7° 6' 50"		Angle between Γ_A and Γ_Y
Θ_2	14° 0' 50"		Angle Y between Γ_D and Γ

Table 5.1: Lattice parameter of the Brillouin zone for Bi_2Te_3 (compare fig. 5.2 (b) [Lov77][Row06]

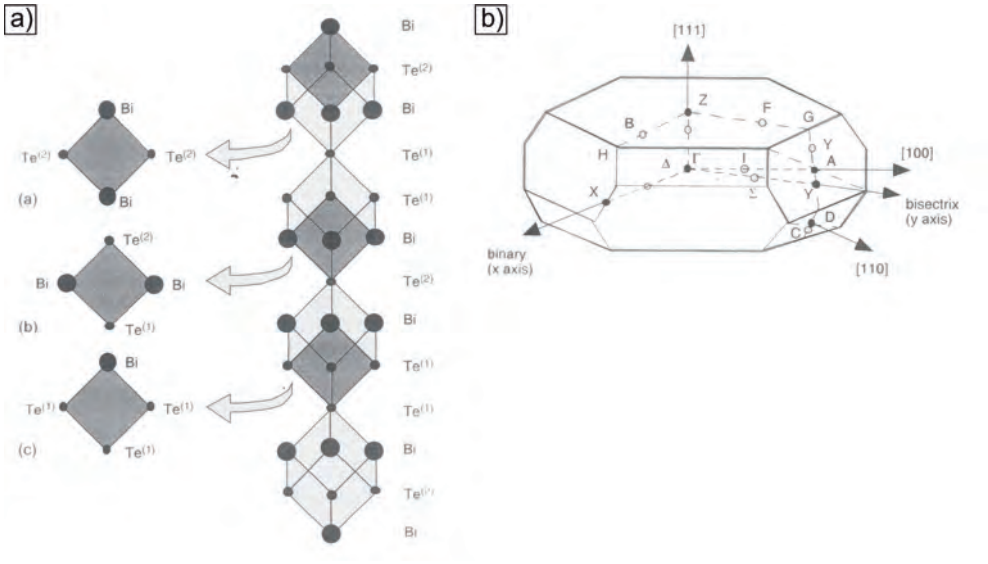

Figure 5.2: (a) crystallographic structure of Bi_2Te_3; (b) Brillouin zone for Bi_2Te_3 [Row06]

The hexagonal cell of Bi_2Te_3 is composed from three sequences that are connected with $Te^1 - Te^1$ bonds in between. Since these bonds are of Van der Waals type [DG58], Bi_2Te_3 is likely to cleave along the planes perpendicular to the c-axis. In contrast, the $Te^1 - Bi$ and $Bi - Te^2$ bonds are based on ionic covalence [BPN71] and therefore they exhibit stronger bindings. Since the crystallographic structure exhibits multiple layers to form the lattice, in principle, the properties of Bi_2Te_3 show anisotropic behavior.

Electrochemically deposited bismuth telluride is very well reported in the literature (compare chapt. 2), since the deposition of the material is comparatively easy. Many reported materials exhibit large excesses of either bismuth or antimony. Also, the thermoelectric performance of such materials often is not satisfactory. Small changes in the materials' composition may result in significant decreases of the thermoelectric parameters, in particularly the Seebeck coefficient [SS59]. However, many works lack the careful control of the composition or/and the thermoelectric characterization. Thus, the optimization process of Bi_2Te_3 presented in this work starts with the investigation on the morphology and composition.

5.1.1 Structural Properties

Bi_2Te_3 films are deposited using the potentiostatic millisecond pulse method with $\frac{t_{on}}{t_{off}} = \frac{10ms}{50ms}$. SEM images are presented in fig. 5.3. In (a), the cross section of a films with the thickness $d = 13\ \mu m$ is shown, with a homogeneous growth and thickness in z-direction and a crystalline structure of high compactness observable. In 5.3 (b), the top view is presented. It exhibits the characteristic structure with needlelike crystals.

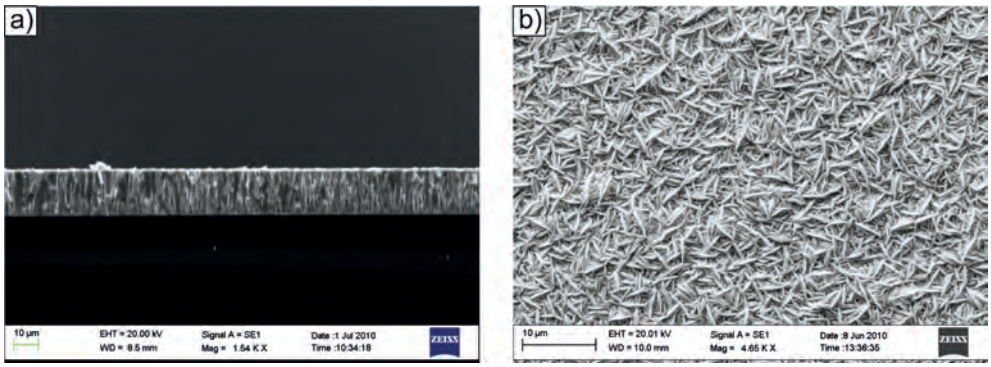

Figure 5.3: SEM-pictures of Bi_2Te_3 films electrodeposited with pulsed deposition technique (10/50 ms), (a) cross-section, (b) surface

The SEM picture presented in fig. 3.8 in chapt. 3.2 also show Bi_2Te_3 films deposited with different pulse parameters. X-Ray diffraction pattern of the Bi_2Te_3 films are presented in fig. 5.4 deposited with DC and pulsed deposition (10/50ms).
The material's characteristic peaks are observed at 28° and 42° indicating the preferred orientation in (015) and (110) direction, respectively. DC deposited material exhibits a more pronounced orientation in (110) direction, indicated by the reflection intensities I_R with $\frac{I_{(015)}}{I_{(110)}} \approx 0.7$ (DC) and ≈ 1.2 for pulsed deposited films.

	DC	pulsed deposited (10/50 ms)	Bi_2Te_3 bulk [Row95]
a $\left[\mathring{A}\right]$	4.363	4.392	4.3835
c $\left[\mathring{A}\right]$	30.130	30.213	30.360
crystal size $[nm]$	437	523	

Table 5.2: Lattice parameter of Bi_2Te_3 films - calculated from XRD pattern

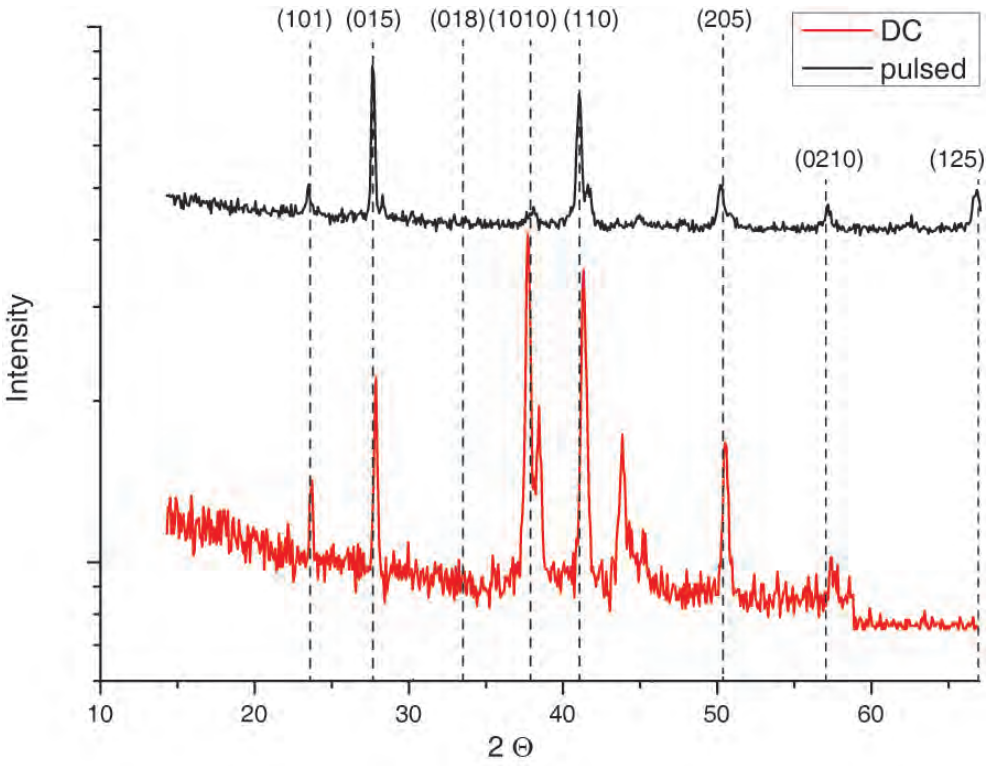

Figure 5.4: Comparison of both DC and pulsed deposited films' XRD pattern

The lattice parameters presented in table 5.2 are calculated using the Bragg equation $n\lambda = 2dsin(\theta)$ and the lattice plane spacing

$$\frac{1}{d^2} = \frac{4}{3}(\frac{h^2 + hk + k^2}{a^2}) + \frac{l^2}{c^2} \tag{5.4}$$

The crystal size is achieved from:

$$D = \frac{FWHM \cdot cos\Theta}{0.9\lambda} \tag{5.5}$$

with the Miller indices h,k,l, the lattice parameter a,c, and the half-maximum (FWHM) of the reflectance peaks. They exhibit only slight differences - this may be due to crystal imperfection or instrumental errors - to the standard of reference [JCP] ($a = 4.381\mathring{A}$ and $c = 30.483\mathring{A}$) and are also comparable to the ones reported in other works on the electrochemical deposition of Bi_2Te_3, e.g. in ref. [FYX+07]. Pulsed deposited films show a smaller deviation from standard lattice parameters

than DC deposited films. This is another indicator for higher crystallinity and consistent to the observations in terms of morphology from the SEM pictures above. Thus, consecutively, pulsed deposited films are discussed in more detail.

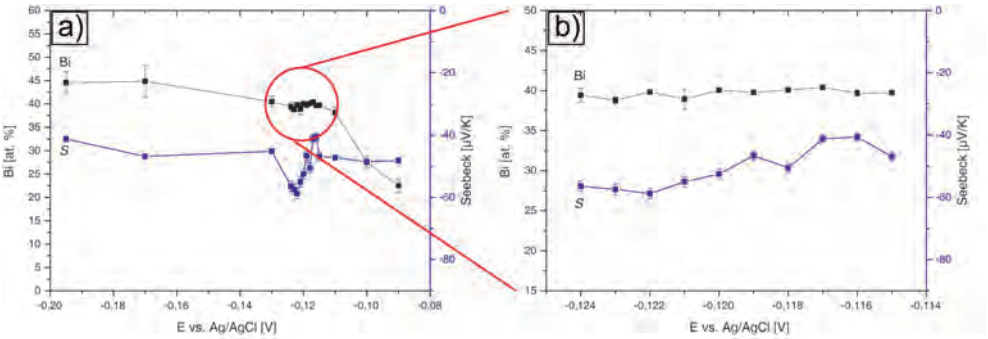

Figure 5.5: Composition of Bi_2Te_3 films pulsed deposited (10/50 ms) at multiple deposition potentials

In fig. 5.5, the composition and Seebeck coefficient of pulsed deposited Bi_2Te_3 films is presented. In fig. 5.5 (a), the composition is presented for a wide range of deposition potentials appropriate for the potentiostatical deposition of Bi_2Te_3 materials (compare fig. 3.1). Since the best results are observed around -0.120 V vs. Ag/AgCl reference, several samples are prepared with deposition potentials ranging from -0.125 V to -0.115 V with an increment of -0.001 V as presented in fig. 5.5 (b). The films exhibit almost ideal stoichiometry at 40 at. % of Bi and 60 at. % of Te over a wide range. The Seebeck values show moderate changes within -40 to -55 $\frac{\mu V}{K}$. The measurement of the Seebeck coefficient is performed as described above (compare chapt. 4.2).
Films, deposited with the millisecond pulse technique exhibit huge deviations in film thickness, although the deposition parameters, e.g. the deposition remains constant for multiple samples. Since no constant deposition rate is observed, the control of the film thickness is difficult. This may be due to the very plain electrode surface used with sputtered Au/Pt seed layers (compare chapt 3.3). Thus, the starting of the initial nucleation process may be randomly deferred.
In order to realize predictable deposition rates, the start of the growth process is forced by an initial "nucleation pulse" at a very high overpotential more negative than -0.3 V vs. Ag/AgCl. Since the current density achieves very high values, the nucleation even on the plain surface is forced and a "starting layer" of deposited material is produced.

After the nucleation pulse, the deposition process is performed normally. In fig. 5.6 (a), the length of the nucleation pulse is set to 3 s. Thus, the pulsed deposition of Bi_2Te_3 films at a (on-time) deposition potential of -0.15 V vs. Ag/AgCl scales linearly with the deposition time, while the deposition Bi_2Te_3 films at a potential of -0.12 V do not. In fig. 5.6 (b), the length of the initial nucleation pulse is set to 5 s - here, both samples exhibit constant growth rates. Thus, the length of 3 s of the nucleation pulse is likely to force an insufficient amount of deposited material. Thus, the starting layer may be fragmented or imperfect in some cases. On the other hand, a nucleation pulse of 5 s in length is adequate in order to ensure a satisfactory control over the depositions' thickness.

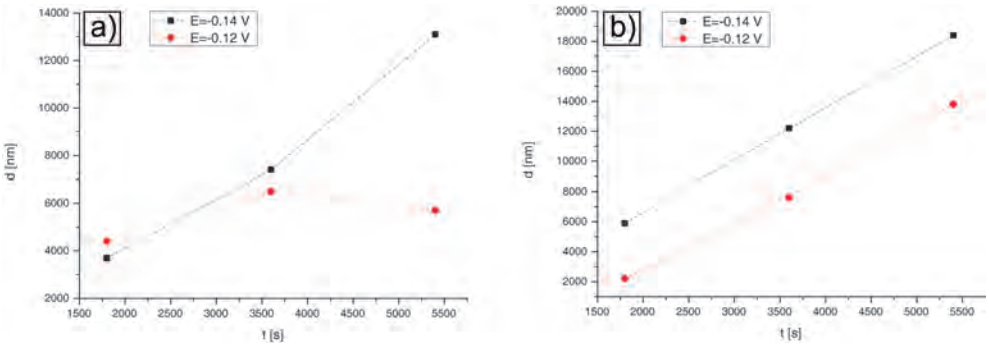

Figure 5.6: Thickness dependent on the deposition duration - Bi_2Te_3 films pulsed deposited (10/50 ms) at -0.14 V (black line) and -0.12 V vs. Ag/AgCl (red line) reference, (a) deposited with a nucleation pulse of 3 s, (b) deposited with a nucleation pulse of 5 s

5.1.2 Transport Properties

In fig. 5.7, the charge carrier density (a) and the charge carrier mobility (b) of pulsed deposited Bi_2Te_3 films are presented. As observed above, the electrochemical deposition within the range of -0.125 to -0.115 V causes very homogeneous films with almost identical materials' quality. The carrier densities diversify within a range of $0.1 \cdot 10^{20} \frac{1}{\mathrm{cm}^3}$, comparable to Bulk values reported $(9.5 \cdot 10^{19} - 2 \cdot 10^{20} \frac{1}{\mathrm{cm}^3})$[FYX+07].
The carrier mobility shows slightly higher values compared to the literature (7-9 $\frac{\mathrm{cm}^2}{\mathrm{V \cdot s}}$), indicating a good crystal quality by comparable large crystals/grains (compare tab. 5.2). Thus, the movement of charge carriers (electrons) is inhibited by grain boundaries, causing a high mobility and high crystallinity. Both the carrier density n and mobility μ indicate a homogeneous distribution of Seebeck coefficients, although the depen-

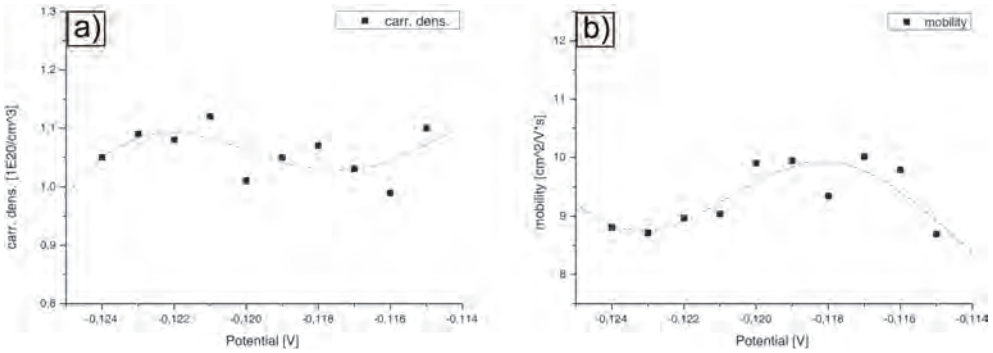

Figure 5.7: Electrical properties of Bi_2Te_3 films pulsed deposited (10/50 ms) vs. deposition potential, (a) charge carrier density (electrons), (b) charge carrier mobility; lines are guides to the eye

dence of between S, n and μ is more complicated and will be discussed in chapt. 7. [Gol09]

5.1.3 Thermoelectric Performance

The electrical conductivity show moderate variations at deposition potentials around -0.12 V vs. Ag/AgCl, consistent to the homogeneous distribution of charge carrier density and mobility, since it can expressed as $\sigma = ne\mu$ as discussed above. Based on the Seebeck coefficient S and the electrical conductivity σ, the power factor

$$pf = S^2 \cdot \sigma \tag{5.6}$$

can be calculated (fig. 5.8 (b)). The thermal conductivity is determined by laser flash/TDTR method (compare chapt. 4).

		Bi_2Te_3 pulsed dep. (10/50 ms)
σ	[Scm^{-1}]	158
S	[μVK^{-1}]	-60
pf	[$\mu WK^{-2}m^{-1}$]	57
κ (RT)	[$WK^{-1}m^{-1}$]	0.9
ZT(RT)		0.02

Table 5.3: Thermoelectric performance of Bi_2Te_3

The thermoelectric performance of the Bi_2Te_3 films exhibits relatively poor Seebeck values in the range of 25 - 60 $\frac{\mu V}{K}$. Since the power factor

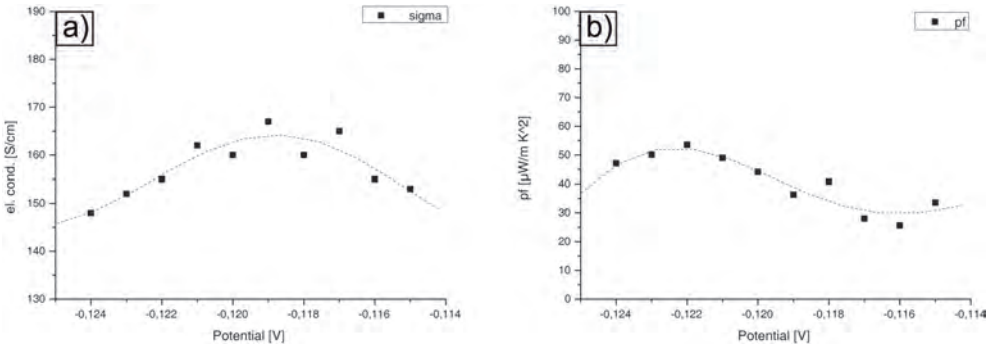

Figure 5.8: Electrical properties of Bi_2Te_3 films pulsed deposited (10/50 ms) vs. deposition potential, (a) electrical conductivity, (b) power factor; lines are guides to the eye

increases with the square of S, this is most likely due to the low Seebeck coefficients of the films presented in fig. 5.5. However, the margin of deviation of pf remains moderate for films deposited with best working deposition potentials around -0.12 V vs. Ag/AgCl/KCl (sat.), indicating a reliable and and repeatable deposition method.

5.2 Ternary $Bi_2(Te_xSe_{1-x})_3$

In order to optimize the thermoelectric performance of Bi_2Te_3, further doping of the material may lead to increases of the electrical properties. The doping is performed by adding Se to be an electron donor in order to increase the amount of charge carriers in the semiconductor.
The crystal structure of $Bi_2(Te_xSe_{1-x})_3$ is identical to Bi_2Te_3 with Se atoms randomly occupying Te lattice spaces. Since one of the valence electrons of each Se atom remains without a binding process to the nearby Te atoms. Thus, the (quasi) free electron may contribute directly to the electrical conduction of the semiconductor.

5.2.1 Structural Properties

The morphology of $Bi_2(Te_xSe_{1-x})_3$ is pretty much similar to that of Bi_2Te_3, the SEM pictures of the films' surface presented in fig. 5.9 show the same characteristic needlelike structure. This is consistent to the deposition mechanism to be reported similar for both materials. [MGSP+03]
The composition of the $Bi_2(Te_xSe_{1-x})_3$ films are quite homogeneous over a wide range of deposition potentials. Thus, the optimization of the

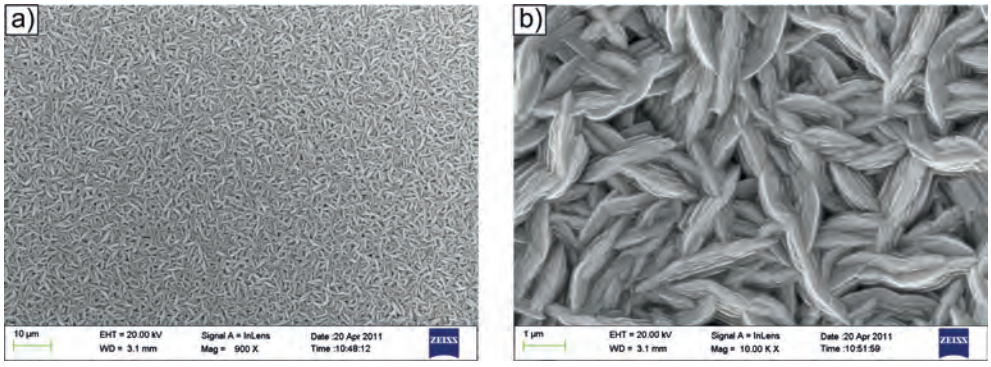

Figure 5.9: SEM-pictures of the surface of $Bi_2(Te_xSe_{1-x})_3$ films electrodeposited with pulsed deposition technique (10/50 ms), (a) magnification 0.9k, (b) magnification 10k

ternary materials' composition cannot be performed by a variation of the deposition potential, as with the deposition of binary Bi_2Te_3, but the composition of the electrolyte used for the electrochemical deposition has to be optimized in order to realize ideal stoichiometry of the materials. However, this type of optimization is much more complicated and time-consuming. Although the films' compositions do not change too much with the deposition potential, the Seebeck coefficients exhibit slightly increased values at potentials of around -0.21 V vs. Ag/AgCl (compare fig. 5.10). This may be due to increased morphology at films deposited with higher electrochemical overpotential.
The X-Ray diffraction pattern displayed in fig. 5.11 exhibit a preferred orientation in (110) direction, the ratio $\frac{I_{(015)}}{I_{(110)}}$ is calculated to ≈ 0.5. Thus, the morphology and crystal structure of both Bi_2Te_3 and $Bi_2(Te_xSe_{1-x})_3$ is - as expected - proven to be almost similar.

	Bi_2Te_3	$Bi_2(Te_xSe_{1-x})_3$	Bi_2Te_3
	pulsed dep. (10/50 ms)		bulk [Row95]
a $\left[\mathring{A}\right]$	4.392	4.3735	4.3835
c $\left[\mathring{A}\right]$	30.213	30.6239	30.360
crystal size $[nm]$	523	275	

Table 5.4: Lattice parameter of Bi_2Te_3 and $Bi_2(Te_xSe_{1-x})_3$ - calculated from XRD pattern

In figure 5.12, a high resolution TEM image of a pulsed deposited $Bi_2(Te_xSe_{1-x})_3$ film is presented. The material exhibits a high degree of crystallinity and

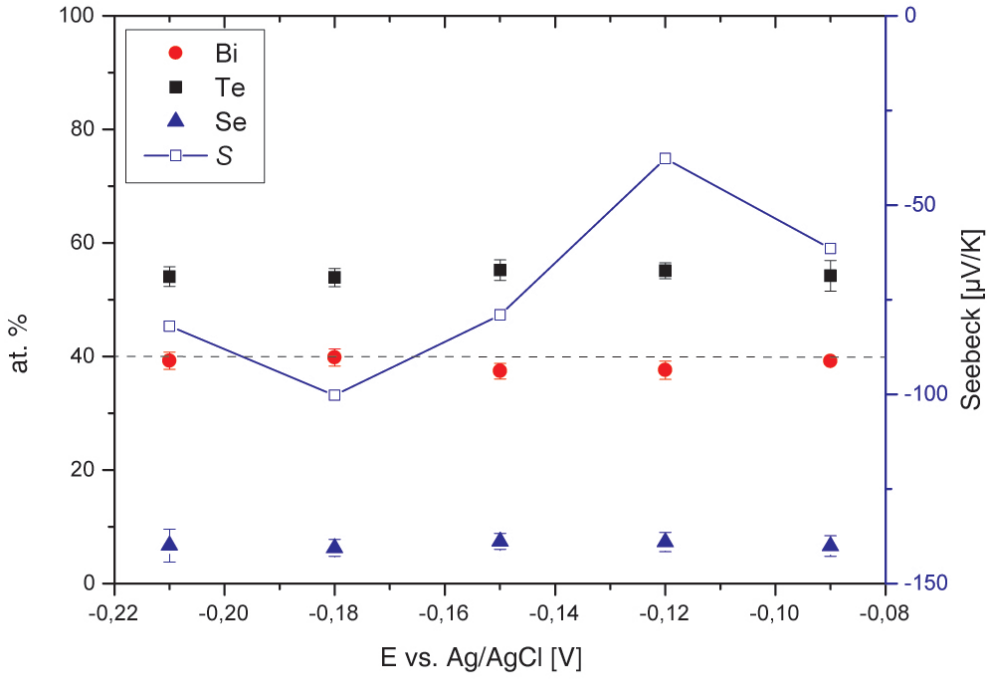

Figure 5.10: Composition and Seebeck coefficients of $Bi_2(Te_xSe_{1-x})_3$ films electrodeposited with pulsed deposition technique (10/50 ms)

a homogneous crystal structure over a large surface area. More information of the TEM analysis can be found in the appendix (A).
The lattice parameters (tab. 5.4) are calculated from the pattern exhibiting comparable values with moderate disparity caused by crystallographic imperfectness and certain unstability of process parameters during the electrochemical deposition (compare chapt. 3).

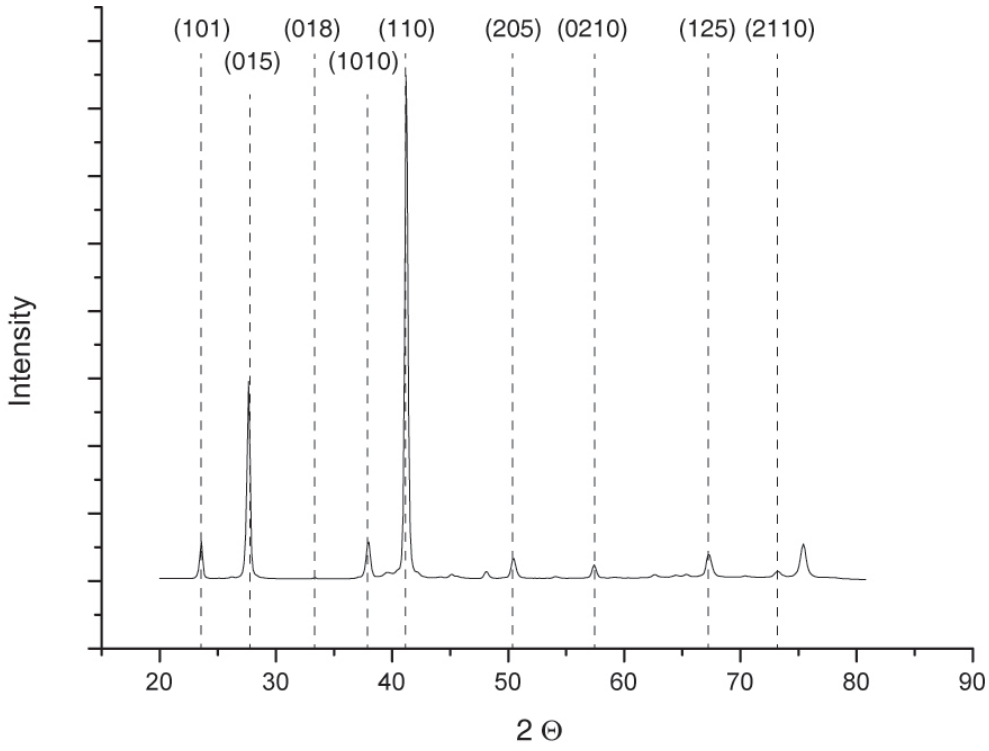

Figure 5.11: X-Ray diffraction pattern of $Bi_2(Te_xSe_{1-x})_3$ films electrodeposited with pulsed deposition technique (10/50 ms)

5.2.2 Transport Properties

As expected, the charge carrier density of Bi_2Te_3 significantly increases by adding Se as an electron donator. More free electrons are available at the conduction band and contribute to the electrical conductivity.
The charge carrier mobilities of $Bi_2(Te_xSe_{1-x})_3$ also is increases compared to those of Bi_2Te_3. Since a high mobility is suspect to denote a high degree of crystallinity, the ternary compound should exhibit less electron scattering processes, e.g. at grain boundaries.

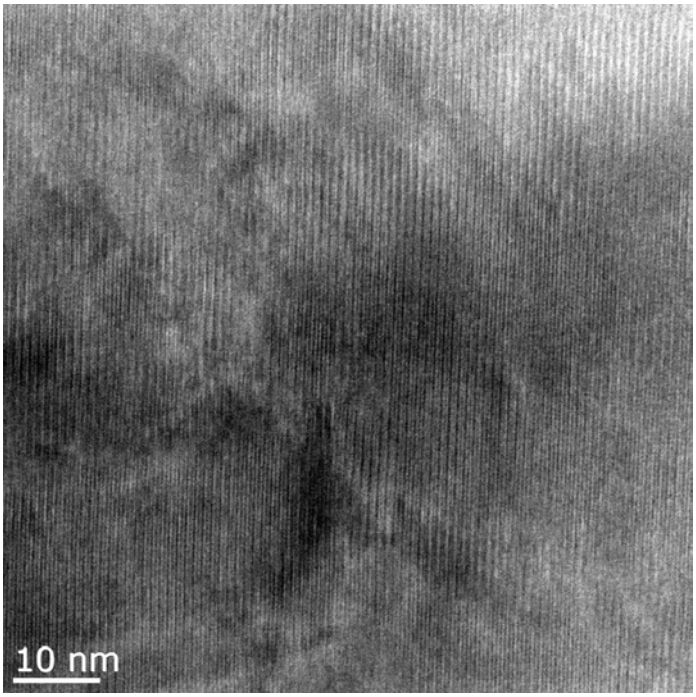

Figure 5.12: High resolution TEM image of a $Bi_2(Te_xSe_{1-x})_3$ film pulsed deposited (10/50 ms) [MPI]

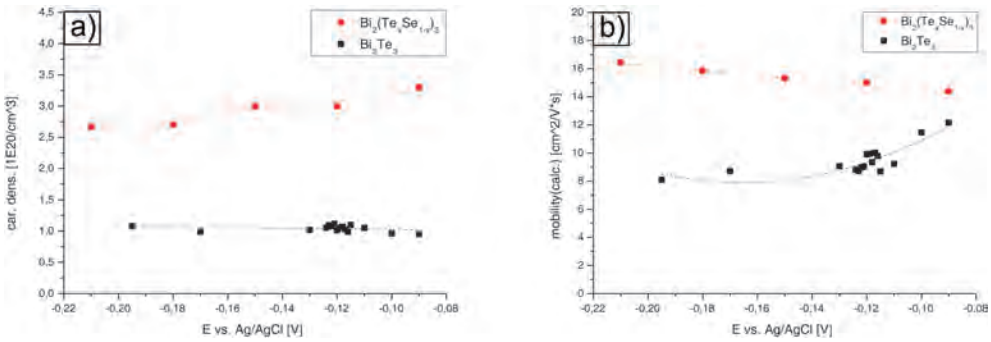

Figure 5.13: Electrical properties of Bi_2Te_3 and $Bi_2(Te_xSe_{1-x})_3$ films pulsed deposited (10/50 ms) vs. deposition potential, (a) charge carrier density (electrons), (b) charge carrier mobility; lines are guides to the eye

5.2.3 Thermoelectric Performance

Since both the charge carrier density and the mobility strongly increase by doping Bi_2Te_3 with Se, the electrical conductivity also exhibits considerable improvements of about 7 times the initial value for Bi_2Te_3. (fig.

5.14 (a)).

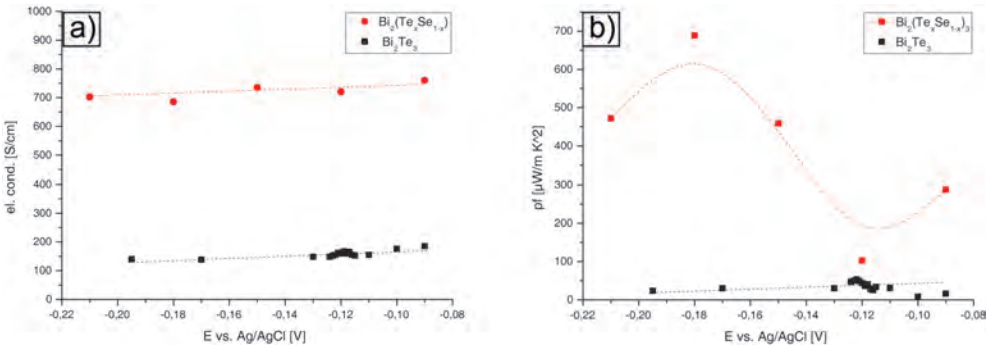

Figure 5.14: Electrical properties of Bi_2Te_3 and $Bi_2(Te_xSe_{1-x})_3$ films pulsed deposited (10/50 ms) vs. deposition potential, (a) electrical conductivity, (b) power factor; lines are guides to the eye

The power factors (fig. 5.14 (b) show huge increases compared to Bi_2Te_3. Consistent to the deposition potentials determined to be best for the electrochemical deposition of $Bi_2(Te_xSe_{1-x})_3$ (compare fig. 3.4), the best performing materials are found for E ≈ -0.21 V vs. Ag/AgCl. The power factors are almost one order of magnitude higher for ternary $Bi_2(Te_xSe_{1-x})_3$ compared to binary Bi_2Te_3.

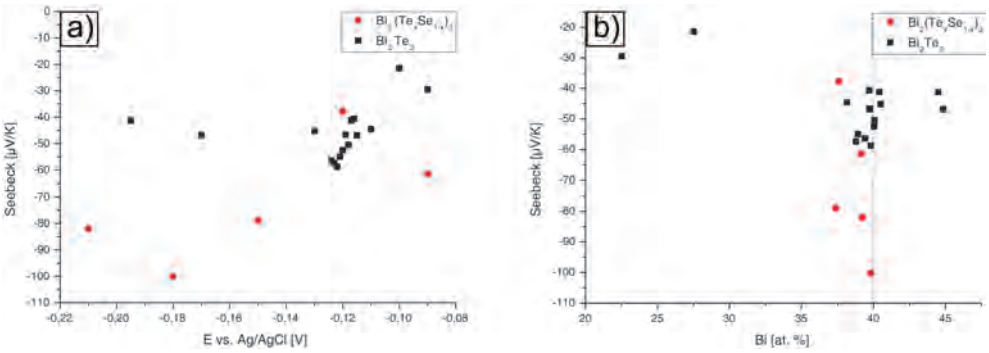

Figure 5.15: Seebeck coefficients of Bi_2Te_3 and $Bi_2(Te_xSe_{1-x})_3$ films pulsed deposited (10/50 ms), (a) vs. deposition potential, (b) vs. composition; lines are guides to the eye

In consistence, the Seebeck coefficients of ternary compounds also exhibit significantly higher values than those of Bi_2Te_3 for materials deposited around -0.21 V vs. Ag/AgCl (compare fig. 5.15 (a)). As discussed above, the deposition of Bi_2Te_3 seems to work best, since the Seebeck coefficients

exhibit the highest values. For ternary compounds, the Seebeck coefficients are comparable to those of Bi_2Te_3 in this potential range. Thus, the deposition potential tends to significantly shift to more negative potentials for ternary potentials. This is consistent to the discussions above. In fig. 5.15 (b), the Seebeck coefficients of both materials are presented in dependence on the composition of the compounds. Both materials the binary and the ternary compounds exhibit best Seebeck coefficients for almost ideal composition of 40 at. %.

Most of the ternary compounds are slightly Te/Se-rich. However, the data prove the best working samples for $Bi_2(Te_xSe_{1-x})_3$ (deposited at E=-0.21 V vs. Ag/AgCl/KCl (sat.) - compare above) also are of almost ideal stoichiometry at 39.95 at. % of Bi.

		Bi_2Te_3 puls-dep. (10/50 ms)	$Bi_2(Te_xSe_{1-x})_3$ puls-dep. (10/50 ms)
σ	$[Scm^{-1}]$	158	700
S	$[\mu VK^{-1}]$	-60	-80
pf	$[\mu WK^{-2}m^{-1}]$	57	448
κ (RT)	$[WK^{-1}m^{-1}]$	0.9	1.2
ZT(RT)		0.02	0.11

Table 5.5: Thermoelectric performance of Bi_2Te_3 and $Bi_2(Te_xSe_{1-x})_3$ films pulsed deposited (10/50 ms)

In table 5.5, the thermoelectric performances of selected samples are presented. As already discussed above, the performance of n-doped ternary compounds is significantly higher (about 5 times higher) compared to that of binary n-doped material. Thus, subsequently, the deposition of ternary compounds becomes the standard for the following chapters.
The materials presented here exhibit significantly higher thermoelectric performances compared to results presented in the literature. [BBC+09], [MBL96], [LTS+06], since the values of Seebeck and σ exhibit improvements of around 30 %.
The material exhibits a thermopower of about 25% (Bi_2Te_3) and 60 % ($Bi_2(Te_xSe_{1-x})_3$) of nanograin bulk materials.[TXL+07] [YPM+10] The thermal conductivity is comparable to bulk values (105 %). Using the Wiedemann Franz law (eq. 2.8), the thermal conductivity can be discussed in more detail:

$$\kappa = \kappa_{lat.} + \kappa_{el}$$

$$\kappa_{el} = L\sigma T$$

Thus, the electronic part κ_{el} contributing to κ can be determined to be 13 % (Bi_2Te_3) and 42 % (($Bi_2(Te_xSe_{1-x})_3$) of the total thermal conductivity. This is provided that the Lorentz factor L the free electrons is correct. Due to the high charge carrier density, this assumption may be allowed, although mixed conduction may distort the value for L at temperatures between 300-400 K.
Further improvements may be obtained by thermal treatment of the thermoelectric material, thus, a detailed comparison of the best materials obtained in this work to best results reported in the literature is given in chapt. 7.

In order to realize materials, that can easily transferred to applications, such as microstructured thermogenerators, the development of p-doped material is required. The results are shown subsequently in chapt. 6.

Chapter 6

P-doped Materials

As already mentioned, the successful integration of the thermoelectric materials into microgenerators requires both n-doped and p-doped materials. Thus, binary and ternary p-doped Sb_2Te_3 and $(Bi_xSb_{1-x})_2Te_3$ films are characterized subsequently.

In order to ensure the conditions found in chapt. 2 and 5 are valid for p-doped materials with positive holes as the majority charge carriers, too, some facts about p-doped semiconductors have to be recapitulated.
With the consideration of p-doped semiconductors, the calculations can be performed analogue to n-doped materials. The total amount of (negative) charge carriers has been given by eq. 5.2 for n-doped materials above.
Now, with p-doped semiconductors, the Fermi-level is close to the edge of the valence band, as shown in fig. 5.1 (d). Thus, there are some empty states in the valence band, which cause them to contribute to the electrical conduction. The effective mass m^* turns out to be negative then, although the process is still due to electrons [Gol09]. This effect then is understood by changing the carriers' charge to positive $\rightarrow$ positive holes with, also positive, effective masses. Thus, one can understand the electrical conduction in p-doped semiconductors to be performed by "positive holes", which total amount p can be calculated by:

$$p = \int_0^\infty \frac{4\pi(2m^*)^{\frac{3}{2}}}{h^3(1+e^{\frac{E-E_f}{k_BT}})} dE \tag{6.1}$$

The behavior of positive holes in an external magnetic or electric field is analogue to electrons with a virtual positive charge. [Kit02] This can be explained by the consistency of electrons and holes:

Wave Vector: Electrons exhibit the wave vector $\vec{k}_e$. Once they relocate to the the conduction band by e.g. direct optical passing of the band

gap, a photon with E=$\hbar\omega$ is absorbed and the entire wave vektor of the valence band then is -$\vec{k}_e$. Since this is only related to the hole, originated by the missing electron in the valence band, the wave vector of the hole can be assigned to: $\vec{k}_h = -\vec{k}_e$

Energy: As long as the band structure remains symmetrically, the energy of the electron abandoned from the valence band is constant after relocating to the conductance band: $\epsilon_e(\vec{k}_e) = \epsilon_e(-\vec{k}_e)$ Since the the energy of electrons and holes (caused by electrons) is identical, the absolute value of the energy of electrons is equal to that of holes, but with opposite sign:

$$\epsilon_e(\vec{k}_e) = \epsilon_e(-\vec{k}_e) = -\epsilon_h(-\vec{k}_e) = -\epsilon_h(-\vec{k}_h)$$

$$\epsilon_e(\vec{k}_e) = -\epsilon_h(-\vec{k}_h) \tag{6.2}$$

Velocity: The velocity $\upsilon = \frac{d\omega}{d\vec{k}}$ can be written as $\upsilon = \frac{d\epsilon}{\hbar d\vec{k}}$ by using $\omega = \frac{\epsilon}{\hbar}$. Thus, the velocity is:

$$\vec{v} = \frac{\nabla_{\vec{k}}\,\epsilon(\vec{k})}{\hbar}$$

As discussed above, the absolute values of the energy of electrons and holes are identical, from eq. 6.2, one can find

$$\nabla\epsilon_e(\vec{k}_e) = \nabla\epsilon_h(\vec{k}_h)$$

Effective Mass: From $\epsilon = (\underbrace{\frac{\hbar^2}{2m}}_{\mathrm{C}})k^2$ for free electrons [Kit02], it´s obvious, that C affects the 2$^{\mathrm{nd}}$ derivation of $\epsilon(k)$. In consistence, one can say $\frac{1}{m}$ affects the bending of $\epsilon(k)$. For small band gaps, at the border of the Brillouin zone, the bending of the bands are huge. If the band-gap ΔE is small compared to the energy ϵ of the free electron (and the width of a band), the bending is affected to increase by $\frac{\epsilon}{\Delta E}$, realizing effective masses of 0.1 or smaller. Farther away from the band-gap, the beding decreases and the effective mass aligns to that of a free electron.
The energy of an electron near the lower edge of the upper band is [Kit02]

$$\epsilon(k) = \epsilon + (\frac{\hbar^2}{2m_e})k^2 \rightarrow \frac{m_e}{m} = \frac{1}{(\frac{2\epsilon}{U}) - 1},$$

with the potential energy U and the effective mass for an electron m_e. For an electron near the upper edge of the lower band, it is:

$$\epsilon(k) = \epsilon - (\frac{\hbar^2}{2m_h})k^2 \rightarrow \frac{m_h}{m} = \frac{1}{(\frac{2\epsilon}{U}) + 1}$$

and therefore, one can find

$$m_h = -m_e.$$

Based on the considerations above, the transport processes of both p- and n-doped semiconductors can be understood by the same equations, but since the conduction takes place in the conduction band with reference to electrons for n-doped materials and in the valence band with reference to the positive holes for p-doped materials, the energy E has to be determined in different ways from the Fermi-level - upwards or downwards, respectively.

6.1 Binary Sb_2Te_3

Sb_2Te_3 is a narrow band gap ($\Delta E \approx 0.3$ eV [JM11]) and has the same structure as Bi_2Te_3, with Sb atoms occupying the Bi lattice sites. Thus, it exhibits almost similar physical properties. Sb_2Te_3 also crystallizes in the $R\bar{3}m$ point group and the cell also is build from multiple layers perpendicular to the c-axis (compare fig. 5.2 for Bi_2Te_3), although the mass of Sb is smaller than that of Bi_2Te_3.
Electrical conduction in p-doped Sb_2Te_3 takes place by positive holes in the valence band as discussed above. Thus, Sb_2Te_3 is of high interest as a p-doped counterpart to Bi_2Te_3 to work in thermoelectric (micro)devices and -generators. Amorphous Sb_2Te_3 also is of high interest for phase change applications, since it tends to become crystalline above around 120°C, and therefore is deposited by various deposition techniques such as MBE, vapor techniques and also by electrochemical deposition.[HKR08] [JPL+10] [JM11]
As Bi_2Te_3, Sb_2Te_3 also exhibits it´s thermoelectric peak performance around 300 K (compare fig. 2.2 (b)) and therefore is a proper candidate for all types of applications at room temperature. Parts of the following chapter already have recently been published by the authors.

6.1.1 Structural Properties

SEM pictures of Sb_2Te_3 are presented in fig. 6.1 - the cross section of a pulsed deposited (10/50 ms) material (a) shows a smooth surface

and a homogeneous growth of the layer on top of the Pt seed layer. Also the top view in fig. 6.1 (b) proves the surface to be smooth, since the characteristic needlelike structure is observable, comparable to the structure of binary and ternary Bi_2Te_3 compounds presented in chapt. 5.

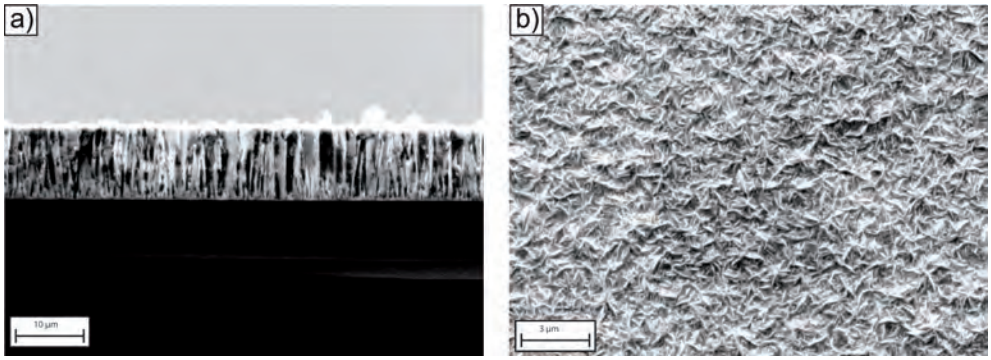

Figure 6.1: SEM-pictures of Sb_2Te_3 films electrodeposited with pulsed deposition technique (10/50 ms), (a) cross-section, (b) surface

X-Ray diffraction pattern presented thereby exhibit the main characteristic peaks with the preferred orientation to be in (015) direction with $\frac{I_{(015)}}{I_{(110)}} \approx 1.5$ (DC) and ≈ 2.7 for pulsed deposited films.

	DC	pulsed deposited (10/50 ms)	Sb_2Te_3 bulk [Row95]
a $\left[\mathring{A}\right]$	4.271	4.263	4.264
c $\left[\mathring{A}\right]$	28.730	30.323	30.428
crystal size $[nm]$	137	637	

Table 6.1: Lattice parameter of Sb_2Te_3 films - calculated from XRD pattern

The lattice parameters presented in table 6.1 are accordingly to the bulk values of Sb_2Te_3. The DC deposited films show a shortened unit cell in c-direction and about 5 times lower crystal size compared to that of pulsed deposited films, likely due to crystal imperfectness during the electrodeposition process, that may caused by the constant voltage and therefore high current density applied.

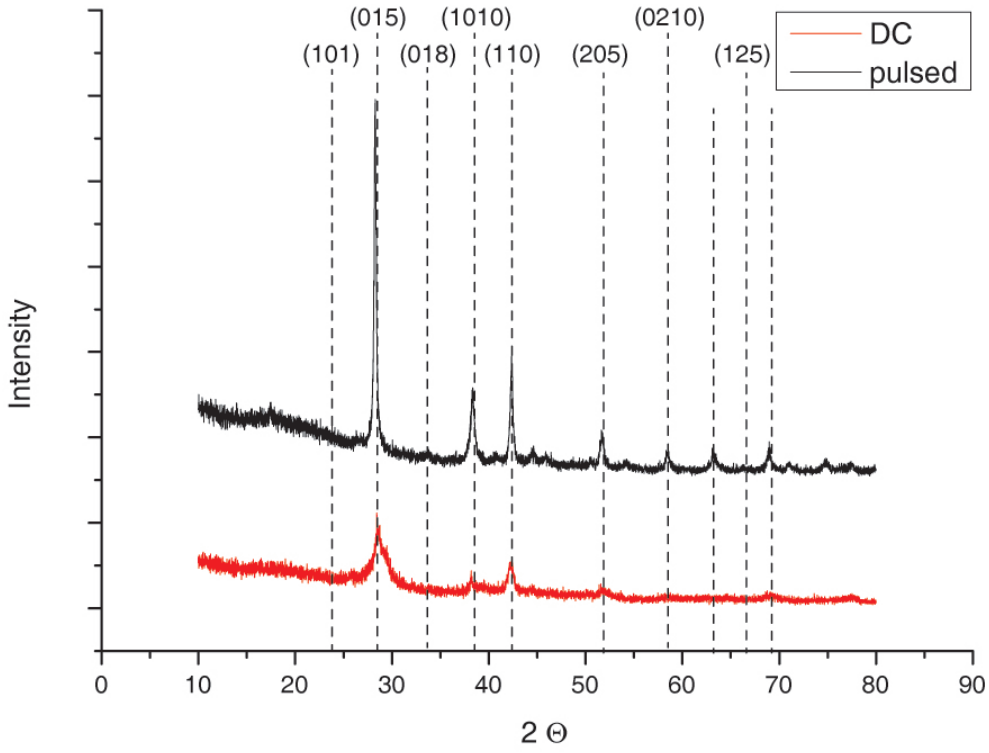

Figure 6.2: Comparison of both DC and pulsed deposited Sb_2Te_3 films' XRD pattern - deposited at E=-0.42 V vs. Ag/AgCl

6.1.2 Transport Properties

In fig. 6.4, the charge carrier density (a) and the charge carrier mobility (b) of pulsed deposited Sb_2Te_3 films are presented. The pulsed deposition method proves good reliability by a homogeneous distribution of compositions over a wide range of E. Almost the ideal composition is found for deposition potentials between -0.32 to -0.46 V with respect to the Ag/AgCl reference. However, a significant increase of the Seebeck coefficient is achieved at E around -0.36 V vs. Ag/AgCl.
The charge carrier (holes) density presented in fig.6.4 (a) is distributed quite homogeneous over the whole range of deposition potentials, the deviances are within $0.2 \cdot 10^{20} \frac{1}{\mathrm{cm}^3}$.

The charge carriers' mobility (shown in fig. 6.4 (b)) exhibits deviations between about 13 to 18 $\frac{\mathrm{cm}^2}{\mathrm{Vs}}$, indicating a high crystallinity, since the mobility of binary Sb_2Te_3 is about 2 times higher compared to binary Bi_2Te_3 (compare fig.5.7 (b)). The mobility is slightly higher than reported for electrochemically deposited chalcogenides before (10-14 $\frac{\mathrm{cm}^2}{\mathrm{Vs}}$), but only

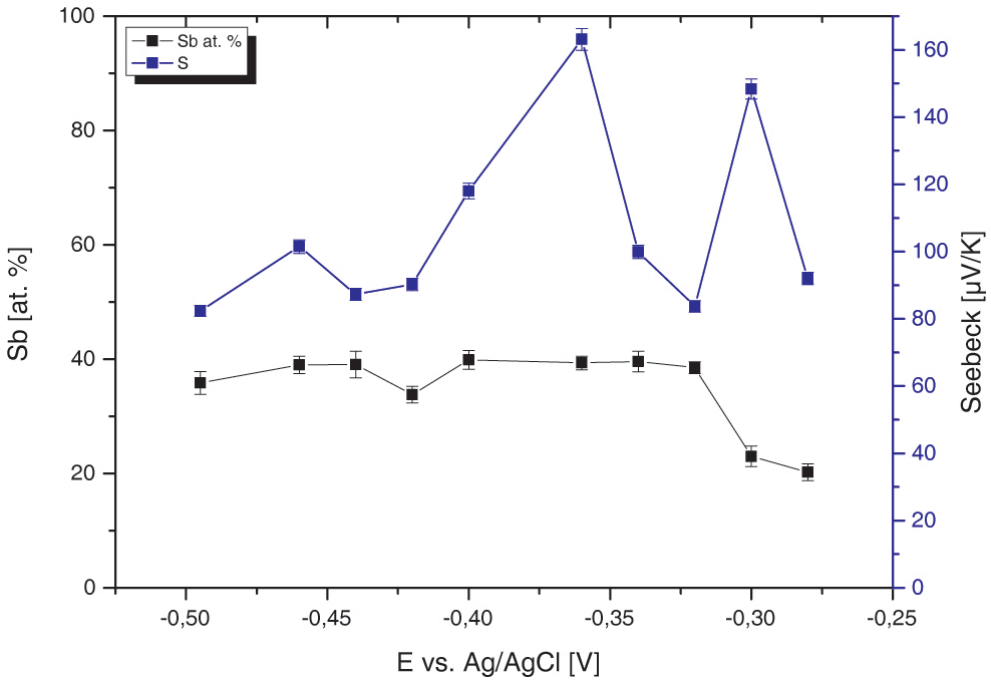

Figure 6.3: Composition and Seebeck coefficients of Sb_2Te_3 films electrodeposited with pulsed deposition technique (10/50 ms)

about 20 % of values reported for nanograined bulk. [Row06]

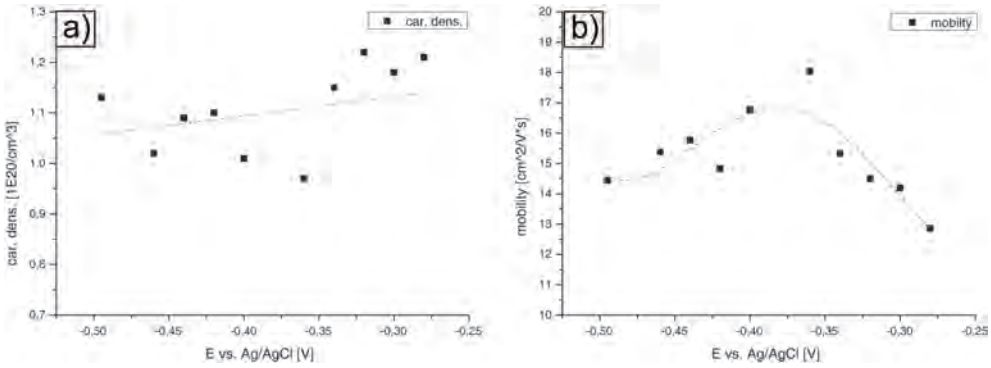

Figure 6.4: Electrical properties of Sb_2Te_3 films pulsed deposited (10/50 ms) vs. deposition potential, (a) charge carrier density (electrons), (b) charge carrier mobility; lines are guides to the eye

6.1.3 Thermoelectric Performance

The electrical conductivity (fig. 6.5 (a))show moderate variations over the whole range of deposition potentials. The fluctuations are below 10 % around absolute values of 260 $\frac{S}{cm}$. Since these values are about 30 % higher compared to Sb_2Te_3, this is consistent with the fact, that Sb_2Te_3 is found to exhibit higher values compared to BI_2Te_3 as discussed above. Due to the increased electrical conductivity and Seebeck coefficient, the power factor (fig. 6.5 (b)) strongly increases, leading to a significantly improved thermoelectric performance of binary p-doped Sb_2Te_3.

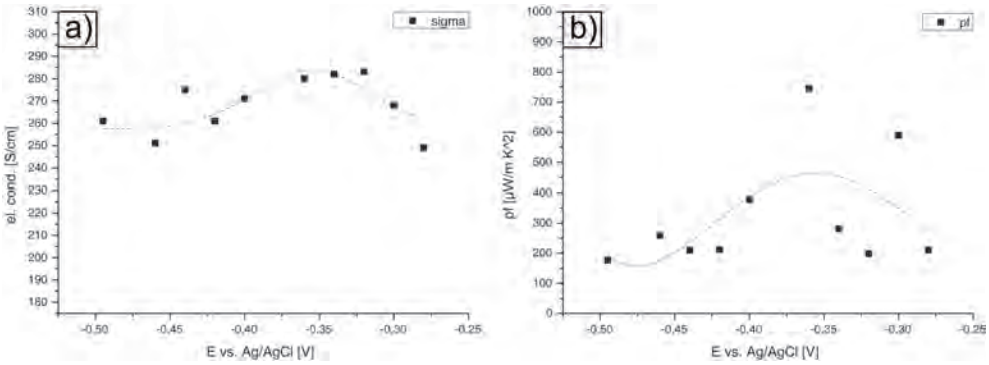

Figure 6.5: Electrical properties of Sb_2Te_3 films pulsed deposited (10/50 ms) vs. deposition potential, (a) electrical conductivity, (b) power factor; lines are guides to the eye

		Sb_2Te_3 pulsed dep. (10/50 ms)
σ	[Scm^{-1}]	280
S	[μVK^{-1}]	161
pf	[$\mu WK^{-2}m^{-1}$]	726
κ (RT)	[$WK^{-1}m^{-1}$]	1.0
ZT(RT)		0.21

Table 6.2: Thermoelectric performance of Sb_2Te_3

6.2 Ternary $(Bi_xSb_{1-x})_2Te_3$

Significant improvements of the thermoelectric performance of binary Sb_2Te_3 compounds may be realized by doping of the material with bismuth atoms. Thus, the transport parameters such as σ and S may increase due to an increased charge carrier density p.

6.2.1 Structural Properties

SEM pictures of $(Bi_xSb_{1-x})_2Te_3$ are presented in fig. 6.6. Both the cross-section (a) as well as the top-view (b) prove a good crystallinity and homogeneity of the deposited materials, the grain size of $(Bi_xSb_{1-x})_2Te_3$ is slightly increased compared to Bi_2Te_3. Since the control of the deposition of ternary materials is mainly realized by optimization of the electrolyte bath, the morphology of the films may not be optimized by variation of the deposition potential, like it was possible with the deposition of binary compounds.

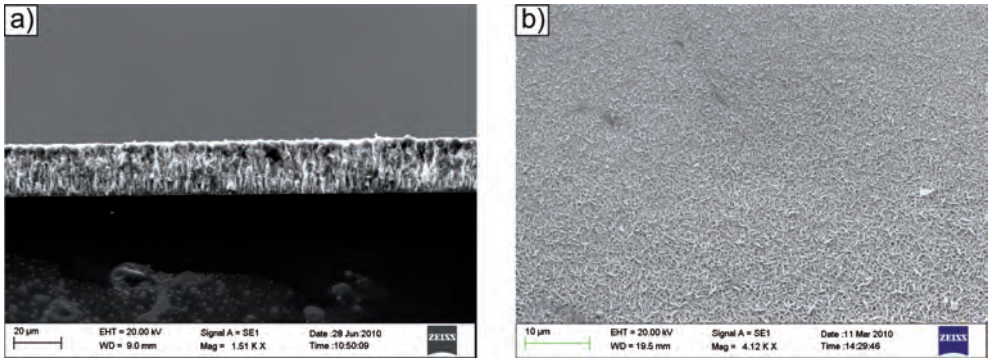

Figure 6.6: SEM-pictures of $(Bi_xSb_{1-x})_2Te_3$ films electrodeposited with pulsed deposition technique (10/50 ms), (a) cross-section, (b) surface

In fig. 6.7, the XRD pattern of both the DC- and the pulsed deposited $(Bi_xSb_{1-x})_2Te_3$ films are presented. Analogue to DC deposited Bi_2Te_3 and $Bi_2(Te_xSe_{1-x})_3$, the preferred orientation of DC deposited $(Bi_xSb_{1-x})_2Te_3$ films is also (110), since $\frac{I_{(015)}}{I_{(110)}} \approx 0.5$.
For pulsed deposited films, the preffered orientation is (015) with $\frac{I_{(015)}}{I_{(110)}} \approx 1.2$. This is most likely due to the not optimized deposition parameters during the DC deposition. Since the DC deposition does not show promising results in terms of morphology, it has not been optimized too far in terms of composition. Therefore, very high current densities may occur during the deposition process, leading to imperfect crystal growth.

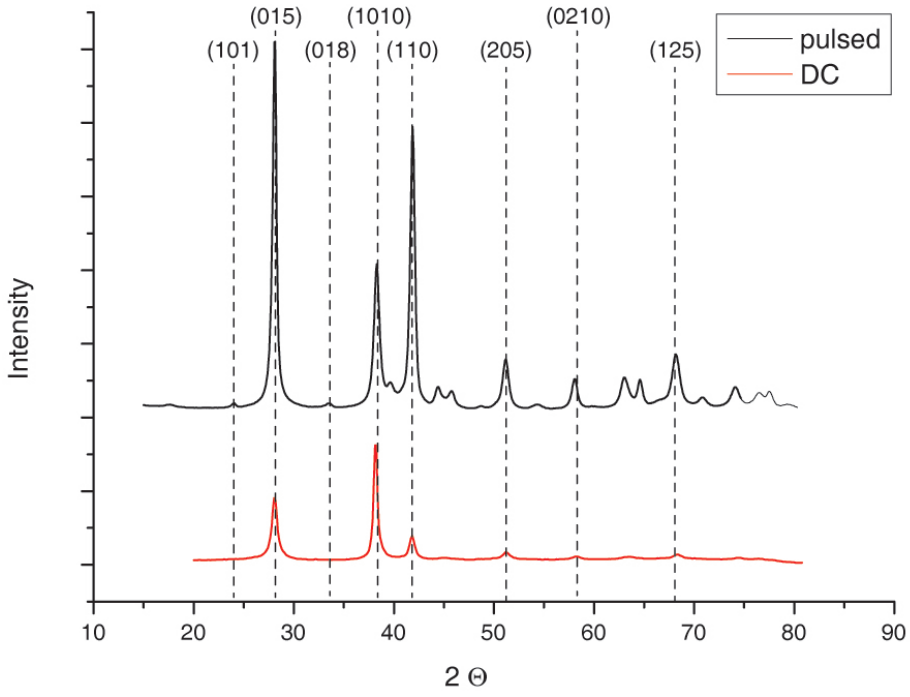

Figure 6.7: Comparison of both DC and pulsed deposited $(Bi_xSb_{1-x})_2Te_3$ films' XRD pattern

	DC deposited (10/50 ms)	pulsed deposited (10/50 ms)	$(Bi_xSb_{1-x})_2Te_3$ bulk [Row95]
a $[\mathring{A}]$	4.275	4.299	4.295
c $[\mathring{A}]$	30.215	30.4262	30.350
crystal size $[nm]$	275	326	

Table 6.3: Lattice parameter of $(Bi_xSb_{1-x})_2Te_3$ films - calculated from XRD pattern

In figure 6.8, a high resolution TEM image of a pulsed deposited $(Bi_xSb_{1-x})_2Te_3$ film is presented. The material exhibits a high degree of crystallinity and a homogneous crystal structure over a large surface area. More information about TEM analysis can be found in the appendix A.
The lattice parameters of $(Bi_xSb_{1-x})_2Te_3$ presented in tab. 6.3 show comparable values for a reported for electrochemical deposited films (a=4.27-4.29)[RDB10]. On the other hand, the cell-size in c-direction reported in this work by Richoux et al. is determined to c=29.91-30.26, what is actually far away from the theoretical values.[Row06][RDB10] In contrast, the

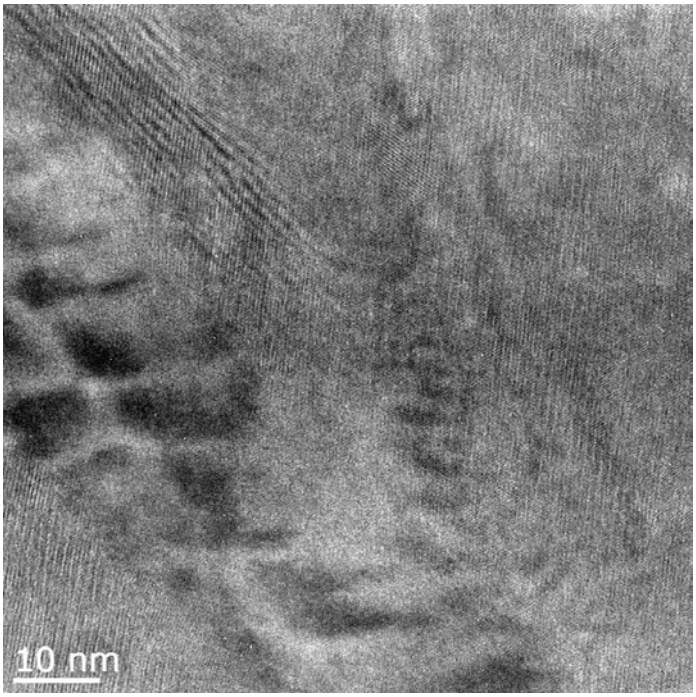

Figure 6.8: High resolution TEM image of a $(Bi_xSb_{1-x})_2Te_3$ film pulsed deposited (10/50 ms) [MPI]

lattice parameters determined in this work (presented in tab.6.3) show very good accordance to the bulk values reported in [Row95]. Thus, the deposition of ternary $(Bi_xSb_{1-x})_2Te_3$ is proven to be successful in terms of morphology and crystal structure.

6.2.2 Transport Properties

The charge carrier density of Sb_2Te_3 and $(Bi_xSb_{1-x})_2Te_3$ films is shown in fig. 6.9 (a). Due to the doping by Bi as an electron acceptor, more electrons are fixed to bondings and therefore more positive holes are located in the valence band. Thus, the charge carrier density increases for ternary $(Bi_xSb_{1-x})_2Te_3$ compared to binary Sb_2Te_3.
Since the charge carrier mobility for $(Bi_xSb_{1-x})_2Te_3$ shows significantly increases (fig.6.9 (b)) up to about 160 % of the value for Sb_2Te_3, the quality of the crystal structure also seems to be improved, although the crystal size of the ternary compounds exhibits increases of not more than 17 %.

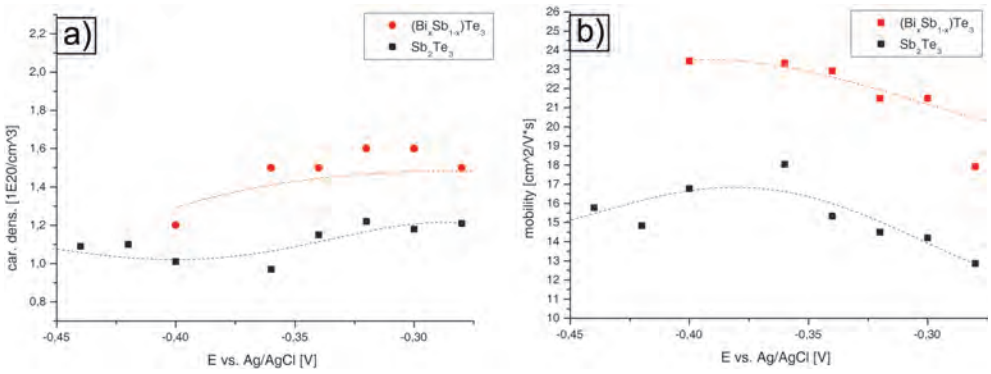

Figure 6.9: Electrical properties of Sb_2Te_3 and $(Bi_xSb_{1-x})_2Te_3$ films pulsed deposited (10/50 ms) vs. deposition potential, (a) charge carrier density (electrons), (b) charge carrier mobility

6.2.3 Thermoelectric Performance

In consistence to the increased charge carrier density and -mobility, the electrical conductivity of ternary $(Bi_xSb_{1-x})_2Te_3$ also increases up to around 2 times the value for binary Sb_2Te_3 as shown in fig. 6.10 (a).

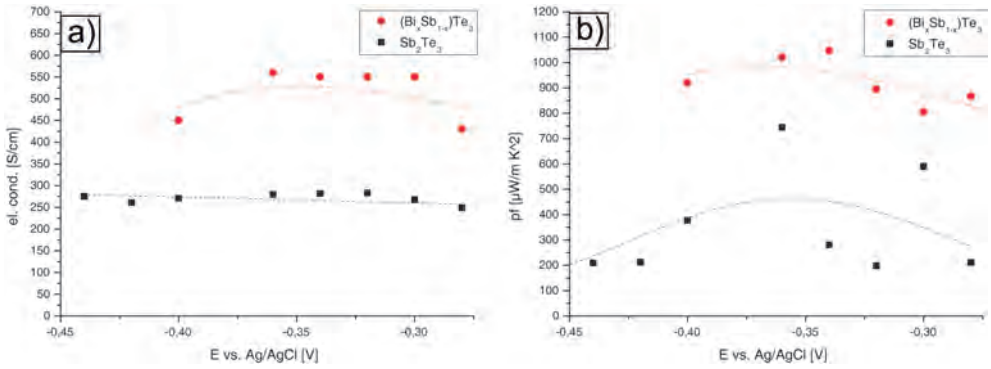

Figure 6.10: Electrical properties of Bi_2Te_3 and $(Bi_xSb_{1-x})_2Te_3$ films pulsed deposited (10/50 ms) vs. deposition potential, (a) electrical conductivity, (b) power factor; lines are guides to the eye

At the same time, the distribution is homogeneous, since the values' deviation is small for the whole range of deposition potentials. This is consistent to the discussion above, that the depositions' quality is less dependent on the deposition potential for ternary compounds than for binary compounds.
The power factor of both the binary and ternary p-doped materials is presented in fig. 6.10 (b), exhibiting the ternary compounds - as expected

- to be significantly higher. The power factor of ternary $(Bi_xSb_{1-x})_2Te_3$ exhibits values up to about 1100 $\frac{\mu W}{mK^2}$, while the average for binary Sb_2Te_3 is at around 300 $\frac{\mu W}{mK^2}$.

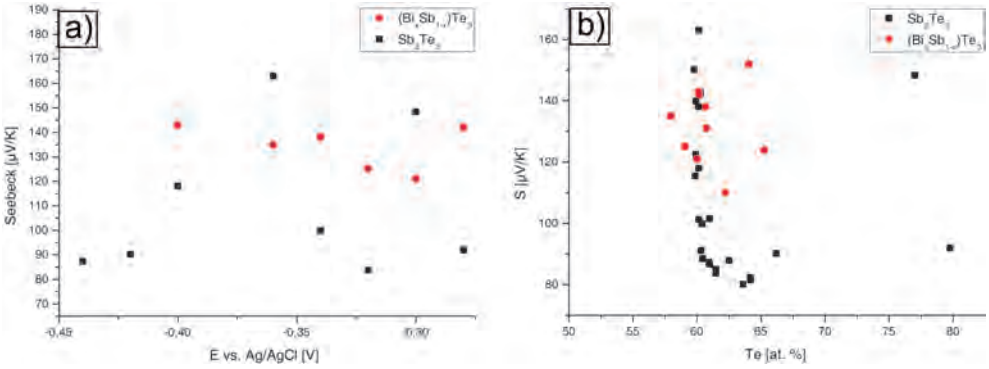

Figure 6.11: Seebeck coefficients of Bi_2Te_3 and $(Bi_xSb_{1-x})_2Te_3$ films pulsed deposited (10/50 ms), (a) vs. deposition potential, (b) vs. composition; lines are guides to the eye

In fig. 6.11 (a), the Seebeck coeffients are presented in more detail. In principle, the ternary compounds exhibit higher Seebeck values compared to the binary compounds, although here some Seebeck coefficients for Sb_2Te_3 are actually higher. If S is plotted in function of the composition of the compounds (fig. 6.11 (b)), a strong dependence of Seebeck coefficient to the composition is observed. For binary Sb_2Te_3, the Seebeck coefficients are significantly higher, once the material exhibits almost ideal stoichiometry.

		Sb_2Te_3	$(Bi_xSb_{1-x})_2Te_3$
		pulsed dep. (10/50 ms)	
σ	$[Scm^{-1}]$	280	560
S	$[\mu VK^{-1}]$	161	135
pf	$[\mu WK^{-2}m^{-1}]$	726	1020
κ (RT)	$[WK^{-1}m^{-1}]$	1.0	1.1
ZT(RT)		0.21	0.28

Table 6.4: Thermoelectric performance of Sb_2Te_3 and $(Bi_xSb_{1-x})_2Te_3$ films pulsed deposited (10/50 ms)

For ternary $(Bi_xSb_{1-x})_2Te_3$ films, there is also a trend observed for ideal composition, although Te rich films exhibit comparable high Seebeck coefficients as well. The dependence of thermoelectric performance on the composition of the materials is analysed in more detail in chapt. 7.

In table 6.4, the thermoelectric performances of selected samples are presented. Similar to the n-doped material discussed in chapt. 5, the p-doped ternary compounds exhibit significantly improved thermoelectric performances.

The material exhibits a thermopower comparable to that of nanostructured bulk materials: 77% of bulk (Sb_2Te_3) [PHM$^+$08] [MHP$^+$08] and 59 % ($Bi_2(Te_xSe_{1-x})_3$) [XTY$^+$09]. The thermal conductivity is comparable to bulk (110 %). As already discussed in chapt. 5.2.3, the thermal conductivity may be analyzed in more detail using the Wiedemann Franz law (eq. 2.8), finding the electronic part κ_{el} to be 20 % (Sb_2Te_3) and 37 % ($(Bi_xSb_{1-x})_2Te_3$). Although the ternary compounds exhibit significantly higher electrical conductivity, the thermal conductivity's increase is small. Thus, the phononic part κ_{lat} decreases, most likely due to significant changes of the crystal structure. Further improvements may be obtained by thermal treatment of the thermoelectric material, thus, a detailed comparison of the best materials obtained in this work to best results reported in the literature is given in chapt. 7.

Now, both the n-doped and the p-doped ternary materials developed exhibit good homogeneity and thermoelectric performance. Although the materials can be used for integration into microdevices in the as deposited state, further improvements may be realized by the thermal treatment of the materials, which will be discussed consecutively in chapt. 7.

Chapter 7

Enhancement of Charge Carrier Density and -Mobility

7.1 Thermoelectric Performance

The physical parameters S, σ and κ are dependent on the temperature, thus the electrodeposited thermoelectric materials are subject to a thermal treatment process in He and Te ambience.
Since the semiconductors' thermoelectric performance is determined from these values, the thermoelectric material may change it's quality with the temperature. In fig. 7.1, this expected behavior for intrinsic semiconductors is presented in dependence on the materials' charge carrier density. With increasing charge carrier density, the Seebeck coefficient S decreases, while the electrical conductivity σ increases. Thus, the thermoelectric power factor (5.6) exhibits a maximum, which is located at charge carrier densities of around 10^{19} to 10^{20} $\frac{1}{\mathrm{cm}^3}$. Since the thermal conductivity κ also increases with T, the maximum of the thermoelectric figure of merit ZT is slightly shifted from the pf-maximum, but remains in this range of charge carrier density. In order to understand this behavior, one has to understand the origin of the parameters contributing to the thermoelectric figure of merit. Consecutively, the dependence on the temperature and charge carrier density/-mobility of all values contributing to the thermoelectric figure of merit are derived from the legal equations given in chapt. 2.

The Boltzmann equation provides information about the occupied states $\vec{k}$ located at $\vec{r}$ at time t by charge carriers. Therefore, it relates the effects of applied fields and the scattering of the charge carriers. If a function f is disturbed from the equilibrium f_0, it will relax back to f_0 correspoding to [Gol09]:

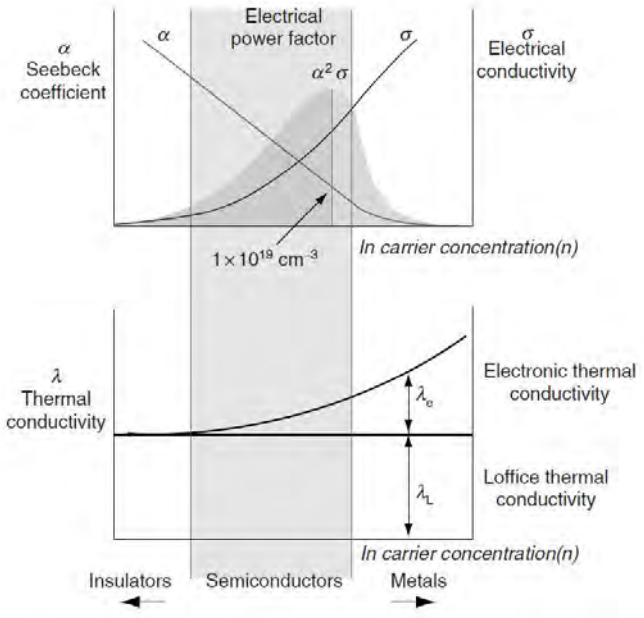

Figure 7.1: Thermoelectric parameter in dependence on the charge carrier concentration [Row06].

$$\frac{df(E)}{dt} = -\frac{f(E) - f_0(E)}{\tau_{e/h}}$$

with the relaxation time $\tau_{e/h}$ of the form $\tau_0 E^r$ for electrons and holes, respectively. In most thermoelectric materials, the scattering of the charge carriers is dominated by the acoustic-lattice vibrations (r=$-\frac{1}{2}$) and by ionised impurities (r=$\frac{3}{2}$). [Gol09] Thus, the reciprocal relaxation time can be added in case that none of the scattering processes is predominant. Small disturbances to F(E) (2.4) can be described with the relation above:

$$\frac{F(E) - F_0(E)}{\tau_{e/h}} = \upsilon \frac{dF_0(E)}{dE}\left(\frac{dF(E_f}{dx} + \frac{(E - E_f)}{T}\frac{dT}{dx}\right) \tag{7.1}$$

with the charge carriers' velocity (x-direction). Then, the electric current density is:

$$i = \mp \int_0^\infty e\upsilon F(E)G(E)dE. \tag{7.2}$$

The energy transported by each carrier here is $(E - E_f)$. For the case $F = F_0$, the system remains in the equilibrium and no flow occurs. Thus,

F is replaced by $(F - F_0)$ in the equation. Since the drift velocity of the charge carriers is a small part of the total velocity [Gol09], υ is replaced by $\frac{2E}{3m^*}$, leading to

$$i = \mp\frac{2e}{3m^*}\int_0^\infty G(E)\tau_{e/h}E\frac{dF_0(E)}{dE}(\frac{dE_f}{dx} + \frac{(E-E_f)}{T}\frac{dT}{dx})dE. \tag{7.3}$$

with the effective mass m^*. Analogue, this can be done for the heat flux density:

$$j = \pm\int_0^\infty \upsilon(E-E_f)F(E)G(E)dE \tag{7.4}$$

$$j = \pm\frac{E_f}{e(orh)}i + \frac{2}{3m^*}\int_0^\infty E^2\frac{dF_0(E)}{dE}(\frac{dE_f}{dx} + \frac{(E-E_f)}{T}\frac{dT}{dx})dE. \tag{7.5}$$

The boundary conditions are inserted in order to find the transport parameters: σ is determined by the ratio $\frac{i}{electricfield}$, when no temperature gradient is applied ($\frac{dT}{dx} = 0$). Analogue, $\kappa_e = \frac{j}{\frac{-dT}{dx}}$, if the electric current is zero. The Seebeck coefficient is given by $\frac{electricfield}{\frac{dT}{dx}}$, if the electrical current is zero. [Gol09] Thus, the parameters can be determined (for electrons as major charge carriers) by:

$$\sigma = \frac{1}{\rho} = -\frac{2e^2}{3m^*}\int_0^\infty G(E)\tau_e\frac{dF_0(E)}{DE}dE \tag{7.6}$$

$$\kappa_e = \frac{2}{3m^*T}((\frac{(\int_0^\infty G(E)\tau_e E^2\frac{dF_0(E)}{DE}dE)^2}{\int_0^\infty G(E)\tau_e\frac{dF_0(E)}{dE}dE}) - \int_0^\infty G(E)\tau_e E^3\frac{dF_0(E)}{dE}dE) \tag{7.7}$$

$$S = \pm\frac{1}{eT}\frac{E_f - \int_0^\infty G(E)\tau_e E^2\frac{dF_0(E)}{dE}dE}{\int_0^\infty G(E)\tau_e E\frac{dF_0(E)}{dE}dE} \tag{7.8}$$

In order to simplify the equations above, the integrals can be substituted by coefficients of the order:

$$L_s = -\frac{2T}{3m^*}\int_0^\infty G(E)\tau_e E^{s+1}\frac{dF_0(E)}{dE}dE$$

By using eq. 5.1, G(E) and τ_e can be eliminated in the way of [Gol86]:

$$L_s = \frac{8\pi}{3}(\frac{2}{h^2})^{\frac{3}{2}}(m^*)^{\frac{1}{2}}T\tau_0(s + r + \frac{3}{2})(kT)^{s+r+\frac{3}{2}}F_{s+r+\frac{1}{2}},$$

with the Fermi-Dirac integrals $F_n(\chi) = \int_0^\infty \chi^n F_0(\chi) d\chi$, where$\chi$ is the reduced energy, that substitutes $\frac{E}{k_b T}$. The transport coefficients then can be expressed as:

$$\sigma = \frac{e^2}{T} L_1 \tag{7.9}$$

$$\kappa_e = \frac{1}{T^2}(L_2 - \frac{L_1^2}{L_0}) \tag{7.10}$$

$$S = \pm\frac{1}{eT}(E_f - \frac{L_1}{L_0}) \tag{7.11}$$

These are the required equations in order to understand the dependence of the main parameters contributing to the thermoelectric figure of merit ZT.
Due to an increase of the free energy $k_b T$ with increasing temperature, more charge carriers will be excited to energy states within the conduction band (electrons) and can contribute to the electrical conductivity. Thus, the electrical conductivity increases with increasing charge carrier concentration n/p and temperature T as illustrated in fig. 7.1. For the same matter, the electronic part of the thermal conductivity increases. In addition, the phonons also contribute to the thermal conductivity ($\kappa = \kappa_{phonon} + \kappa_e$). The Seebeck coefficient decreases with increasing n and T, thus the potential difference between the hot and cold ends of the semiconductor decreases.

Subsequently, the dependencies given in the eq. 7.9 - 7.11 are used in order to understand the behavior of the electrochemically deposited thermoelectric materials.
The measurement data of Bi_2Te_3, presented in fig. 7.2 exhibits an increasing electrical conductivity with increasing T. This is as expected for semiconductors, since σ scales linear with the increasing charge carrier density and - mobility by $\sigma = ne\mu$.
Since the behavior of the thermoelectric parameters changes for different temperature due to irreversible annealing effects, such as recrystallisation, crystal growth etc, the measurement will be discussed for two different temperature-ranges:

300-550 K During heating of the Bi_2Te_3 sample, it exhibits a slight increase of both Seebeck coefficient and electrical conductivity. As discussed above, the behavior of σ is consistent with the theory for semiconductors. However, since the Seebeck coefficient also increases, this causes S to be dominated by the temperature T, which can be best described

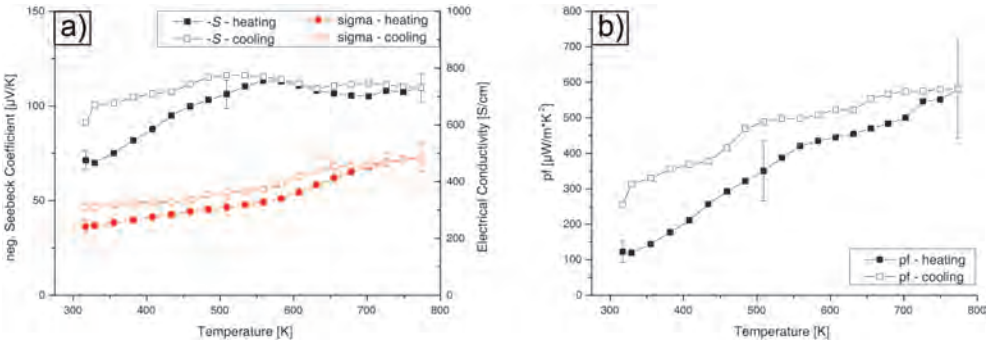

Figure 7.2: Thermoelectric performance of a $Bi_{1.976}Te_{3.024}$ film pulsed deposited (10/50 ms) in dependence on the temperature, (a) Seebeck coefficient and electrical conductivity, (b) power factor

with the Mott equation valid for higly doped semiconductors, that can be found by expanding eq. 7.11 with Sommerfeld [AM76]:

$$S = \frac{\pi^2 k_b^2 T}{3e}\left(\frac{1}{\sigma}\frac{d\sigma}{dE}\right)_{E_f} \tag{7.12}$$

$$S = \frac{\pi^2 k_b^2 T}{3e}\left(\frac{dln(\sigma)}{dE}\right)_{E_f} \tag{7.13}$$

from eq. 7.12 and the ohmic law, it can be found, that the Seebeck coefficient is related to the charge carrier density and mobility by: [Zas10]

$$S = \frac{\pi^2 k_b^2 T}{3e}\left(\frac{1}{\mu}\frac{d\mu(E)}{dE} + \frac{1}{n}\frac{dn(E)}{dE}\right)_{E_f} \tag{7.14}$$

In consequence, the power factor increases up to a temperature of around 550 K.

$\geq$ 550 K At temperatures higher than 550 K, irreversible annealing takes place: σ still increases, while the Seebeck coefficient decreases. Thus, the derivation of the power factor pf decreases (fig. 7.2), but remains at positive values, since σ still compensates the decrease of the Seebeck coefficient. This is consistent to the theory discussed for intrinsic semiconductors. Additionally, σ is observed to increase faster than at T$\leq$ 450 K. This is most likely due to annealing effects, which cause structural improvements by decreasing the amount of defects. The charge carrier mobility increases due to less crystal imperfectness. In addition, the charge carrier density increases by more electrons moved to the conduction band.

After the thermal treatment of the Bi_2Te_3 material, both the Seebeck coefficient and the electrical conductivity remain at higher values for almost the whole temperature range - also they do after returning to room temperature, the values remain at around 125 % for both S and σ. The overall improvements caused by the annealing process will be discussed in more detail in chapt. 7.2.3.

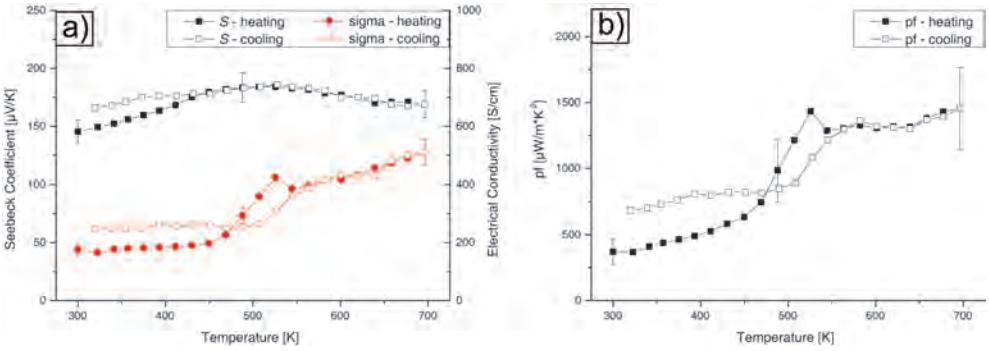

Figure 7.3: Thermoelectric performance of $Sb_{1.945}Te_{3.0525}$ films pulsed deposited (10/50 ms) in dependence on the temperature, (a) Seebeck coefficient and electrical conductivity, (b) power factor

In fig. 7.3, the results of p-doped Sb_2Te_3 are presented. Both the Seebeck coefficient and the electrical conductivity exhibit significantly higher values of about 250 % of S compared to the value of Bi_2Te_3. Although the thermoelectric performance is higher, the behavior of the parameters is comparable to those of Bi_2Te_3: the Seebeck coefficient increases up to a temperature of about 550 K and the electrical conductivity increases with increasing temperature. Above 550 K, the derivation of σ remains positive, but the increase of σ is lower compared to 450 K $\leq T \leq$ 550 K. This most likely is caused by increased scattering processes, causing a significant decrease of the charge carrier mobility μ.
In consistence, the power factor presented in fig. 7.3 (b) shows significantly improved values of around 300 % of the value for Bi_2Te_3. It exhibits a local maximum at around 550 K, which in general is consistent to the theory discussed in fig. 7.1. Due to a high increase of σ, the power factor remains at high values around 1300-1500 $\frac{\mu W}{K^2 m}$.

In order to further improve the - already significantly - thermoelectric performance of Sb_2Te_3, further doping is performed by adding acceptor atoms (Bi), leading to highly doped ternary p-doped $(Bi_xSb_{1-x})_2Te_3$, whose results are presented in fig. 7.4.

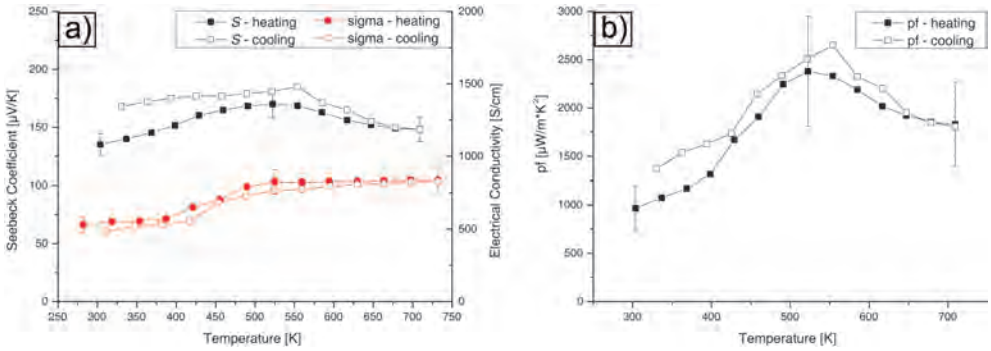

Figure 7.4: Thermoelectric performance of $(Bi_xSb_{1-x})_2Te_3$ films pulsed deposited (10/50 ms) in dependence on the temperature, (a) Seebeck coefficient and electrical conductivity, (b) power factor

Concurrent to the behavior of binary p-doped Sb_2Te_3, σ significantly increases with increasing T below 550 K, for higher T, the increase is lower due to increased phonon-electron scattering, leading to high decrease of the charge carrier mobility μ. The Seebeck coefficient also shows a similar behavior - it increases up to $T = 550$ K, with falling values for temperatures above. Thus, the power factor of $(Bi_xSb_{1-x})_2Te_3$, presented in fig. 7.4 (b), also shows an increase up to 550 K. For higher T, it decreases due to a predominant decrease of S and a moderate increase of σ. This is consistent with the theory for highly doped semiconductors.

In contrast to Sb_2Te_3, here σ exhibits a decrease due to annealing. After returning to room temperature, the electrical conductivity is decreased by about 15 % compared to the initial value. This is consistent to the theory and will be discussed in more detail in chapt. 7.2.3.

7.2 Annealing experiments

The results presented above in chapt. 6 prove the electrochemical deposition process to be sufficiently accurate in order to repeatably realize thermoelectric materials of high quality. Nevertheless, the relevant parameters such as the electrical conductivity, the charge carrier mobility and -density are highly sensitive to small changes in the composition of the materials [Bou10], accordingly, also the thermoelectric performance is (compare e.g. fig. 5.15). Electrodeposition in general exhibits a relative facile control over the composition [MDB$^+$05] and the materials deposited exhibit performance deficits (e.g. excess of the charge carrier density) compared to those deposited from the gaseous phase such as ALD or MBE-deposited materials. [TBP$^+$03]
Thermal post-treatment has been proven to reduce the density of crystal defects [JLO06], thus, the electrical properties may exhibits significantly improvements after the annealing process [LSZ$^+$08].

7.2.1 Annealing in He atmosphere with in-situ XRD

In order to avoid oxidation of the material, the thermal treatment is performed under He atmosphere in a home made heating chamber. [RSM$^+$11] For the purpose of in-situ XRD measurements, the chamber is mounted to a Bruker D8 Discover system presented in fig. 4.6. All measurements have been performed at the University of Ghent, Belgium (Christophe Detavernier/Geert Rampelberg).
In fig. 7.5, a scheme of the setup is illustrated, exhibiting the sample to be mounted to a heating plate and electrically contacted by probe tips at the edges of the samples' surface (fig. 7.6 (a)).

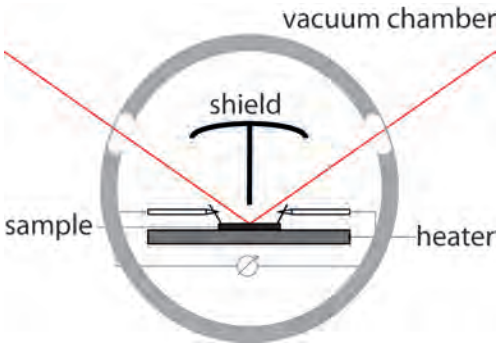

Figure 7.5: Scheme of the in-situ annealing with XRD measurement

The vacuum chamber features two notches sealed with capton foil in order to enable the X-Ray beam to penetrate the samples' surface. A

metal shield ensures no scattered X-Ray intensity to reach the detector (fig. 7.6 (b)).

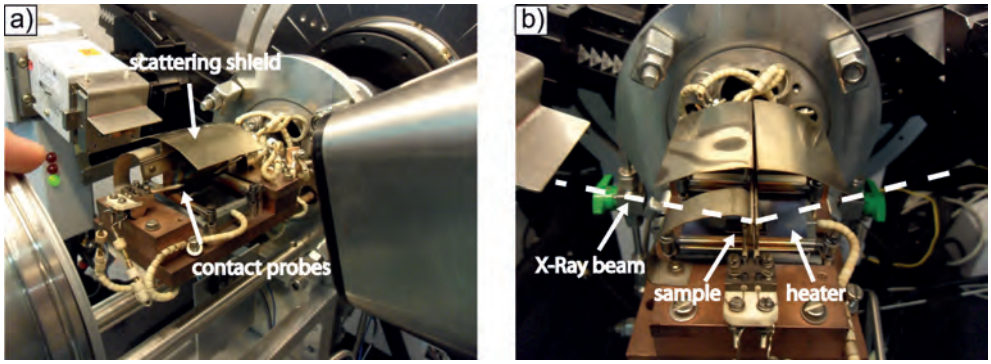

Figure 7.6: Experimental heating chamber mounted to a Bruker D8 Discover System; perspective of the sample mount without vacuum chamber

The samples are heated from room temperature up to 600 K with 0.2 $\frac{\mathrm{K}}{\mathrm{s}}$. Due to a constant He flow, the sample is tempered constantly and the correct heat can be measured, since a delay in the sample's temperature is avoided. In fig. 7.7, the XRD pattern of DC- and pulsed deposited Sb_2Te_3 are presented with respect to the annealing temperature. For both films, a decreased crystal imperfectness is observed, since the sharpened peaks indicate a more pronounced crystal orientation of the material in (015) and (110) direction.
In addition, the peaks indicating the orientation exhibit a crystal growth above an annealing temperature of about 450-500 K by significantly increased intensities of (1010) and (110) orientation. This is consistent to the observations discussed above - for temperatures above 500 K, again crystal growth starts, leading to a decrease of the amount of defects and larger grain sizes. Thus, the charge carriers mobility negative derivation with increasing T is lower.

The results presented indicate the quality of pulsed deposited (10/50 ms) Sb_2Te_3 to be significantly higher compared to DC deposited films, this is consistent to the results in terms of morphology observed during the synthesis (compare chapt. 3). Thus, the measurements are performed for pulsed deposited materials from now on. In fig. 7.8 and 7.9 the results of annealing in He atmosphere for ternary p-doped $(Bi_xSb_{1-x})_2Te_3$ and n-doped $Bi_2(Te_xSe_{1-x})_3$ are presented.
'The patterns of $(Bi_xSb_{1-x})_2Te_3$ corresponding to (015) and (110) show a distinctive crystal orientation along these directions (fig. 7.8 (a)). During the annealing process, improvements for these orientations as well as

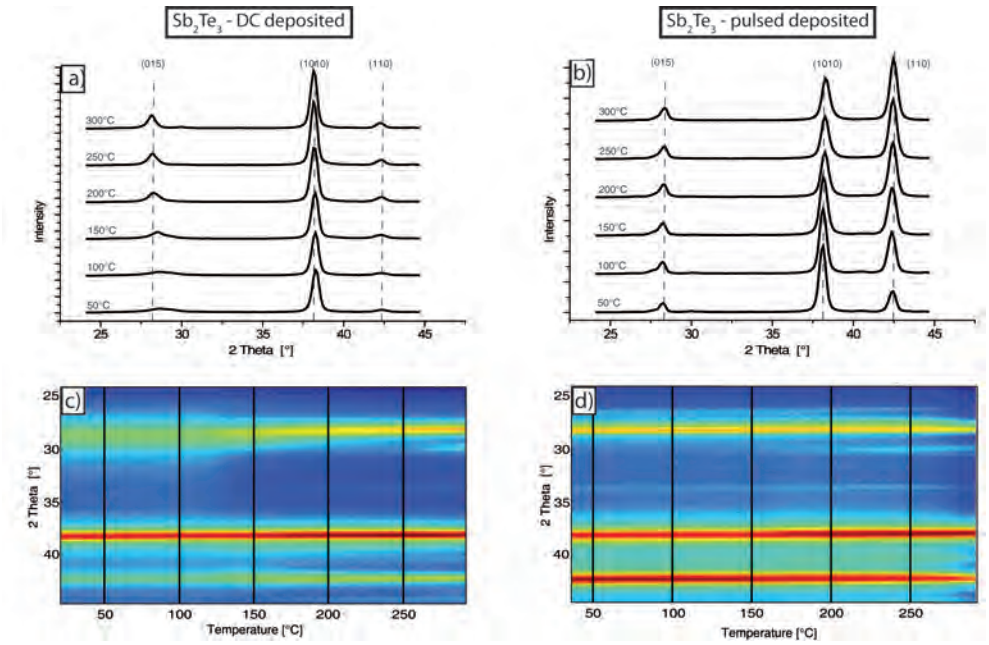

Figure 7.7: Diffraction pattern during annealing up to 600 K with 0.2 K/s, (a) for Sb_2Te_3 film DC deposited, (b) for Sb_2Te_3 films pulsed deposited (10/50 ms); in-situ XRD intensity in function of the annealing temperature, (c) for a Sb_2Te_3 film DC deposited, (d) for Sb_2Te_3 films pulsed deposited (10/50 ms)

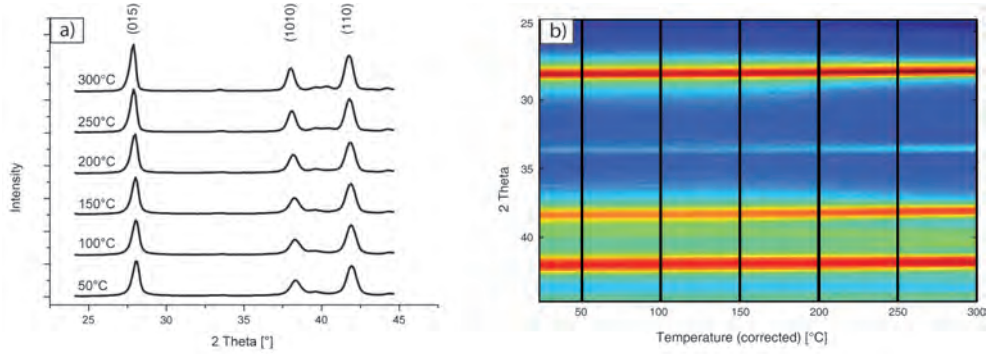

Figure 7.8: Measurement results for a $(Bi_{0.384}Sb_{0.515})_2Te_{3.203}$ film pulsed deposited (10/50 ms) during annealing up to 600 K with 0.2 K/s, (a) XRD patterns, (b) in-situ XRD intensity in function of the annealing temperature

for (1010) direction are observed.
The in situ XRD measurement of $Bi_2(Te_xSe_{1-x})_3$ is performed in a slightly

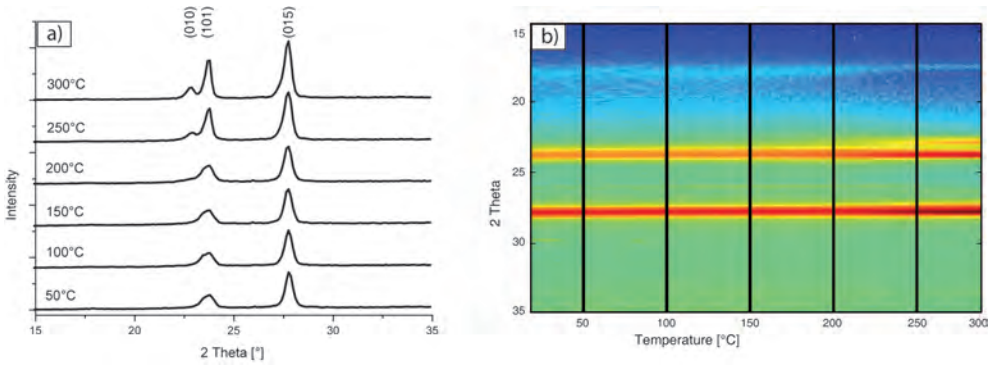

Figure 7.9: Measurement results for a $Bi_{1.960}(Te_{0.903}Se_{0.110})_3$ film pulsed deposited (10/50 ms) during annealing up to 600 K with 0.2 K/s, (a) XRD patterns, (b) in-situ XRD intensity in function of the annealing temperature

different geometry, in order to record the interesting range of 15° to 35°. Since pre-annealing XRD measurements indicate distinctive peaks at 23° and 24°, these are chosen to be analyzed in more detail. During annealing, both the clearly observable orientations of as deposited films, (012) and (015) become more distinctive, while a new peak at 23,5°, indicative of (010) orientation becomes observable after annealing.'[SRA+12] The electrical conductivity improves as presented consecutively in fig. 7.14.

7.2.2 Annealing in Te atmosphere

The annealing process in He atmosphere leads to significant improvements of the electric parameters as well as of the morphology and crystal structure of the thermoelectric materials. Due to the fact, that the thermoelectric performance is linked to the materials' composition [KOK07], annealing under equilibrium conditions may lead to significant improvements of the crystal structure and the composition in parallel. [BS54],[Bre69]

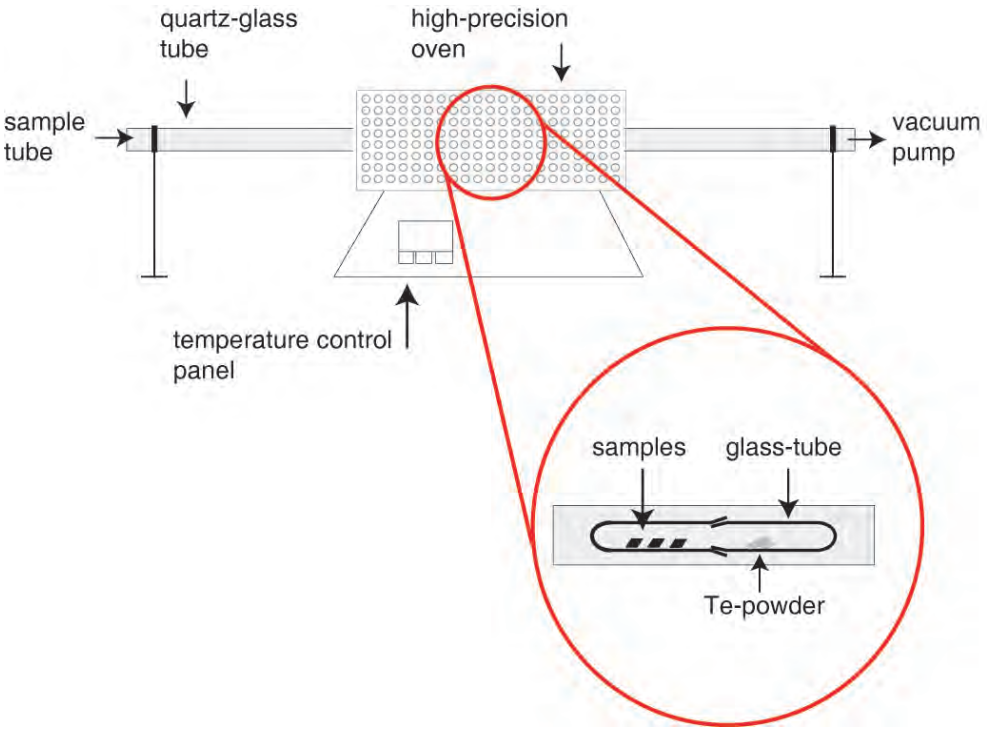

Figure 7.10: Setup for equilibrium annealing; high precision furnace with temperature-control; glass tube evacuated to P $\approx$ 3 x 10^{-4} mbar; inlay: sealed glass-tube with samples and Te

In fig. 7.10, the setup for the equilibrium annealing of the thermoelectric materials is illustrated. The small sample tube is evacuated inside the large quartz-glass tube to a pressure of about 3 x 10^{-4} mbar. Then, the small tube is closed and the system is heated up to the annealing temperature. Thus, the elemental Te in the sealed tube starts to evaporate until an equilibrium atmosphere is set up inside the sealed tube. The vapor pressure of Te in function of the temperature can be found in fig. A.3.

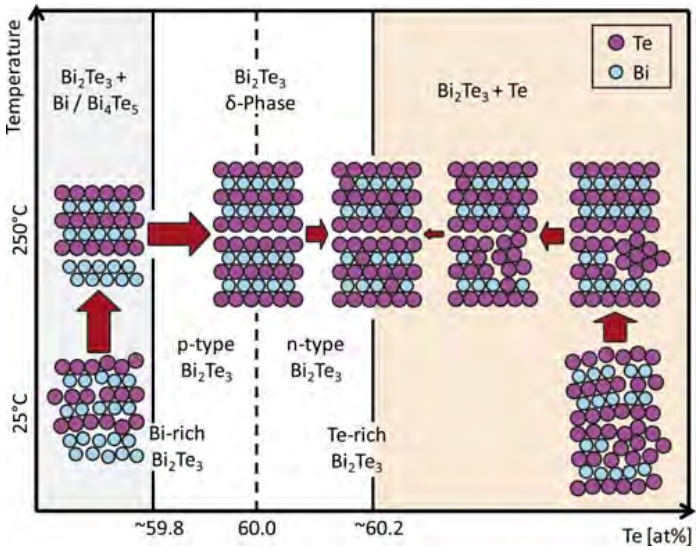

Figure 7.11: Reactions during the annealing process in Te atmosphere [RSW11].

For Bi_2Te_3, the method has been used leading to reduced charge carrier densities and significantly improved Seebeck coefficients of the electrodeposited thermoelectric material. [RSW11]. The materials' composition improves, causing lower electrical conductivities and higher Seebeck coefficients. Due to the square dependence of S to the power factor pf, the thermoelectric performance was improved due to the thermal treatment.

Here, both the binary and the ternary chalcogenide materials have been annealed under a Te equilibrium atmosphere at 525 K for 100 h. In fig. 7.11, the phase diagram is illustrated schematically for Bi_2Te_3. Materials exhibiting a Te deficit are observed to form stoichiometric Bi_2Te_3 phases by reaction of Bi_2 layers with the gaseous Te. Materials showing a Te excess are formed from stoichiometric Bi_2Te_3 phases and elemental Te. Due to the high vapor pressure of Te at this temperature, the elemental Te from the material evaporates until the equilibrium to the gaseous Te atmosphere is reached. Since the concentration-gradient scales linearly with the Te excess, the process' reaction velocity becomes very low, the higher the improvement of the stoichiometry gets. The equilibrium annealing process can be found in more detail in ref. [RSW11].
Although here ternary compounds are annealed, one can expect significant improvements as well, since the high aspiration of Te to evaporate from the material may be compensated during the treatment in Te equilibrium atmosphere. Sb_2Te_3 is expected to behave almost similar to Bi_3Te_3, since the crystal structure is similar with just Sb located at

the Bi lattice sites, but since the ternary compounds strongly exhibited higher material quality in terms of morphology and also thermoelectric performance, the annealing process is focused on the optimization of well performing ternary compounds only.

In order to compare the results of both annealing methods, different pieces of the same samples are used for annealing in He and Te atmosphere.

7.2.3 Improvements after annealing

The improvements of the thermoelectric films during annealing are presented in the figures 7.12 to 7.18. The changes in the charge carrier density and - mobility are presented in fig. 7.12 and 7.13, contributing to the electrical conductivity of the deposited materials, which is presented in fig. 7.14. The changes observed are summarized here:

$(Bi_xSb_{1-x})_2Te_3$

- as deposited:
  - n-doped material shows higher electrical conductivity compared to the p-doped material
  - the Seebeck coefficient of p-doped material is higher compared to that of n-doped material
  - the power factor of p-doped material is higher compared to that of n-doped material
- annealing in He ambience:
  - the electrical conductivity exhibits improvements of about 10 %
  - the Seebeck coefficient increases with improved stoichiometry by around 10-20 %
  - the power factor improves by up to +60 %
- annealing in Te ambience:
  - the electrical conductivity exhibits decreases of about -25 %
  - the Seebeck coefficient increases with improved stoichiometry by around +50-100 %
  - the power factor improves by up to +80 %

$Bi_2(Te_xSe_{1-x})_3$

- annealing in He ambience:
  - the electrical conductivity exhibits slight decreases of about -5 %
  - the Seebeck coefficient increases with improved stoichiometry by around +10 %
  - the power factor improves by up to +50 %
- annealing in Te ambience:
  - the electrical conductivity exhibits decreases of about -35 %
  - the Seebeck coefficient increases with improved stoichiometry by around +50-80 %
  - the power factor improves by up to +100 %

Subsequently, the changes in the thermoelectric performance are analyzed by having a more detailed look onto the transport parameters such as charge carrier density, -mobility, Seebeck coefficient and also the chemical composition of the materials.
After returning to the initial room temperature, the resistivity of the deposited material abates to around 90 % of the initial value for $(Bi_xSb_{1-x})_2Te_3$, thus the improvement of the electrical conductivity due to annealing

in He atmosphere is of about +10 % (compare to fig. 7.14 (a)). 'Although the improvements for p-doped $(Bi_xSb_{1-x})_2Te_3$ are consistent with previously results with - also p-doped - Sb2Te3 [SRA+12], for n-doped $Bi_2(Te_xSe_{1-x})_3$ films, a different behavior is observed: after returning to RT, the resistivity remains at around 110 % of the initial value, results in a slightly decrease of around -10 % in electrical conductivity (compare fig. 7.14 (b)).

During the annealing in He atmosphere, the decrease in carrier density of the n-doped $Bi_2(Te_xSe_{1-x})_3$ films is higher compared to p-doped $(Bi_xSb_{1-x})_2Te_3$ films. Furthermore, as deposited n-doped films already exhibit higher carrier densities. This suggests larger deviations from stoichiometry. During annealing, these materials are likely to either combine to stoichiometric phases or evaporate (e.g. Se and Te are likely to evaporate during annealing, reducing the carrier concentration significantly - compare fig. 7.12). In addition, at temperatures above 450-500 K, an intensive crystal growth is observed during the annealing process leading to larger crystal sizes compared to as deposited films (compare tab. 7.1). This strongly decreases the amount of defects in the annealed materials, leading to higher charge carrier mobilities (presented in fig. 7.13). Also the higher initial crystallinity of p-doped as deposited films, observed in the XRD patterns as discussed above causes a 30-50 % lower decrease of the carrier density during annealing compared to the n-doped films.

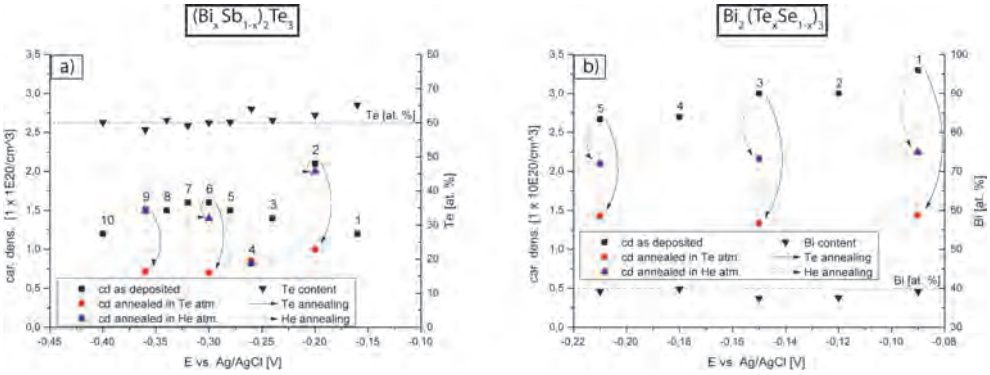

Figure 7.12: Charge carrier density of as-deposited and annealed samples in function of deposition potential for pulsed deposited (10/50 ms) films, (a) $(Bi_xSb_{1-x})_2Te_3$, (b) $Bi_2(Te_xSe_{1-x})_3$

In table 7.1, the structural improvements to the films are presented, indicating larger crystal sizes of p-doped materials already in the as deposited state. This is consistent with the discussion above. The Seebeck values of the films annealed in He atmosphere strongly increase for both ma-

terials (compare fig. 7.17, 7.18). Furthermore, a slight change in the composition is observable as a decrease of Te for $(Bi_xSb_{1-x})_2Te_3$ and an increase of Bi for $Bi_2(Te_xSe_{1-x})_3$, respectively. This is most likely due to the evaporation of Te and Se during the annealing process, but the materials remain sufficiently stoichiometric due to short annealing times.

		$\mathbf{(Bi_xSb_{1-x})_2Te_3}$ #2	$\mathbf{Bi_2(Te_xSe_{1-x})_3}$ #5
literature	a $[\mathring{A}]$	4.2842	4.3740
	c $[\mathring{A}]$	30.5239	30.4242
as deposited	a $[\mathring{A}]$	4.2999	4.3735
	c $[\mathring{A}]$	30.4262	30.6239
	avg. cr. size $[nm]$	326	274
annealead in	a $[\mathring{A}]$	4.3002	4.3702
He atmosphere	c $[\mathring{A}]$	30.4972	30.6896
	avg. cr. size $[nm]$	463	336
annealead in	a $[\mathring{A}]$	4.3074	4.3661
Te atmosphere	c $[\mathring{A}]$	30.5210	30.6931
	avg. cr. size $[nm]$	482	351

Table 7.1: Structural parameters (measured) of selected pulsed deposited (10/50 ms) . literature values [STOa],[STOb]

Significant improvements are achieved and a small decrease of Te-content is observable. This may be due to the short annealing time of about 0.5 - 1 h.
Further annealing could additionally improve the composition of the films. As presented in [RSW11], it is possible to change the films' composition by postdeposition annealing under Te atmosphere to tune into almost perfect stoichiometry. Here the treatment of n-doped Bi_2Te_3 films is presented. The results will also be transferable for $(Bi_xSb_{1-x})_2Te_3$ and $Bi_2(Te_xSe_{1-x})_3$ by annealing in Te atmosphere, since the main indicator of good thermoelectric performance is reported to be the (Bi,Sb):Te ratio of 2:3.[SS59] Due to the strong tendency of tellurium to evaporate from the materials during thermal treatment, this also may be of interest for n-doped $Bi_2(Te_xSe_{1-x})_3$.

In the figures 7.17, 7.18, the Seebeck coefficients of the samples annealed in Te atmosphere are compared to the Seebeck values of samples in as deposited state as well as after annealing in He atmosphere for ≤ 1 h. For

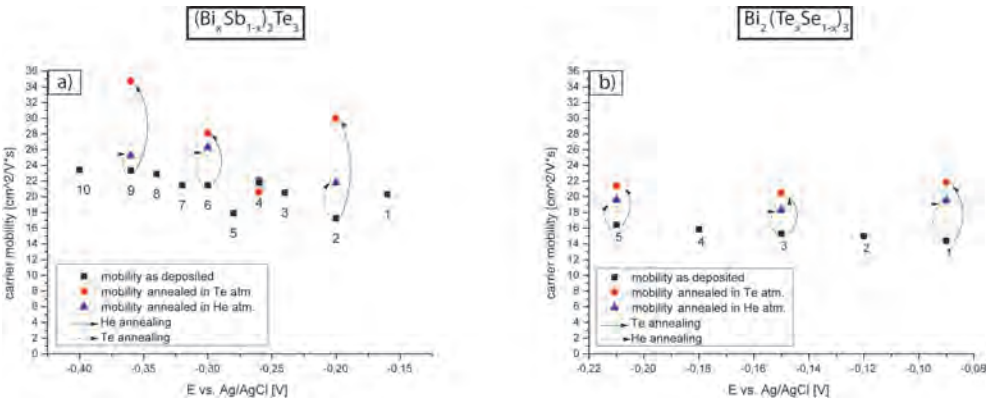

Figure 7.13: Charge carrier mobility of as-deposited and annealed samples in function of deposition potential for pulsed deposited (10/50 ms) films, (a) $(Bi_xSb_{1-x})_2Te_3$, (b) $Bi_2(Te_xSe_{1-x})_3$

both materials, the Seebeck values strongly increase during annealing in Te atmosphere to values of about $+200\ \frac{\mu V}{K}$ and $-130\ \frac{\mu V}{K}$, respectively.

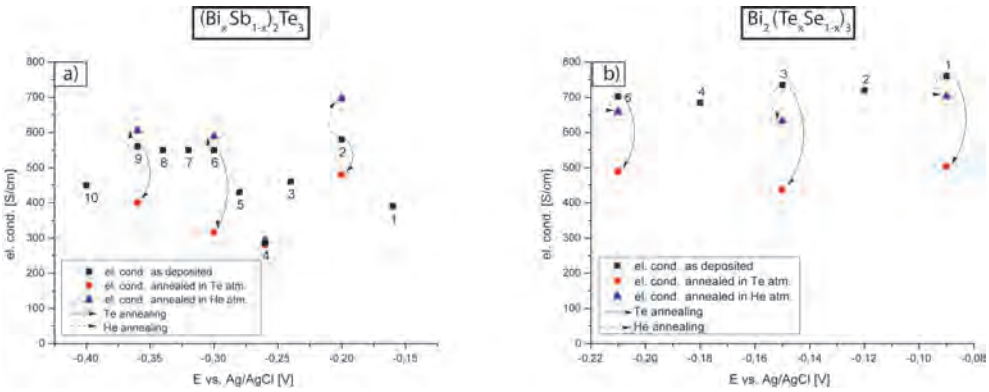

Figure 7.14: Electrical conductivity of as-deposited and annealed samples in function of deposition potential for pulsed deposited (10/50 ms) films, (a) $(Bi_xSb_{1-x})_2Te_3$, (b) $Bi_2(Te_xSe_{1-x})_3$

For $(Bi_xSb_{1-x})_2Te_3$, the composition of the films changes strongly towards ideal stoichiometry. Samples with almost ideal composition in the as deposited state show a slight increase of the Te content but stay within $\pm$ 0.25 at. % of 60 at. % Te. Samples with high Te deficit ($\approx$58 at. %) show a strong increase of Te content to almost the ideal composition. The excess of Bi in the material reacts with the gaseous Te to form Bi_2Te_3, therefore the Te content increases. Samples with a high Te excess ($\approx$62 at. %) exhibit a high decrease in Te content to also almost ideal com-

position. The excess of Te evaporates from the sample, although at a slower rate than in He atmosphere.

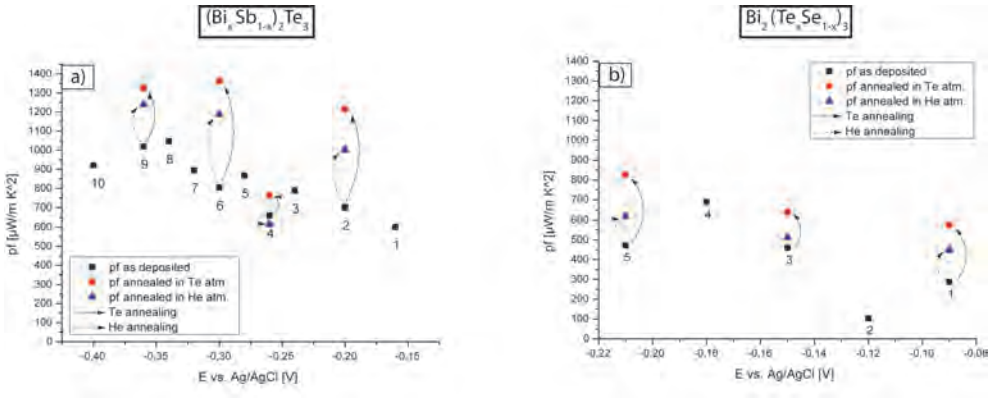

Figure 7.15: Power factor of as-deposited and annealed samples in function of deposition potential for pulsed deposited (10/50 ms) films, (a) $(Bi_xSb_{1-x})_2Te_3$, (b) $Bi_2(Te_xSe_{1-x})_3$

Samples with an initially high Te excess are improved as well, albeit not to perfection. In general, all samples should reach a steady Te content after a sufficient annealing duration. For $Bi_2(Te_xSe_{1-x})_3$, the film composition also shows improvements. All annealed samples are Te/Se rich in as deposited state. During the annealing process, the samples' composition changes to a lower excess of Te/Se due to the Te atmosphere. Since the Se is likely to evaporate from the films during annealing, the compositions tend to do not reach completely the ideal composition in terms of Se. Further improvements could be achieved by annealing under combined Te/Se atmosphere. [NBKB11]
Figure 7.16 provides more detailed information about the transport parameters. The materials' charge carrier density significantly decreases during annealing. For $(Bi_xSb_{1-x})_2Te_3$, S steadily increases with decreasing density. For $Bi_2(Te_xSe_{1-x})_3$, S also decreases with decreasing n, although the annealing of the films may change the materials' composition and especially the Te/Se ratio, causing slightly different behavior. During the thermal treatment in Te atmosphere, the carrier density further decreases for both materials compared to the samples in as deposited state and after annealing in He atmosphere. This is most likely due to further defect annealing during the annealing process, as well as the formation of stoichiometric phases due to the equilibrium atmosphere. Correspondingly, there is a strong decrease in the electrical conductivity during the annealing processes, although the carrier mobility of both materials increases with respect to $\sigma = ne\mu$ and $\sigma = pe\mu$, respectively.

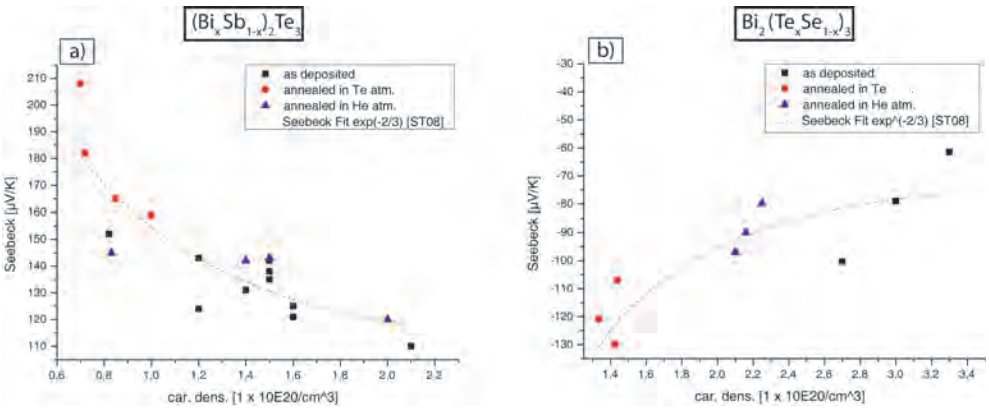

Figure 7.16: Seebeck coefficients of as-deposited and annealed samples in function of charge carrier density for pulsed deposited (10/50 ms) films, (a) $(Bi_xSb_{1-x})_2Te_3$, (b) $Bi_2(Te_xSe_{1-x})_3$

For both materials, a decrease of up to around -45 % is observed (compare fig. 7.12). Despite this decrease in the electrical conductivity, all samples annealed in Te atmosphere exhibit a strong improvement of the power factors (compare fig. 7.15), increases of about +70 % and +80 % are observed causing maximum values of 1325 $\frac{\mu W}{K^2 m}$ and 825 $\frac{\mu W}{K^2 m}$, respectively.'[SRA+12]. Thus, annealing in Te equilibrium ambience emerged to be a suitable and effective method for thermal posttreatment, since both the stoichiometry and the thermoelectric performance of Bi_2Te_3-based semiconductor compounds exhibit significant improvements. Due to the high vapor pressure of Se, a process combining both Te and Se equilibrium atmosphere could be optimal. [NBKB11]

For the ternary compound $(Bi_xSb_{1-x})_2Te_3$, one can expect the ratio of Bi/Sb to change, since Sb is more likely to evaporate, due to it's higher vapor pressure at lower annealing temperature compared to Bi (compare fig. A.3). For $Bi_2(Te_xSe_{1-x})_3$, the ratio Te-Se may change, since the vapor pressure of Se is much lower and therefore Se is even more likely to evaporate from the material than Te, since the Te annealing equilibrium process requires sufficiently high temperatures for the evaporation of Te.

The results shown in figures 7.17 and 7.18 indicate, that, although a not ideal composition in the as deposited state can be fixed, the highest performance is obtained with starting composition around $\pm$ 0.5 % from ideal stoichiometry. Thus, the materials' composition should be be carefully controlled during the deposition process, although the films exhibit slight improvements during the thermal treatment.

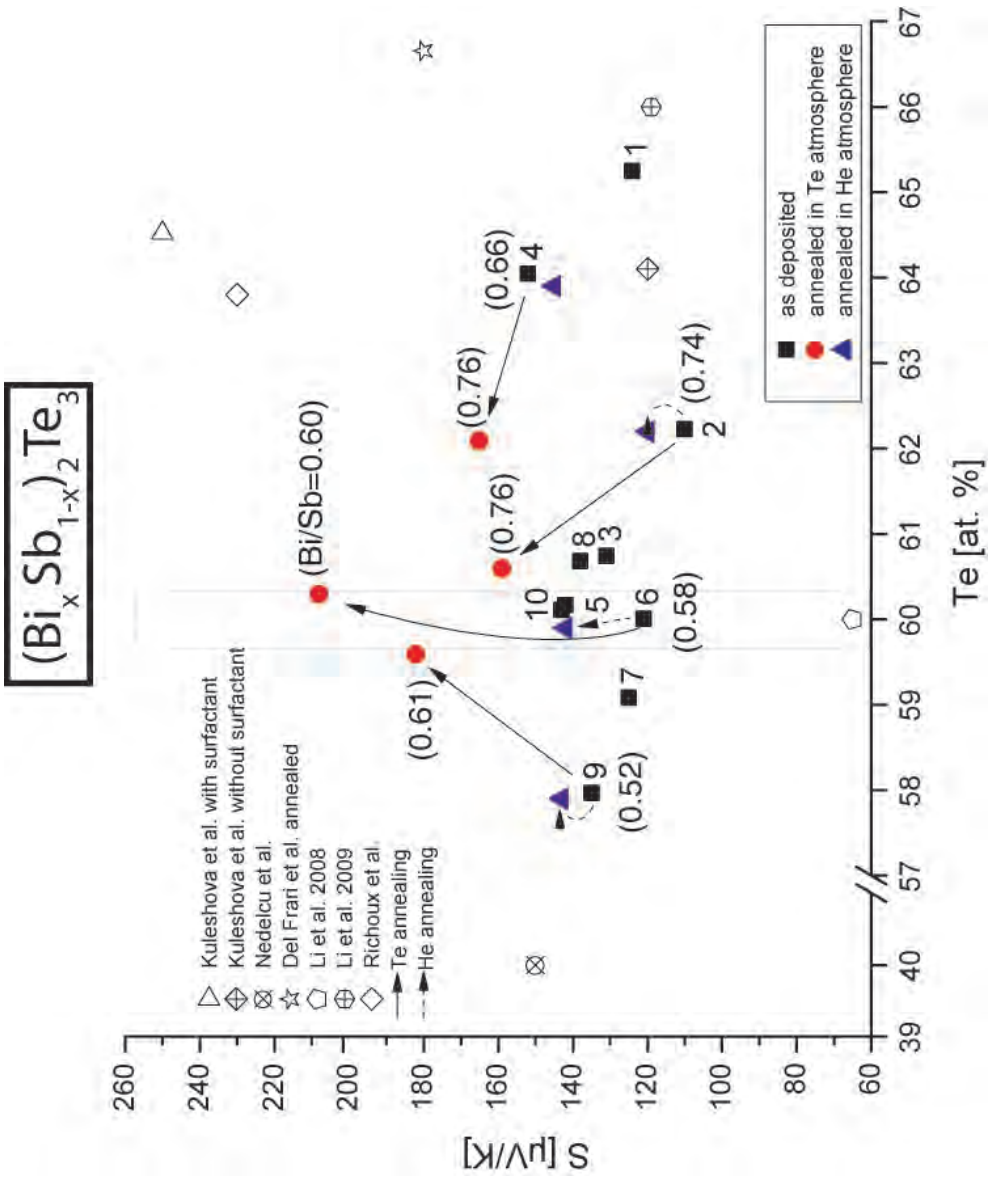

Figure 7.17: Seebeck coefficients of as-deposited and annealed samples in function of the materials' composition for pulsed deposited (10/50 ms) $(Bi_xSb_{1-x})_2Te_3$ films

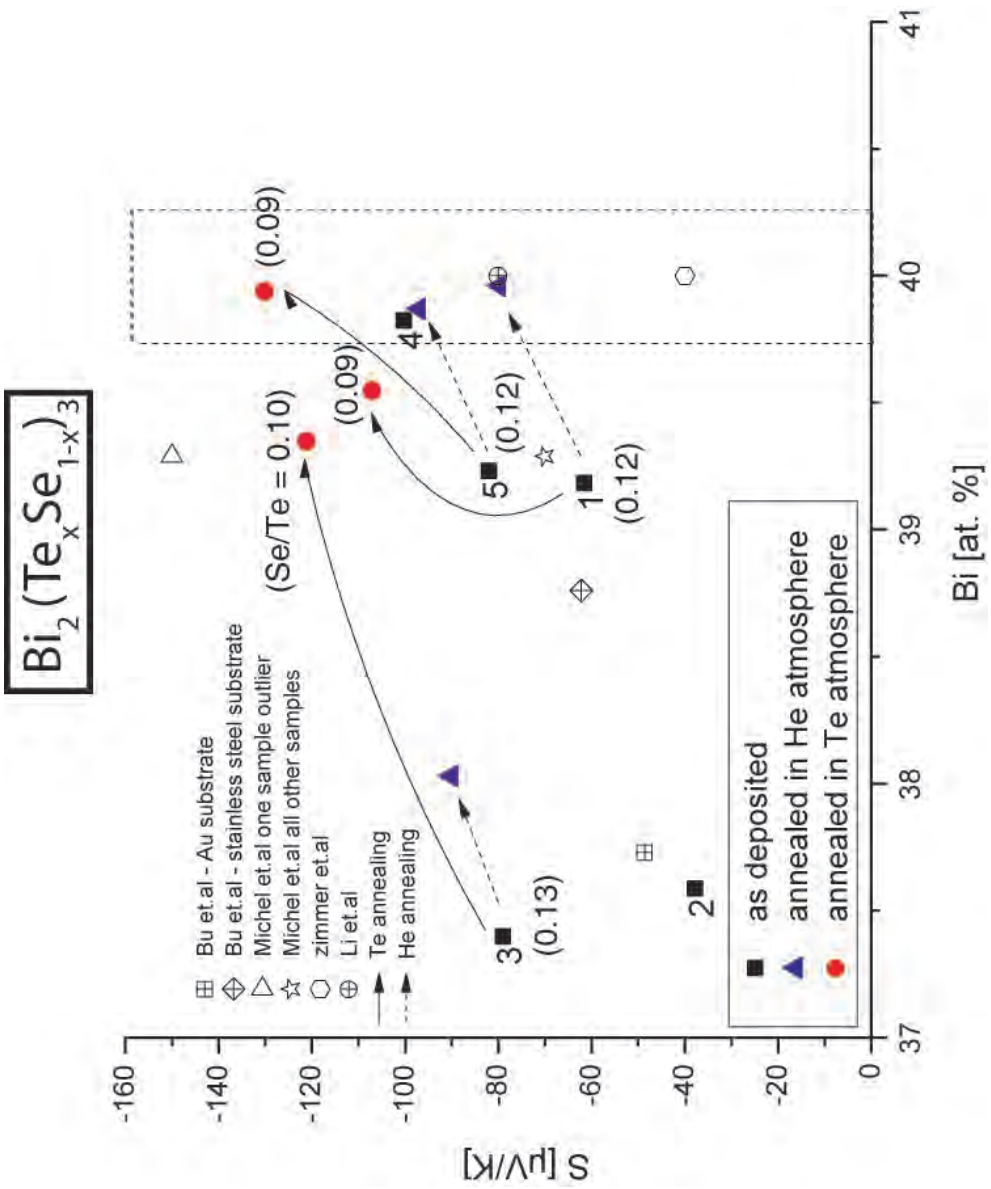

Figure 7.18: Seebeck coefficients of as-deposited and annealed samples in function of the materials' composition for pulsed deposited (10/50 ms) $Bi_2(Te_xSe_{1-x})_3$ films

In table 7.2, the results of selected samples are presented. As discussed in chapt. 5 and 6, the thermoelectric figure of merit of p-doped films is higher than that of n-doped films. This also is observed after the thermal treatment of the films in He and Te ambience. The electrical conductivity of n-doped films is higher, so the charge carrier density also is about 70 % higher (compare fig. 7.12). Due to eq. 7.14, the thermopower is reciprocally proportional to the charge carrier concentration and thus, the absolute value of the Seebeck coefficient of p-doped films is higher compared to those of n-doped films (figs. 7.17, 7.18).

The thermal conductivity at 300 K exhibits higher values for as deposited than for annealed materials and lower values for p-doped films compared to the n-doped films. This is most likely due to decreasing crystal imperfectness during annealing and lower electrical conductivities of p-doped compared to those of n-doped materials.

		$Bi_2(Te_xSe_{1-x})_3$ (#5) puls-dep. (10/50 ms)		
		as deposited	aft. He ann.	aft. Te ann.
dep. pot.	[V vs. ref]	-210		
compos.	[at. %]	39.2/54.1/6.7	39.9/53.9/6.2	39.9/55.3/4.8
σ	[Scm^{-1}]	702	659	488
S	[μVK^{-1}]	-82	-97	-130
pf	[$\mu WK^{-2}m^{-1}$]	472	620	825
κ (RT)	[$WK^{-1}m^{-1}$]	1.2	1.2	1.0
ZT (RT)		0.12	0.16	0.25
		$(Bi_xSb_{1-x})_2Te_3$ (#9) puls-dep. (10/50 ms)		
		as deposited	aft. He ann.	aft. Te ann.
dep. pot.	[V vs. ref]	-360		
compos.	[at. %]	14.4/27.6/58.0	14.6/27.5/57.9	15.3/25.1/59.6
σ	[Scm^{-1}]	560	606	400
S	[μVK^{-1}]	135	143	182
pf	[$\mu WK^{-2}m^{-1}$]	1020	1239	1325
κ (RT)	[$WK^{-1}m^{-1}$]	1.1	1.3	1.0
ZT (RT)		0.28	0.29	0.40

Table 7.2: Thermoelectric performance of $Bi_2(Te_xSe_{1-x})_3$ and $(Bi_xSb_{1-x})_2Te_3$ films pulsed deposited (10/50 ms) as deposited and after annealing in He and Te ambience

The electrodeposited films exhibit higher performances than most other reported thermoelectric materials. For p-doped materials, the perfor-

mance of the as deposited materials is already equal or up to +50 % higher than best reported electrodeposited [KKL+10], [NSM+02], [LW09] materials. The annealed $Bi_2(Te_xSe_{1-x})_3$ films exhibit +20 % higher values compared to best reported annealed films [DFDS+06]. Best performing samples exhibit thermopowers of up to 212 $\frac{\mu V}{K}$ (compare fig. 7.17). This is actually comparable to bulk values, since about 90 % of the value of nanograined bulk materials are achieved [XTY+09] [NBKB11].

The n-doped $Bi_2(Te_xSe_{1-x})_3$ films exhibit about +20-50 % higher values compared to best reported electrodeposited films. [BWW07] [BWW08] [ZSTB07] [LSZ+08] After annealing, the films exhibit up to 320 % higher values compared to almost all reported materials. Michel et al. reported about the electrodeposition of an n-doped film, which exhibited very high thermopower of about -150 $\frac{\mu V}{K}$, what is actually 15 % higher compared to the films reported in this work [MDS+08], but the sample reported about was one out of a bunch, with all other samples' quality reported to be significantly lower.
Samples annealed in equilibrium Te atmosphere exhibit values of about 50-70 % of nanograined bulk performances [YPM+10], what is actually less than the performances, the p-doped materials exhibit. This is most likely due to the fact, that the annealing in Te atmosphere improves the composition in terms of Te, but not in terms of Se, since there is no Se equilibrium atmosphere during annealing. Further annealing in combined Te/Se atmosphere is likely to achieve further significantly improvements of these materials.

Now, that the materials' fabrication processes are achieved and the quality of the deposited thermoelectric materials is proven, in general the materials are ready for application use, e.g. the integration into microdevice-thermogenerators. In order to obtain more detailed information about the transport properties, in particular the cross-plane transport parameters, nanostructured materials are used subsequently. The nanowires will allow for the characterization of thermoelectric performance and transport parameter in small dimensions, thus more informations on the influence of the crystal structure can be achieved in chapt. 8.

Chapter 8

Nanostructuring - Nanowires

As discussed in chapt. 7, the fabrication of the developed material in nanoscale dimensions is an eligible instrument for the analysis of the physical properties of the thermoelectric materials in more detail. Due to the small dimension in the range of about 50-100 nanometers, effects such as increased scattering processes may occur, leading to an improved thermoelectric performance.

The thermoelectric figure of merit

$$ZT = \frac{S^2\sigma}{\kappa}T$$

points out the need for a high electrical conductivity on the one hand and a small thermal conductivity on the other hand in order to optimize the ZT value. As already discussed in chapt. 2, both values are directly linked to each other by the Wiedemann-Franz law (compare eq. 2.8). Shrinking the size of the fabricated structure in general leads to an increased amount of surfaces, at which (boundary) scattering processes of charge carriers may occur. Thus, the increased scattering processes may decrease the thermal conductivity and so improve the thermoelectric figure of merit.
In addition, the predominant crystal orientation may be changed due to a different, more aligned growth process inside the pores of the AAO membranes. As already discussed, a decrease of crystal imperfectness may significantly improve the thermoelectric performance (compare to the in-situ XRD analysis in chapt. 7).

Due to the well defined geometry of a single nanowire, high precise electric and thermoelectric characterization of the material can be achieved in contrast to measurements of ensembles of nanowires or macroscopic films. Thus, single nanowire measurements are performed and will be discussed subsequently in chapt. 8.2 and 8.4.

The electrochemical deposition of nanowires starts with the fabrication of alumina templates, into which the thermoelectric nanowires are deposited. The feasibility of such self ordered, hexagonally structured membranes is well reported in the literature. First works of Masuda et al. present a two-step anodisation process with the fabrication of porous alumina membranes with a pore diameter of 70 nm [MF95]. Today, many other related works report about the fabrication and optimization of highly ordered Al_2O_3 alumina membrane structures with different pore diameters (20-300 nm), e.g. about the use of pre-textured alumina templates to form the ordering of the membranes [ANN+01]. However, most of the work was done for the self-organized structuring process for hexagonal porous alumina membranes [MHO97] [JMG98], for two dimensional systems [LMB+99] or for modulated pore diameters [LMB+98] [LSS+08].

8.1 AAO Membranes

The fabrication process can be described as presented in fig. 8.1 and is directly related to the works by Yuan et al. [YHSX04] and Nielsch et al. [NCS+02].

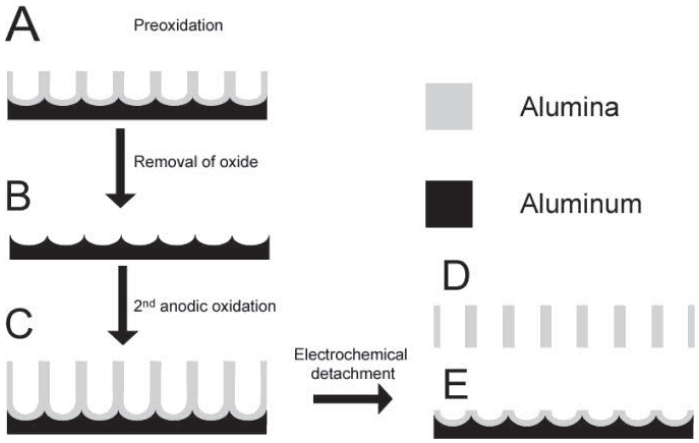

Figure 8.1: Illustration of the fabrication process of AAO membranes for the nanowire deposition; (A), a first, non ordered, hole-structure is etched, (B) the redundant AAO is removed, (D) another layer of pores, perfectly ordered is etched, (D) removal of redundant AAO [YHSX04]

The process starts with the electrochemical oxidation of the Aluminum, which leads to not yet perfectly ordered pores in the AAO. After removing the aluminum oxide, a second anodisation is performed with forming highly self-ordered holes in the AAO layer. The pores may be widened

by chemical etching in phosphoric acid to the desired diameter. After detaching the barrier layer from the oxide, an AAO membrane is isolated with both ends opened. The back side of the membrane then is covered by first sputtered Au and afterwards, an electrochemically deposited, thick Au layer as electrode.

This Au layer then is connected to a potentiostat and thus used as the working electrode for the electrochemical deposition of thermoelectric material into the pores of the AAO membrane. Thus, the electrodeposited nanowires have predetermined diameter (pore diameter of the AAO membrane) and length (thickness of the membrane). In fig. 8.2, a SEM image of a loaded AAO membrane is presented.

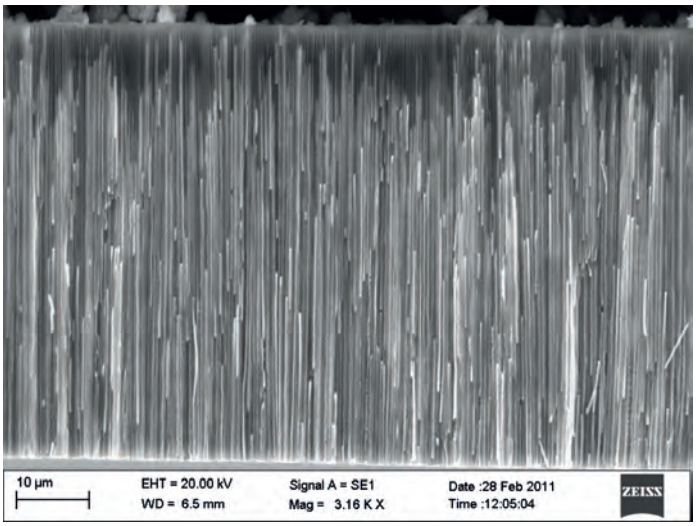

Figure 8.2: Cross-section SEM image of the AAO membrane after electrochemical filling with $Bi_2(Te_xSe_{1-x})_3$ nanowires with l=40 μm, diam=200 nm each

The nanowires embedded in the pores of the membrane are observable, indicated by the white stripes in fig. 8.2. Most of the nanowires fill almost 90-98 % of the total length (40 μm) of the pores. The diameter of the nanowires is determined by SEM to be 200 nm. After dissolving the AAO membrane in concentrated NaOH solution or chromic acid, the wires are cleaned by pipetting and replacing the solution with either distilled water or isopropanol. The nanowires solved in the solution then can be processed for multiple purposes.

TEM (Transmission Electron Microscopy) images of a selected Bi_2Te_3 nanowire are presented in fig. 8.3. The overview image (a) exhibits a uniform geometry and structure with sharp edges over the length of

the nanowire. The diffraction image presented in (b) exhibits the high degree of crystallinity of the nanowire, since the common reflections are observable and only slight circular diffractions are observable.

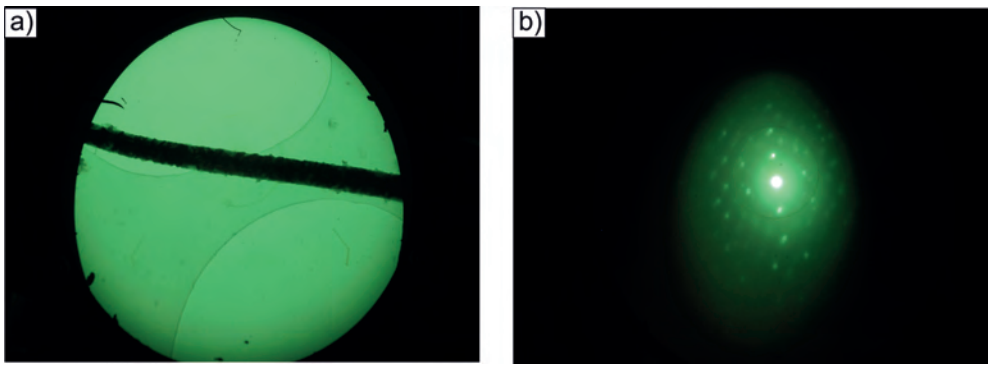

Figure 8.3: TEM picture of a Bi_2Te_3 nanowire with l=40 μm, diam=200 nm; (a) overview, (b) reflection view

In fig. 8.4 and 8.5, the TEM images of ternary $Bi_2(Te_xSe_{1-x})_3$ are presented, indicating the structure of the ternary, Se-doped Bi_2Te_3 nanowires to be of even higher quality compared to binary Bi_2Te_3. The nanowire exhibits an almost perfect homogeneity, since the edges are uniform with very smooth surfaces. Although the deflection image shows some slight circular deflections, the material is observed to be single-crystalline. The single-crystallinity has been proven to be homogeneously distributed over the nanowires' surface. (compare additional HRTEM images in chapt. A. The composition of the nanowire has been proven to be almost ideal composition by TEM-EDX.
TEM images of the nanowires of ternary p-doped $(Bi_xSb_{1-x})_2Te_3$ are presented in fig 8.6 and 8.7. As observed from (a), the surface of the edges of the nanowires is not that smooth compared to those of the n-dopes nanowires presented above. Although the nanowire is observed to be uniform over it's whole length of 40 μm, the outer regions of the wire exhibit some areas of reduced material density and therefore, inhomogeneous diameter of the nanowire.

This phenomenon may be solved by the imperative addition of complexing agents for all types of electrolyte, that contain Sb. In order to solve the Sb, tartaric acid is added, building very large complexes (compare chapt. 3). Thus, the mobility of the ions in the solution may be significantly decreased, causing a very low diffusion of ions during the electrochemical deposition. Thus, the electrochemical deposition inside the pores does not start from the bottom growing uniformly in z-direction,

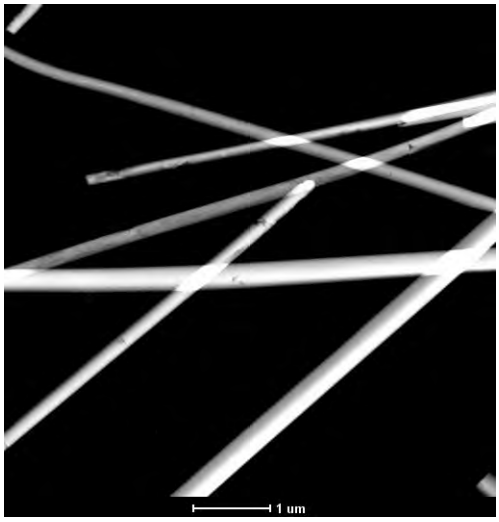

Figure 8.4: TEM overview image of a $Bi_2(Te_xSe_{1-x})_3$ nanowire with l=40 μm, diam=150 nm

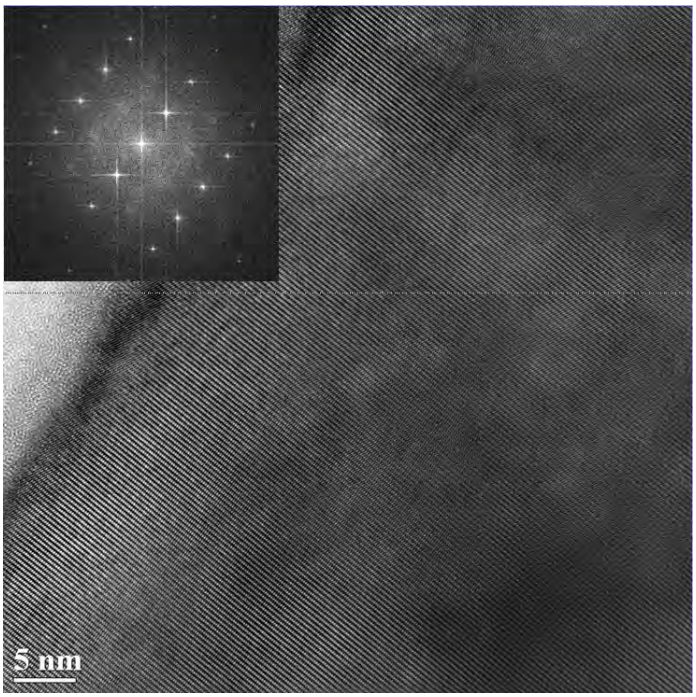

Figure 8.5: High resolution TEM image of a $Bi_2(Te_xSe_{1-x})_3$ nanowire with l=40 μm, diam=150 nm; inlay: reflection image

but it may take place, building empty enclaves, especially at the outer

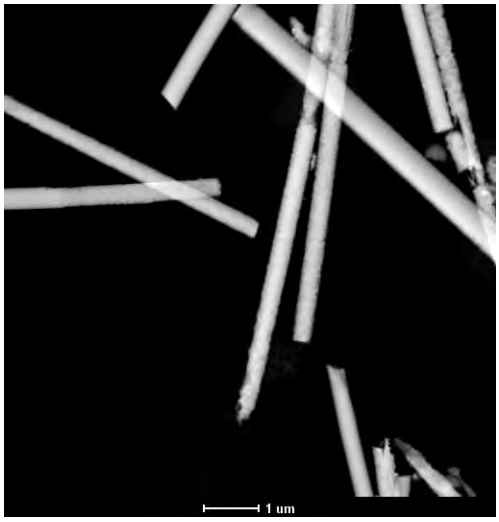

Figure 8.6: TEM overview image of a $(Bi_xSb_{1-x})_2Te_3$ nanowire with l=40 μm, diam=200 nm

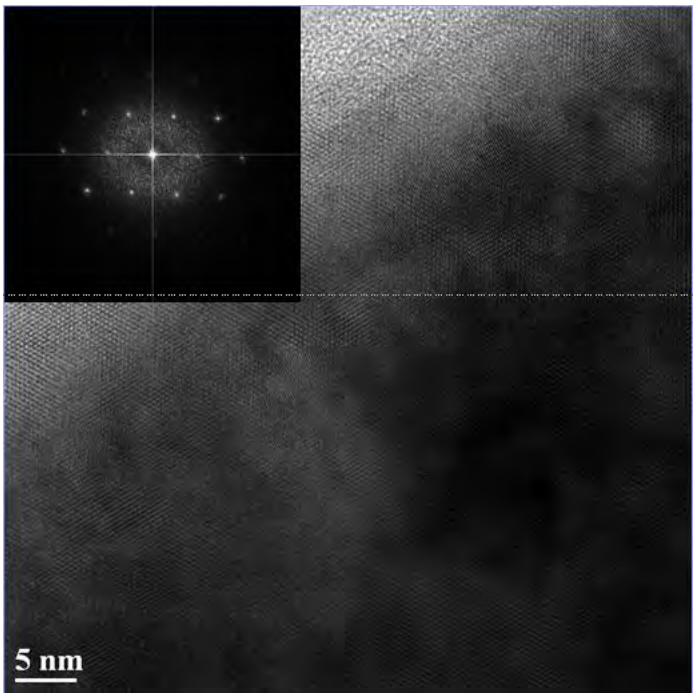

Figure 8.7: High resolution TEM image of a $(Bi_xSb_{1-x})_2Te_3$ nanowire with l=40 μm, diam=200 nm; inlay: reflection image

areas of the pores/nanowires. Thus, the scraggy areas at the edges of the

nanowires are observed here. This problem may be solved by lacing of additives or coating of the membranes' pores. However, this also is the reason for the challenging fabrication of binary Sb_2Te_3 nanowires, since the moderate positive influence of the Bi-doping atoms is missing there, causing an even larger size of complexes compared to those of ternary $(Bi_xSb_{1-x})_2Te_3$.

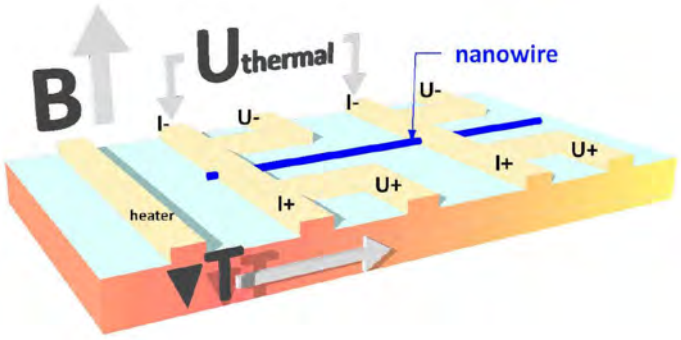

Figure 8.8: Illustration of the measurement setup for single nanowire measurement of the Seebeck coefficient and the electrical conductivity [BOEHNERT]

8.2 Measurement Setup for Single Nanowires

In order to perform the thermoelectric characterization of single nanowires fabricated with binary and ternary Bi_2Te_3 based materials, the Seebeck coefficient and the electrical conductivity are measured and the thermoelectric power factor is achieved by $pf = S^2\sigma$. As already discussed above, single nanowire measurements allow for the precise determination of thermoelectric performance, since the geometry analyzed is well defined. In contrast, the measurement of the transport parameters on films and nanowire ensembles lack this precision.

In fig. 8.9, the principle of the measurement setup is illustrated. This method has proven to work properly for various nanostructured materials by Tim Boehnert, University of Hamburg. A current of a few mA in the heater (contacts # 9 & 10) leads to $P \approx 0.3$ mW, thus a temperature gradient ΔT of about ≈ 5 K is realized trough the length of the contacted, distinct part of the nanowire.

In fig. 8.10, SEM images of the structure made by lithography onto a glass substrate is shown at different magnifications. The contacted nanowire is presented at a higher magnification in fig. 8.12.

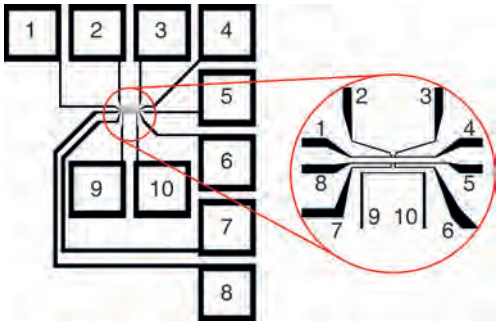

Figure 8.9: Illustrated contact setup used for single nanowire measurement

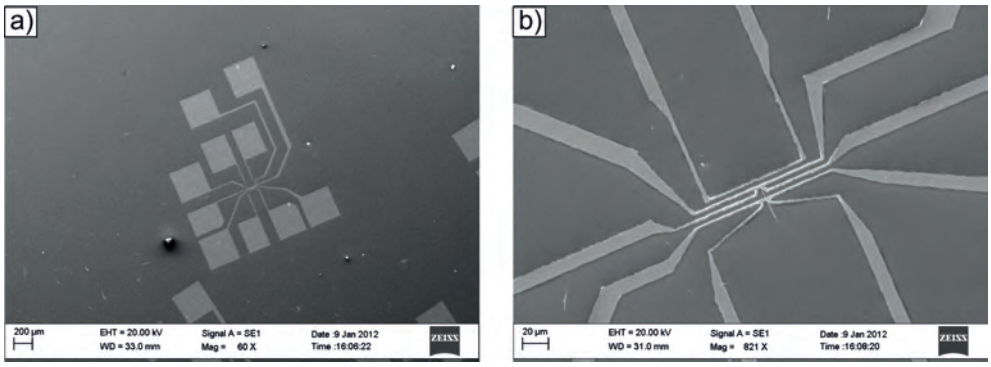

Figure 8.10: SEM pictures of the contacted $Bi_2(Te_xSe_{1-x})_3$ nanowire with l=40 μm, diam=200 nm

After realizing the temperature difference ΔT in the nanowire, the Voltage U_{thermal} is measured between the contacts # 1 & 8 (thermometers) along the contacted nanowire. Subsequently, an AC current of ≈ 10 μA flows between contacts # 1 & 4 and between # 8 & 5. In order to avoid interferences, different frequencies are used: $f_{14} \neq f_{85}$. The contacts # 2 & 3 and # 7 & 6 are used as voltage probes for the measurement of the resistivity of the well-defined part of each thermometer. Thus, the temperature of each nanowire end can be determined. Simulation results for the temperature gradient in function of the length along the main nanowire axis and along the thermometer are presented in fig. 8.11. Thus, only very small deviations of the temperature are expected at the contact points of the thermometers and in addition, a temperature gradient is expected along the nanowire, since the heater is located at one end of the mounted nanowire. This results have to be taken into account for the evaluation of the single nanowire measurement. The Seebeck

coefficient is achieved by

$$S = \frac{-U_{thermal}}{\Delta T} = \frac{-U_{thermal}}{T_{hot} - T_{cold}}$$

In addition, the electrical resistivity R_{nanowire} is measured along the nanowire. Thus, the electrical conductivity can be achieved by

$$\sigma = \frac{l_{nanowire}}{R_{nanowire} \cdot A_{nanowire}} \tag{8.1}$$

with A_{nanowire} and l_{nanowire} to be the cross-section area and lenght of the contacted part of the nanowire, which are determined to be 200 nm and 9 μm, respectively.

By using $pf = S^2\sigma$, then the thermoelectric power factor is calculated.

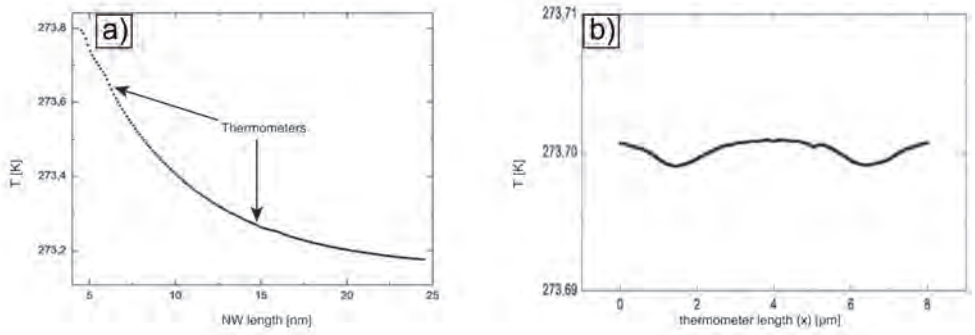

Figure 8.11: (a) simulation of the temperature along the main nanowire axis; (b) simulation of the temperature along the thermometer [BOEHNERT]

8.3 Seebeck Measurements

In fig. 8.13, the electrical conductivity of a single $Bi_2(Te_xSe_{1-x})_3$ nanowire is presented. The resistance of the nanowire is measured in dependence on the temperature T. The measurement starts at 50 K towards RT.
The resistance is measured between both ends of the nanowire contacted to the structure presented above. Since the length and the diameter of the nanowire is known, the electrical conductivity can be determined with respect to eq. 8.1.
With increasing temperature, the resistance of the nanowire slightly increases, which is characteristic for a metal-like behavior. For $T \geq 300$ K,

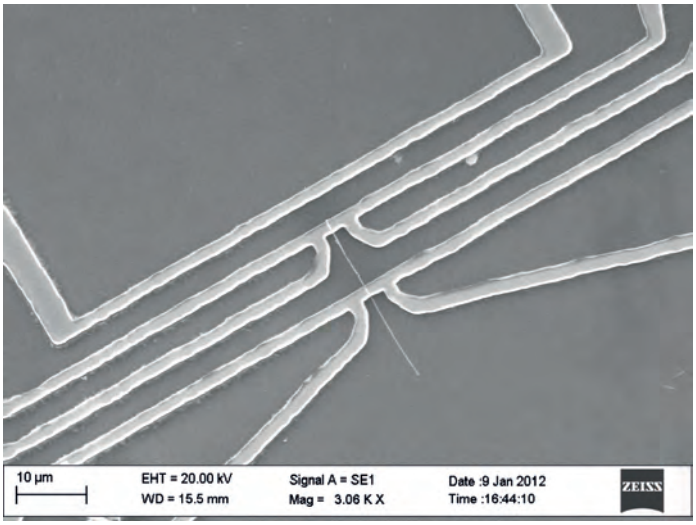

Figure 8.12: SEM picture of the contacted $Bi_2(Te_xSe_{1-x})_3$ nanowire with l=40 μm, diam=200 nm

irreversible structural changes in the crystal structure start to occur, similar to those observed with the annealing of thin films, which have been discussed in more detail in chapt. 7. However, the resistance starts to decrease with increasing annealing time and -temperature (black curve). This is most likely due to an improved crystal structure and a therefore increasing mobility of the charge carriers. In addition, the contacts may have changed due to diffusion of Pt through the barrier layer. Also the nanowires' geometry, e.g. diameter may have changed during the annealing process.
The resistance after annealing at RT finally appears to be reduced to almost 50 % the initial value before annealing. Further heating of the material now shows a repeatable electrical resistance. The metallic behavior is most likely due to the presence of low energy donator subbands, which cause an almost homogeneous charge carrier density with increasing temperature, leading to be the carrier mobility the dominant parameter to contribute to the electrical resistance.

The Seebeck coefficient of the $Bi_2(Te_xSe_{1-x})_3$ nanowire as function of the temperature is shown in fig. 8.14. S increases with increasing temperature. This is consistent with the behavior of the resistance discussed above. The initial Seebeck coefficient S of the as deposited nanowire is around $-30\ \frac{\mu V}{K}$ at 50 K. S increases up to a maximum value $\approx -110\ \frac{\mu V}{K}$ at 300 K, where the curve of S gets almost saturated.

After returning to room temperature, the Seebeck coefficient exhibits an

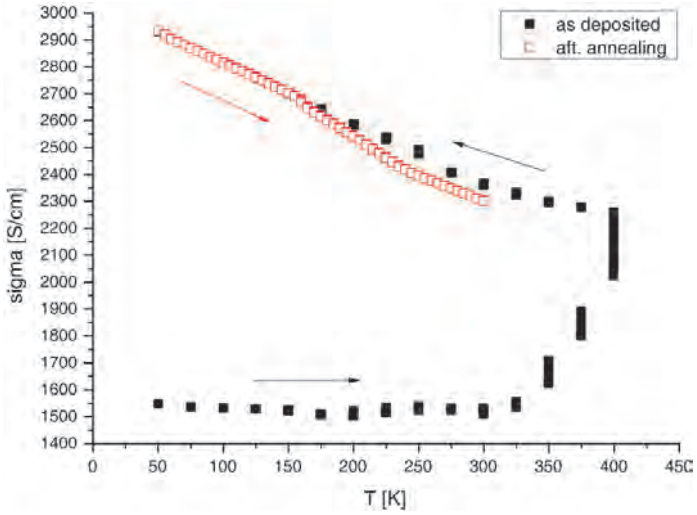

Figure 8.13: Electrical conductivity of a $Bi_2(Te_xSe_{1-x})_3$ (39.7 at.% Bi, 54 at.% Te, 6.3 at.% Se) nanowire with with l=40 μm, diam=200 nm pulsed deposited (10/50 ms) in function of the annealing temperature

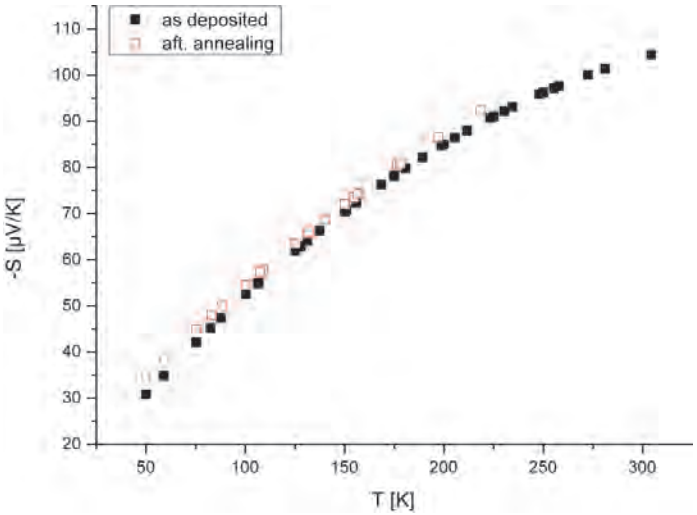

Figure 8.14: Seebeck coefficient of a $Bi_2(Te_xSe_{1-x})_3$ nanowire with l=40 μm, diam=200 nm pulsed deposited (10/50 ms) in function of the annealing temperature

improved value of around $-37\ \frac{\mu V}{K}$. It increases in parallel to the behavior of the as deposited wire, but keeps the improvement over the whole range of T. Thus, the structural improvements discussed above also indicate the influence to the Seebeck coefficient, most likely by significantly decreasing

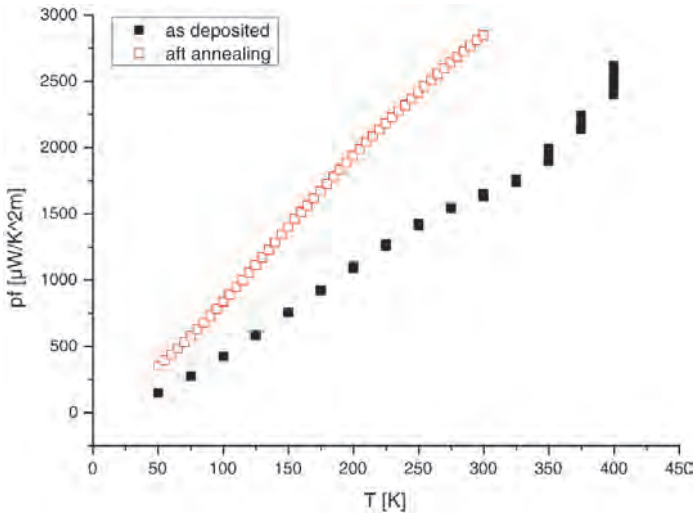

Figure 8.15: Power factor of a $Bi_2(Te_xSe_{1-x})_3$ nanowire with l=40 μm, diam=200 nm pulsed deposited (10/50 ms) in function of the annealing temperature

the charge carrier concentration due to crystal improvements. Thus, the power factor presented in fig. 8.15 exhibits an improvement with increasing temperature and also a strong irreversible improvement due to annealing effects.,

In fig. 8.16, the conductivity of a $(Bi_xSb_{1-x})_2Te_3$ nanowire is presented in function of the temperature. In contrast to $Bi_2(Te_xSe_{1-x})_3$, the resistance steadily increases. Thus, the electrical conductivity decreases with increasing temperature T.
After heating the material up to 400 K for 20 h, annealing effects similar to those discussed above are observed. Thus, the electrical resistance further increases at T=400 K (constant). This may most likely be due to the reduction of crystal defects and therefore decreased charge carrier density. After the annealing process, the electrical resistance remains higher compared to the as deposited state, but still scales linearly with the temperature.
In figure 8.17, the Seebeck coefficient is presented as function of the temperature. It exhibits a strong correlation to the temperature. As much as with the electrical resistance, it increases with increasing temperature. Also, the nanowire exhibits annealing effects, the Seebeck coefficient shows an increase of about +30 % after annealing. At temperatures above 350 K, S starts to saturate.
The power factor of the $(Bi_xSb_{1-x})_2Te_3$ nanowire is presented in function

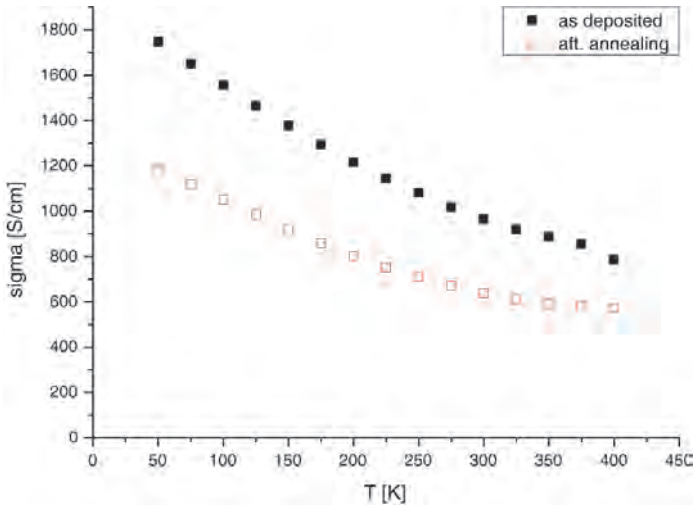

Figure 8.16: Electrical conductivity of a $(Bi_xSb_{1-x})_2Te_3$ nanowire with l=40 μm, diam=80 nm pulsed deposited (10/50 ms) in function of the annealing temperature

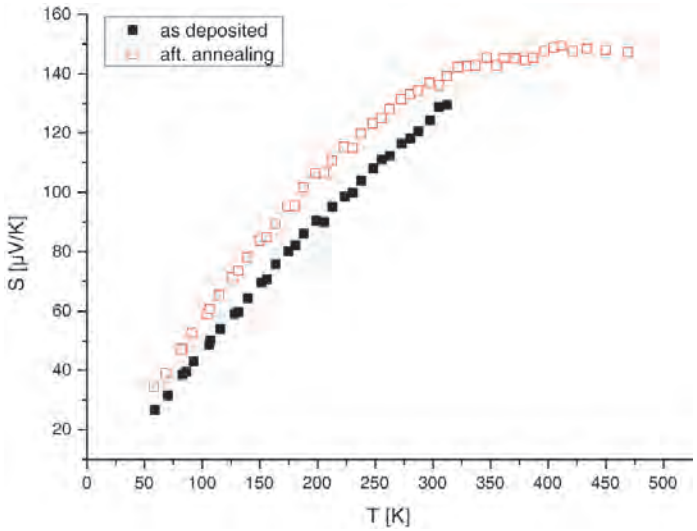

Figure 8.17: Seebeck coefficient of a $(Bi_xSb_{1-x})_2Te_3$ nanowire with l=40 μm, diam=80 nm pulsed deposited (10/50 ms) in function of the annealing temperature

of the temperature in fig. 8.18. It increases with increasing T. At temperatures above 350 K, the derivation of pf starts to decrease, dominated by the behavior of the Seebeck coefficient discussed above. Since the electrical resistance R (compare fig. 8.16) is very high compared to that of

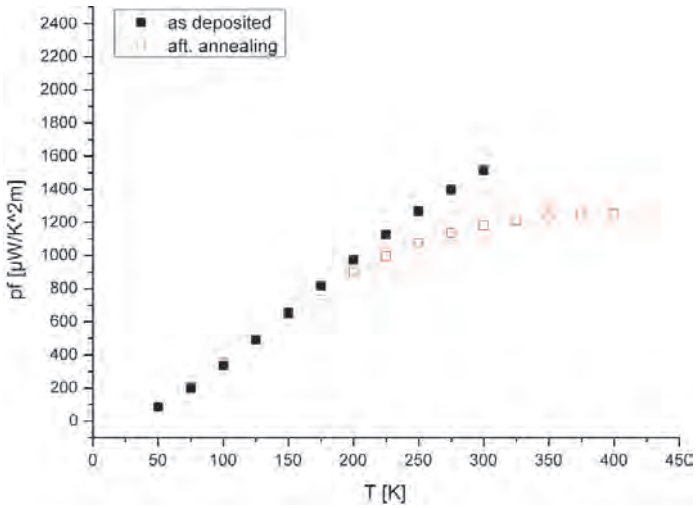

Figure 8.18: Power factor of a $(Bi_xSb_{1-x})_2Te_3$ nanowire with l=40 μm, diam=80 nm pulsed deposited (10/50 ms) in function of the annealing temperature

$Bi_2(Te_xSe_{1-x})_3$ (compare fig. 8.13), the power factor is low compared to that of $Bi_2(Te_xSe_{1-x})_3$. One reason for the high values of R may be the fact, that the surface of the edges of the $(Bi_xSb_{1-x})_2Te_3$ nanowire is rough compared to those of the $Bi_2(Te_xSe_{1-x})_3$ nanowire (compare chapt. 8.1). Thus, the effective diameter of the $Bi_xSb_{1-x})_2Te_3$ nanowire cannot be determined accurately. In order to ensure reliable results, the diameter used for the calculation of the power factor is set conservatively. It is also possible to assume much smaller diameter, which would improve the thermoelectric performance significantly.

8.4 Nanowire Field-Effect Transistor

In order to understand the nanowires' electrical properties presented above, they have to be analyzed in more detail. Since the electrical conductivity scales with the charge carrier density and mobility ($\sigma = ne\mu$), these values are of high interest.

Therefore, single nanowires are contacted similarly as discussed above (compare fig. 8.8) with the measurement setup for the determination of the Seebeck coefficient, but onto a highly conductive Si wafer with 200nm of thermal Si-oxide on top. This method has been intensely proven to work by [Goo11]. The "nanowire field-effect" transistor (NFET) is comparable to a metal-oxide semiconductor field effect transistor (MOSFET),

since the gate is separated from the drain and source of the transistor by an isolating layer of Si-oxide. Similarly to an ordinary transistor, the current through the nanowire is controlled by the voltage applied to the gate. In fig. 8.19, a scheme of the device is presented. Three different analysis models with different IV-curve behavior are applicable for MOSFET measurements - here, the device is analyzed using the "linear model" [Zeh11], where the semiconductor is assumed to behave like an ohmic resistor, that is modulated by a back gate. [Goo11]

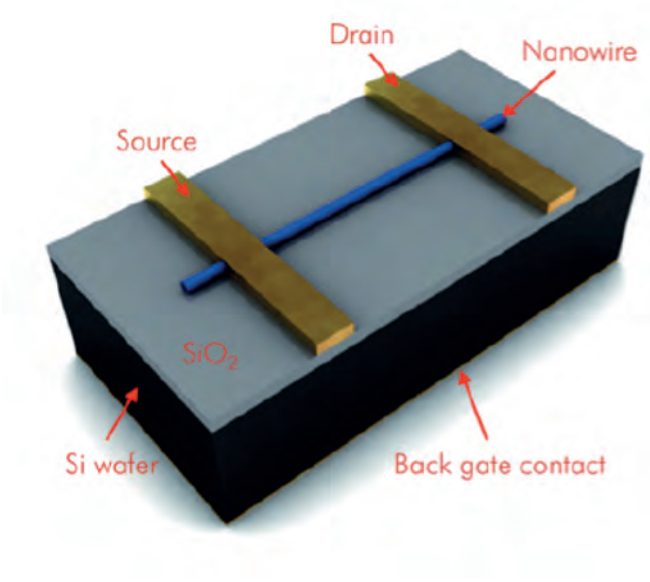

Figure 8.19: illustration of a field effective nanowire transistor with contacted nanowire of 200 nm diameter and a contact distance of 9 μm [Goo11]

The current through the nanowire I_{NW} is given by the current between the transistor's source and drain:

$$I_{NW} = I_{SD} = -\frac{Q}{t} \tag{8.2}$$

with the total charge Q and the time $t = -\frac{Length_{NW}}{\upsilon}$ (υ :velocity of charge carriers) for the charge carriers to move through the nanowire. Drude modeled the velocity of the charge carriers to be

$$\upsilon = \mu E = \mu \frac{V_{SD}}{L} \tag{8.3}$$

with the voltage V_{SD} along the nanowire of length L. Since the velocity υ is assumed to be constant, E can be replaced. Thus, eq. 8.2 can be

expressed as

$$I_{SD} = -\mu Q \frac{V_{SD}}{L^2} \tag{8.4}$$

gives the current through the nanowire. If one assumes the charge carrier density to be constant throughout the length of the contacted nanowire and $V_G - V_{thresh} \gg V_S D$, Q can be expressed by $Q = -C(V_G - V_{thresh})$ for $V_G \geq V_{thresh}$ and else Q=0. The threshold voltage V_{thresh} thereby is defined as the threshold of the gate voltage once the current through the nanowire starts. C is the capacitance of the nanowire, which has to be simulated using the setup geometry - the resulting capacity distribution is presented in fig. 8.20. The mobility then can be expresses as

$$\mu = \frac{I_{SD} L^2}{V_{SD} C (V_G - V_{thresh})} \tag{8.5}$$

Since the threshold value often cannot be determined accurately due to imperfectnesses of the measurement setup, the transconductance $g = \frac{dI}{dV_G}$ is used instead. Thus, the charge carrier mobility is given by

$$\mu = g \frac{L^2}{V_{SD} C} \tag{8.6}$$

which appears to be dependent on the major charge carriers (positive/negative) by the sign of the slope. Then, the charge carrier density (n/p) can be expressed by using

$$I_{SD} = \int qnV dA = qn\upsilon A \tag{8.7}$$

finally to:

$$n = \frac{I_{SD} L}{q\mu V_{SD} A} \tag{8.8}$$

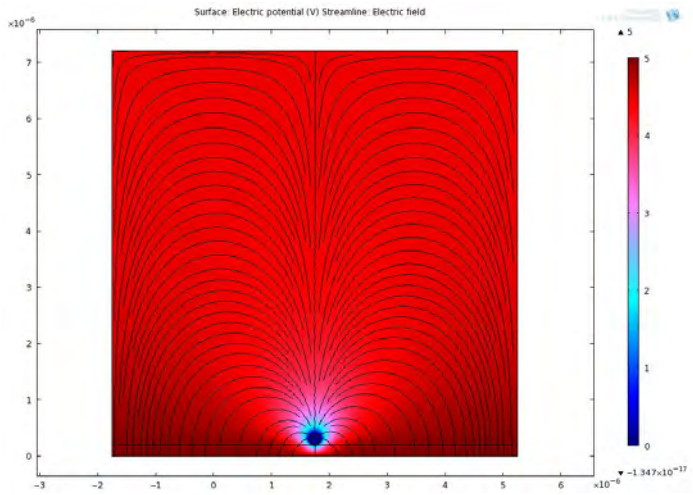

Figure 8.20: Capacitance throughout the 200 nm nanowire on 200 nm Si-oxide substrate (simulated)

In figure 8.21, the transport parameter n (charge carrier density), μ (charge carrier mobility) and σ (electrical conductivity) are presented for a n-doped $Bi_2(Te_xSe_{1-x})_3$ nanowire with a diameter of 200 nm in function of the temperature ranging from 77 to 300 K. The charge carrier density n of as deposited nanowires increases with increasing temperature T - as expected for semiconductors. This is due to an increased amount of charge carriers to move to the conduction band, contributing directly to the electrical conductivity. This is consistent with the results presented above with the Seebeck measurement of the nanowire.
The charge carrier mobility decreases with increasing temperature, which is most likely caused by increased phonon-electron scattering processes at higher temperatures. After the thermal treatment of the samples in He atmosphere at 550 K for 2 h, the electrical conductivity σ increases by approximately +50 % (at 78 K) and +22 % at 300 K. This is consistent to the changes observed during annealing presented above (compare fig. 8.13. Although the electrical conductivity decreases in function of the temperature T after the annealing process, the charge carrier density remains proportional to T and the mobility reciprocally proportional to T. Thus, electrical conductivity after the thermal treatment is dominated by the mobility.

The results for p-doped $(Bi_xSb_{1-x})_2Te_3$ nanowire with a diameter of 80 nm in function of the temperature are presented in fig. 8.22. Here, the charge carrier density p also increases with the temperature T and the charge carrier mobility decreases with increasing T.

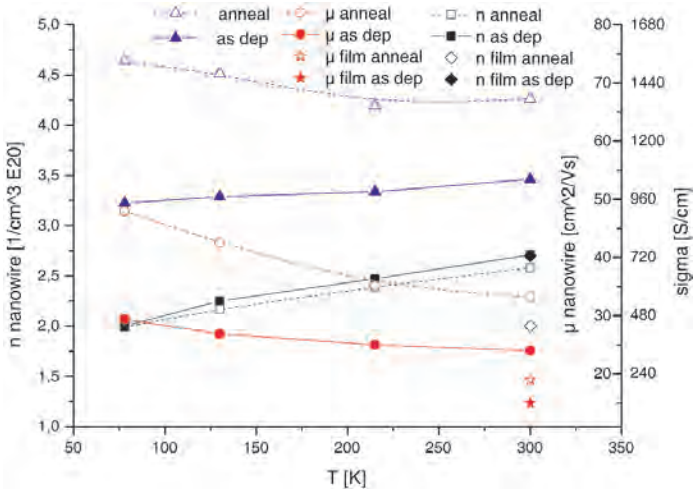

Figure 8.21: Charge carrier density and mobility, electrical conductivity of a $Bi_2(Te_xSe_{1-x})_3$ nanowire with a diameter of 200 nm in function of the temperature

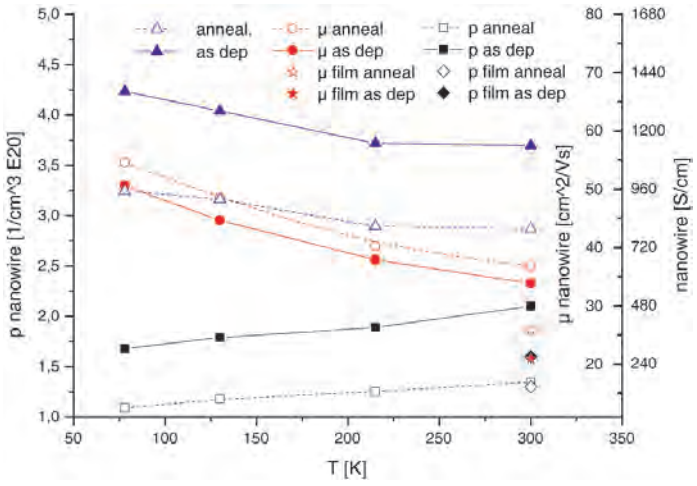

Figure 8.22: Charge carrier density and mobility, electrical conductivity of a $(Bi_xSb_{1-x})_2Te_3$ nanowire with a diameter of 80 nm in function of the temperature

In contrast to n-doped material, the derivation of μ is more negative, thus the electrical conductivity slightly decreases with increasing temperature. This is consistent with the behavior observed in the measurement of S and σ above (compare fig. 8.17). After annealing, the electrical conductivity decreases, this is consistent with the behavior observed above in fig. 8.13. Here, σ still exhibits a reciprocal proportionality with T. Nev-

ertheless, the charge carrier density increases and the mobility decreases with T, indicating a semiconductor-like behavior of the material. After annealing, n exhibits a decrease of approximately -35 % and the mobility increases by about 10 %, indicating an improved crystal structure after the thermal treatment.

8.5 Discussion

The nanowires show a 200 % higher thermoelectric performance compared to the electrodeposited thermoelectric films discussed in chapt. 5 and 6. This is caused by a significantly increased electrical conductivity, which is most likely due to an improved crystal structure and improved orientation. The results obtained for these nanowires are improved about 80-140 % compared to the best reported electrodeposited nanowires in the literature ([MGSP+03] [ZSTB07] [LSZ+08]) and they are comparable to best reported nanocrystalline bulk materials presented in fig. 8.23. The thermopower obtained here is about 62 % the bulk value. Similar to the bulk, the Seebeck coefficient increases up to T about 400 K.
This behavior is expected for metals, since for semiconductors, the charge carrier density n is expected to increase with T and S is reciprocally proportional to n (compare eq. 7.14). Since the electrical conductivity decreases with T, the charge carrier mobility is subject to decrease with T as well. This behavior is consistent to [PHM+08] and the results discussed above with the electrodeposited nanowires. σ exhibits values of about 10 % the value for nanocrystalline bulk.
The more positive derivation of the thermopower S compared to that of bulk material causes an increasing power factor pf (fig. 8.18) and values of almost 50 % the bulk value [PHM+08] [NBKB11]. Based on the results achieved with the annealing in equilibrium Te ambience, the thermoelectric performance of nanostructures thermoelectric material is subject to further improvements due to this thermal treatment.

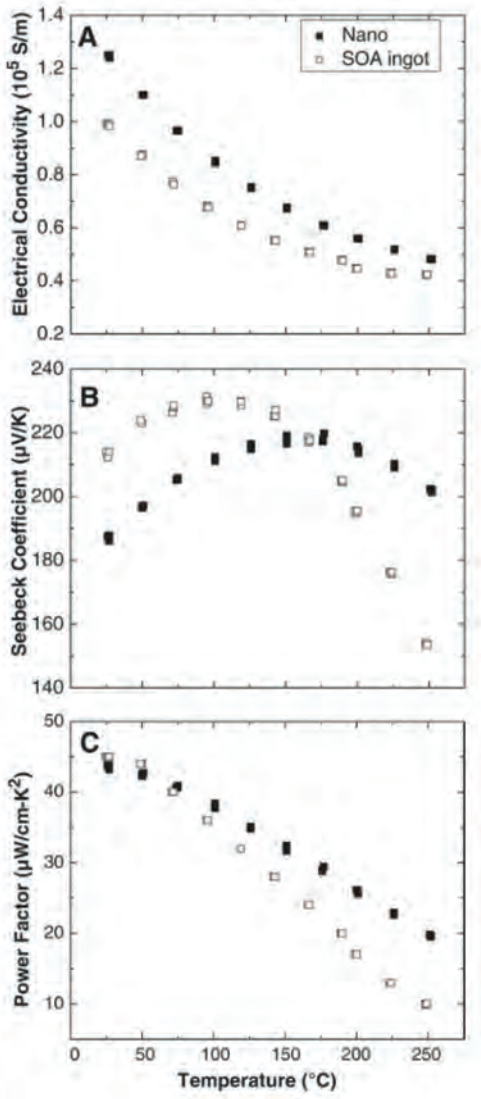

Figure 8.23: Thermoelectric performance of nanocrystalline $(Bi_xSb_{1-x})_2Te_3$ bulk material [PHM+08]; A: electrical conductivity; B: Seebeck coefficient; C: power factor

Chapter 9

Compendium

In this work, a comprehensive study on the electrochemical deposition of thermoelectric n- and p-doped chalcogenide materials has been carried out. High material qualities comparable to those of more cost-intensive deposition methods such as molecular beam epitaxy (MBE) or thermal co-evaporation are realized by electrodeposition technique. Based on the knowledge about the deposition of binary n-doped Bi_2Te_3 given in the literature, the development of binary p-doped Sb_2Te_3 materials has been performed. The influence of chemical and structural parameters such as the composition and the crystal structure on the thermoelectric performance of the deposited materials has been investigated. In order to reach ideal stoichiometry, a close control of the composition has been carried out by highly accurate chemical analysis using various methods such as ICP-OES and EDX. A novel millisecond pulsed electrodeposition technique was applied in order to significantly improve the material quality by improved crystal growth. The deposited materials show good homogeneity in terms of growth, density, and thermoelectric performance. Measurements of parameters contributing to the thermoelectric performance such as σ and S have been performed depending on the temperature in order to understand the behavior of the semiconductor materials.

Further improvements of the deposited materials have been achieved by forced doping using Bi and Se in order to realize ternary compounds. These n-doped $Bi_2(Te_xSe_{1-x})_3$ and p-doped $(Bi_xSb_{1-x})_2Te_3$ materials exhibit improved electrical transport parameters. Thus, the thermoelectric figure of merit of the n-doped ternary compounds significantly improves to 550 % the value of its binary counterparts (compare tab. 7.2).
p-Doped binary Sb_2Te_3 already exhibits a very high quality compared to n-doped Bi_2Te_3. However, further improvement of 133 % have been realized for the p-doped ternary compounds as well.

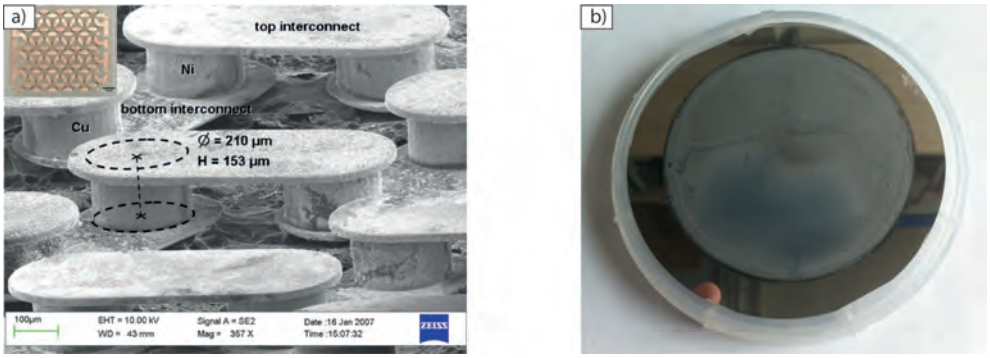

Figure 9.1: (a) SEM image of microstructured thermoelectric generator [GSDH09]; (b) electrodeposited Sb_2Te_3 film on a 4 inch wafer

Although the electrodeposition process has been optimized in order to reach a high and reproducible material quality, the accuracy of chemical composition is still in the order of ± 1-2 %. Further improvement towards ideal composition are realized using a postdeposition thermal treatment in He/Te atmosphere.
Thermal treatment in He atmosphere leads to a +20/35 % (p/n-doped) higher thermoelectric performance due to an improved crystal structure and lowered defect density. Annealing in Te atmosphere is proven to cause further increases towards ideal stoichiometry. Due to a very strong correlation of the thermoelectric performance with the composition of the deposited materials, these improvements in the composition lead to further, significant improvements in the thermoelectric performance of +108 % (n-doped - ZT 0.25) and +42 % (p-doped - ZT 0.4) compared to the electrochemical as-deposited materials (tab. 7.2).

Due to the given geometry of thermoelectric films, the measurement of the thermoelectric performance is limited to the measurement of σ and S in the in-plane direction and the measurement of S and κ perpendicular to the surface. In order to obtain more information about the thermoelectric performance of the deposited materials, a different geometry is realized by the deposition of the optimized materials into porous alumina membranes with pore diameters in the range of 80-200 nm. The thermoelectric nanowires subsequently are used for single-nanowire measurement of S and σ. In order to characterize the behavior of the semiconductor materials, the charge carrier density and mobility are characterized using a nanowire field effective transistor setup. All parameters are determined in function of the temperature. Thus, an investigation of the materials in more detail has been realized. Further analysis of the (temperature dependent) thermal conductivity at single nanowires may

allow for an almost full characterization of the thermoelectric figure of merit in the future.

Due to their optimum working temperature between 300-500 K, the materials developed and characterized in this work are eligible to be used for all kinds of thermoelectric application operating at around room temperature. To date, several approaches of microstructured thermoelectric energy converters (e.g. by Glatz et al. - fig. 9.1 (a)) are expected to be accomplished within the next couple of years. [SGDH08] [GSDH09]

The fabrication of thermoelectric materials by the pulsed millisecond electrochemical deposition method presented in this work may also be extended to other thermoelectric materials of interest, such as lead telluride or skutterudites, which perform best at a different temperature range than Bi_2Te_3 (compare 2.2).

Due to several advantages such as scalability (compare fig. 9.1 (b)), high material quality and low process costs, the electrochemical deposition is suspected to become a practical future alternative for the fabrication of thermoelectric materials.

Appendix A

Appendix

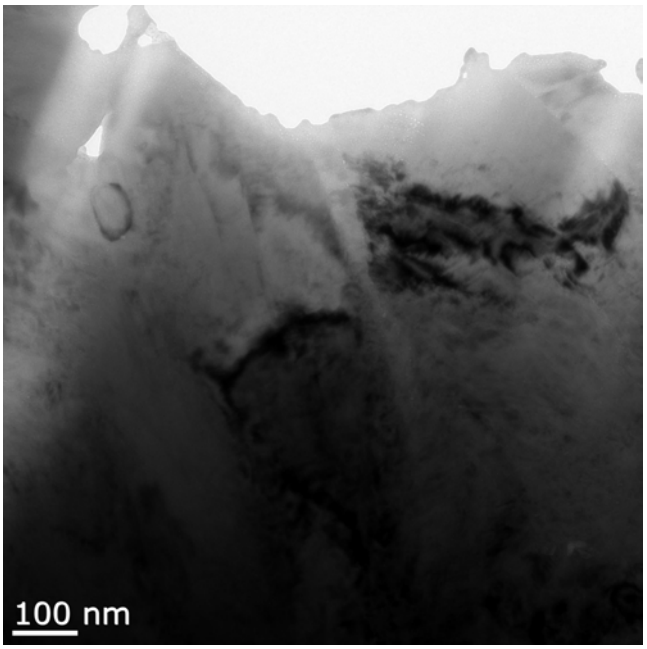

Figure A.1: High resolution TEM image of a n-doped $Bi_2(Te_xSe_{1-x})_3$ film pulsed deposited (10/50 ms) at E=-0.21V vs. Ag/AgCl/KCl (sat.); overview

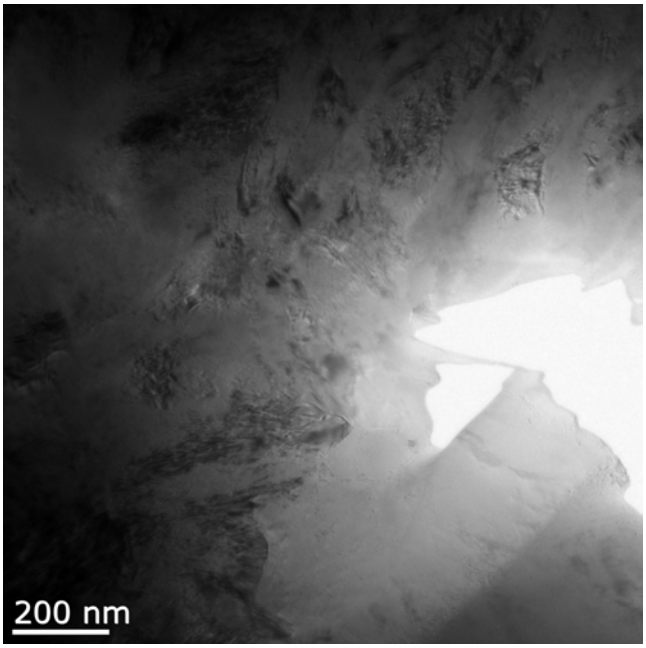

Figure A.2: High resolution TEM image of a n-doped $(Bi_xSb_{1-x})_2Te_3$ film pulsed deposited (10/50 ms) at E=-0.21V vs. Ag/AgCl/KCl (sat.); overview

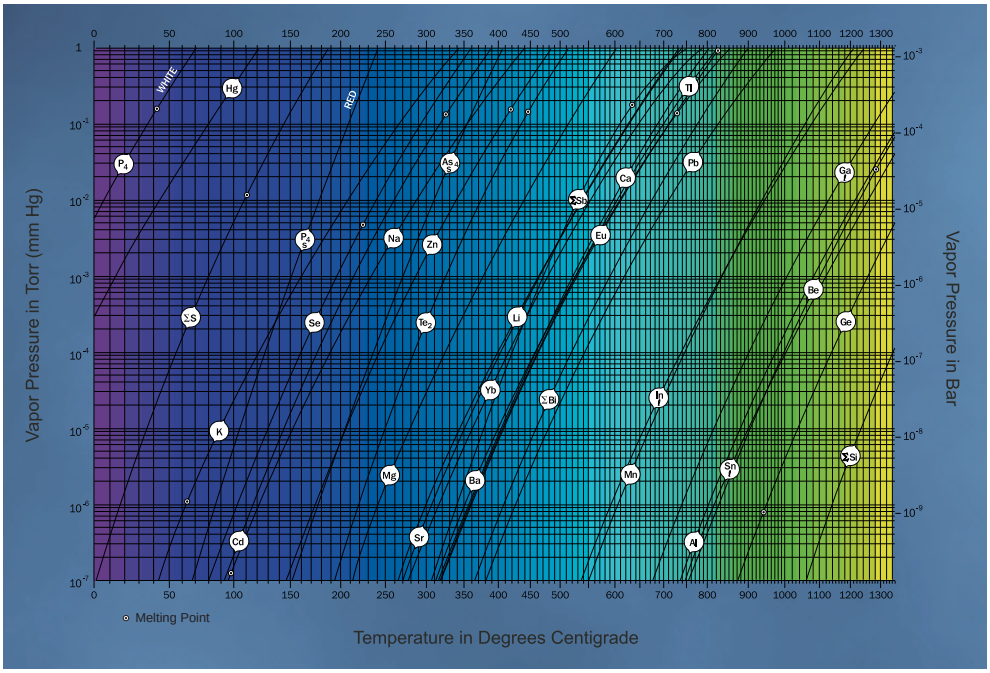

Figure A.3: Vapor pressure chart of Bi, Sb, Te, Se [VEE].

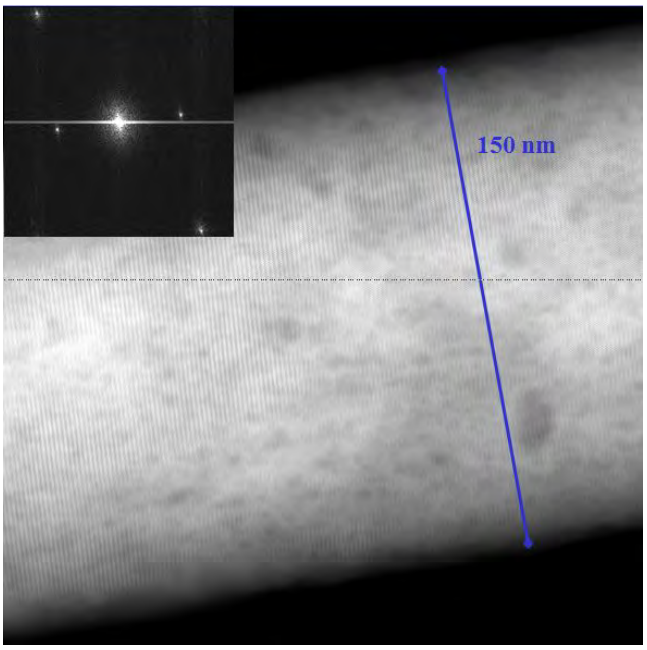

Figure A.4: High resolution TEM image of a $Bi_2(Te_xSe_{1-x})_3$ nanowire with l=40 μm, diam=150 nm; inlay: reflection image

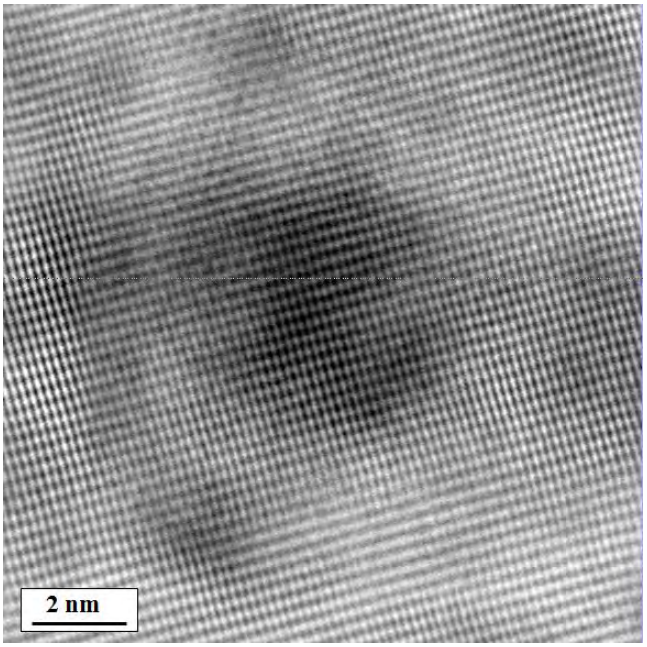

Figure A.5: High resolution TEM image of an area of higher porosity of a $Bi_2(Te_xSe_{1-x})_3$ nanowire with l=40 μm, diam=150 nm

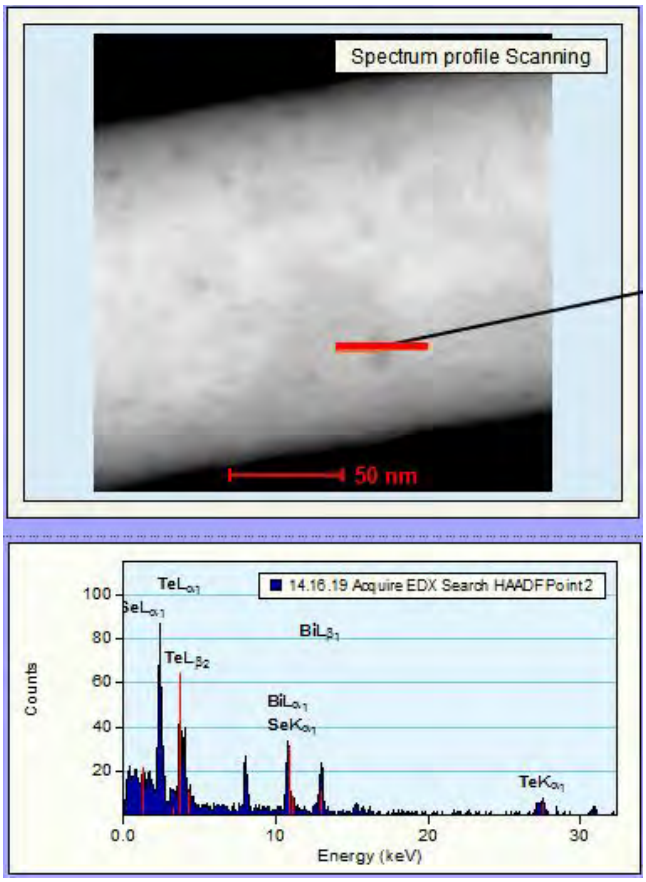

Figure A.6: TEM-EDX image of an area of higher porosity of a $Bi_2(Te_xSe_{1-x})_3$ nanowire with l=40 μm, diam=150 nm

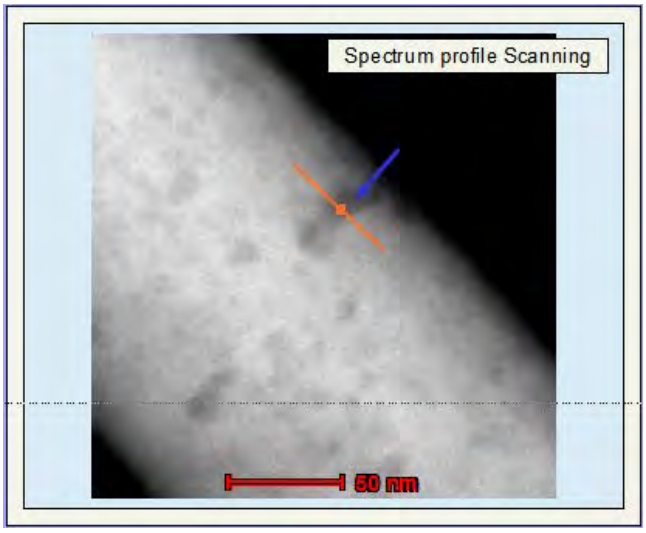

Figure A.7: TEM-EDX image of a $(Bi_xSb_{1-x})_2Te_3$ nanowire with l=40 μm, diam=200 nm

Appendix B

Thanks

I would like to thank all the persons that supported me during this work. First of all, Melanie, Baerbel and Philip who supported me with endurance throughout the whole PhD.
Prof. Kornelius Nielsch for giving me the opportunity and the necessary support to write this thesis. Prof. Julien Bachmann for many discussions and continuous motivation. Prof. Peter Woias as reviewing expert of my thesis. Lewis Akinsinde, Svenja Baessler, Sebastian Zastrow, Tim Boehnert and Johannes Gooth for their patience and continuous support and work. William Toellner for many corrections and remarks.

Appendix C

Publication List

[SRA+12] Christian Schumacher, Klaus G. Reinsberg, Lewis Akinsinde, Sebastian Zastrow, Sonja Heiderich, William Toellner, Geert Rampelberg, Christophe Detavernier, Jose A. C. Broekaert, Kornelius Nielsch, and Julien Bachmann, Optimization of electrodeposited p-doped Sb_2Te_3 thermoelectric films by millisecond potentiostatic pulses, *Advanced Energy Materials*, 2(3):345-352, 2012.

[RSNCB11] Klaus-Georg Reinsberg, Christian Schumacher, Kornelius Nielsch, and Jose Alfons Clement Broekaert. Precision improvements by the use of principal component regression and pooled regression applied to main component determinations with ICP-OES for thermoelectric films, *J. Anal. At. Spectrom.*, 26(12):2477-2482, 2011.

[SRR+12] Christian Schumacher, Klaus G. Reinsberg, Raimar Rostek, Lewis Akinsinde, Svenja Baessler, Sebastian Zastrow, Geert Rampelberg, Peter Woias, Christophe Detavernier, Jose Alfons Clement Broekaert Broekaert, Julien Bachmann, and Kornelius Nielsch. Optimizations of pulsed plated p and n-type Bi2Te3-based ternary compounds by annealing in different ambient atmospheres. *Advanced Energy Materials*, submitted, 2012.

[RSM+12] Klaus-Georg Reinsberg, Christian Schumacher, Katharina Moss, William Toellner, Sonja Heiderich, Kornelius Nielsch, and Jose Alfons Clement Broekaert. Graphite furnace high resolution continuum source atomic absorption spectrometric determination of the main components Bi, Sb and Te in thermoelectric materials sampled as slurries of nanowires. *Spectrochimica Acta Part B*, submitted, 2012.

[RSNCB12] Klaus-Georg Reinsberg, Christian Schumacher, A. Tempez, Kornelius Nielsch and Jose Alfons Clement Broekaert. Depth-profile analysis of thermoelectric layers on Si wafers by glow discharge time-of-flight mass spectrometry. in preparation, 2012.

[RSN+12] Klaus-Georg Reinsberg, Christian Schumacher, Kornelius Nielsch, Jose Alfons Clement Broekaert and Ursula E. A. Fittschen. Investigation on the homogeneity of electrochemically deposited thermoelectric films with synchrotron XRF and XRD, in preparation, 2012.

[SBB+] Christian Schumacher, Tim Boehnert, Svenja Baessler, Klaus G. Reinsberg, and Kornelius Nielsch. Seebeck and transport measurement on p- and n-doped thermoelectric single nanowires, in preparation, 2012

Due to the amount of data obtained during the studies, additionally publications (2-5) are expected to be accomplished during the next couple of months.

Bibliography

[AB02] A. E. Abken and O. J. Bartelt. Sputtered Mo/Sb2Te3 and Ni/Sb2Te3 layers as back contacts for CdTe/CdS solar cells. *Thin Solid Films*, 403:216 – 222, 2002. Proceedings of Symposium P on Thin Film Materials for Photovoltaics.

[AM76] N.W. Ashcroft and N.D. Mermin. *Solid State Physics*. Saunders College, Philadelphia, 1976.

[ANN+01] Hidetaka Asoh, Kazuyuki Nishio, Masashi Nakao, Toshiaki Tamamura, and Hideki Masuda. Conditions for Fabrication of Ideally Ordered Anodic Porous Alumina Using Pretextured Al. *Journal of The Electrochemical Society*, 148(4):B152–B156, 2001.

[BBC+09] A. L. Bassi, A. Bailini, C. S. Casari, F. Donati, A. Mantegazza, M. Passoni, V. Russo, and C. E. Bottani. Thermoelectric properties of Bi-Te films with controlled structure and morphology. *Journal of Applied Physics*, 105(12), 2009.

[BK93] Richard D. Beaty and Jack D. Kerber. *Concepts, Instrumentation and Techniques in Atomic Absorption Spectrophotometry*. Hte Perklin-Elmer Corporation, 2 edition, 1993.

[BKS10] M. Bicer, H. Kose, and I. Sisman. Selective Electrodeposition and Growth Mechanism of Thermoelectric Bismuth-Based Binary and Ternary Thin Films. *Journal of Physical Chemistry C*, 114(18):8256–8263, 2010.

[Bou10] C. Boulanger. Thermoelectric Material Electroplating: a Historical Review. *Journal of Electronic Materials*, 39(9):1818–1827, 2010.

[BPN71] V.G. Bhide, B.A. Patki, and A.S. Nigavekar. X-Ray spectroscopic investigation of bismuth selenide, bismuth tel-

luride and their alloy. *Journal of Physics and Chemistry of Solids*, 32(7):1565 – 1571, 1971.

[Bre69] R. F. Brebrick. Homogeneity Ranges and Te2-pressure Along 3-phase Curves For Bi2Te3(c) and A 55-58-at Percent Te Peritectic Phase. *Journal of Physics and Chemistry of Solids*, 30(3):719–&, 1969.

[BS54] Robert F. Brebrick and Wayne W. Scanlon. Electrical Properties and the Solid-Vapor Equilibrium of Lead Sulfide. *Phys. Rev.*, 96:598–602, Nov 1954.

[BWW07] Luxia Bu, Wei Wang, and Hui Wang. Electrodeposition of n-type Bi2Te3-ySey thermoelectric thin films on stainless steel and gold substrates. *Applied Surface Science*, 253(6):3360 – 3365, 2007.

[BWW08] Luxia Bu, Wei Wang, and Hui Wang. Effect of the substrate on the electrodeposition of Bi2Te(3-y)Sey thin films. *Materials Research Bulletin*, 43(7):1808 – 1813, 2008.

[Che11] Merck Chemicals. Cas 1309-64-4 pdf nr. 107836. CAS, 11 2011. http://assets.chemportals .merck.de/documents/sds/emd/deu/de/1078/107836.pdf.

[DFDS+06] D. Del Frari, S. Diliberto, N. Stein, C. Boulanger, and J. M. Lecuire. Pulsed electrodeposition of (bi1-xsbx)2te-3 thermoelectric thin films. *Journal of Applied Electrochemistry*, 36(4):449–454, April 2006.

[DG58] J.R. Drabble and C.H.L. Goodman. Chemical bonding in bismuth telluride. *Journal of Physics and Chemistry of Solids*, 5(1-2):142 – 144, 1958.

[FDS+05] Doriane Del Frari, Sebastien Diliberto, Nicolas Stein, Clotilde Boulanger, and Jean-Marie Lecuire. Comparative study of the electrochemical preparation of Bi2Te3, Sb2Te3, and (BixSb1-x)2Te3 films. *Thin Solid Films*, 483(1-2):44 – 49, 2005.

[FYX+07] X. A. Fan, J. Y. Yang, Z. Xie, K. Li, W. Zhu, X. K. Duan, C. J. Xiao, and Q. Q. Zhang. Bi2Te3 hexagonal nanoplates and thermoelectric properties of n-type Bi2Te3 nanocomposites. *Journal of Physics D-Applied Physics*, 40:5975–5979, 2007.

[Gol86] H.J. Goldsmid. *Electronic Refrigeration*. Pion, London, 1986.

[Gol09] H.J. Goldsmid. *Introduction to Thermoelectricity*. Materials Science. Springer, 2009.

[Goo11] Johannes Gooth. Thermoelectric Power Factor of InAs Nanowire Field-Effect Transistors. Master's thesis, University of Hamburg, 2011.

[GSDH09] W. Glatz, E. Schwyter, L. Durrer, and C. Hierold. Bi2Te3-Based Flexible Micro Thermoelectric Generator With Optimized Design. *Journal of Microelectromechanical Systems*, 18(3):763–772, 2009.

[HKR08] Q. Huang, A. J. Kellock, and S. Raoux. Electrodeposition of SbTe phase-change alloys. *Journal of the Electrochemical Society*, 155(2):D104–D109, 2008.

[JCP] JCPDS 15-0863 - PDF Bi2Te3. JCPDS.

[JLO06] S. W. Jun, K. Y. Lee, and T. S. Oh. Effects of hydrogen annealing on the thermoelectric properties of electrodeposited Bi2Te3 for nanowire applications. *Journal of the Korean Physical Society*, 48(6):1708–1712, June 2006.

[JM11] Hyunsung Jung and Nosang V. Myung. Electrodeposition of antimony telluride thin films from acidic nitrate-tartrate baths. *Electrochimica Acta*, 56(16):5611 – 5615, 2011.

[JMG98] O. Jessensky, F. Muller, and U. Gosele. Self-Organized Formation of Hexagonal Pore Structures in Anodic Alumina. *Journal of The Electrochemical Society*, 145(11):3735–3740, 1998.

[JPL+10] M. H. Jang, S. J. Park, D. H. Lim, S. J. Park, M. H. Cho, D. H. Ko, M. Y. Heo, H. C. Sohn, and S. O. Kim. Effect of In incorporated into SbTe on phase change characteristics resulting from changes in electronic structure. *Applied Physics Letters*, 96(5):052–112, February 2010.

[JXJ+04] Chuangui Jin, Xiaoqiang Xiang, Chong Jia, Weifeng Liu, Weili Cai, Lianzeng Yao, and Xiaoguang Li. Electrochemical Fabrication of Large-Area, Ordered Bi2Te3 Nanowire Arrays. *The Journal of Physical Chemistry B*, 108(6):1844–1847, 2004.

[KAY+11] Sang Il Kim, Kyunghan Ahn, Dong-Hee Yeon, Sungwoo Hwang, Hyun-Sik Kim, Sang Mock Lee, and Kyu Hyoung Lee. Enhancement of Seebeck Coefficient in Bi0.5Sb1.5Te3 with High-Density Tellurium Nanoinclusions. *Applied Physics Express*, 10.1143:in press, 2011.

[Kit02] Charles Kittel. *Einführung in die Festkörperphysik*. Oldenbourg, München, 13. Auflage edition, 2002.

[KKL+10] Jekaterina Kuleshova, Elena Koukharenko, Xiaohong Li, Nicole Frety, Iris S. Nandhakumar, John Tudor, Steve P. Beeby, and Neil M. White. Optimization of the Electrodeposition Process of High-Performance Bismuth Antimony Telluride Compounds for Thermoelectric Applications. *Langmuir*, 26(22):16980–16985, 2010.

[KO09] Min-Young Kim and Tae-Sung Oh. Electrodeposition and Thermoelectric Characteristics of Bi2Te3 and Sb2Te3 Films for Thermopile Sensor Applications. *Journal of Electronic Materials*, 38:1176–1181, 2009.

[KO10] Min-Young Kim and Tae-Sung Oh. Thermoelectric Characteristics of the Thermopile Sensors with Variations of the Width and the Thickness of the Electrodeposited Bismuth-Telluride and Antimony-Telluride Thin Films. *Materials Transactions*, 51(10):1909–1913, 2010.

[KOK07] M. Y. Kim, T. S. Oh, and J. S. Kim. Annealing behavior of Bi2Te3 thermoelectric semiconductor electrodeposited for nanowire applications. *Journal of the Korean Physical Society*, 50(3):670–676, March 2007.

[Lid92] D. Lide. *CRC Handbook of Chemistry and Physics*. Lide, D., Boca Raton, 73rd edition, 1992. chapt. 4-106.

[Lin] Linseis. Thermal Diffusivity / Thermal Conductivity. http://www.linseis.net.

[LJW09] Fei-Hui Li, Fa-Long Jia, and Wei Wang. Studies of the electrochemical reduction processes of Bi3+, HTeO2+ and their mixtures. *Applied Surface Science*, 255(16):7394 – 7402, 2009.

[LKO09] Su-Kyum Lim, Min-Young Kim, and Tae-Sung Oh. Thermoelectric properties of the bismuth-antimony-telluride

and the antimony-telluride films processed by electrodeposition for micro-device applications. *Thin Solid Films*, 517(14):4199 – 4203, 2009.

[LKRK02] G. Leimkuhler, I. Kerkamm, and R. Reineke-Koch. Electrodeposition of antimony telluride. *Journal of the Electrochemical Society*, 149(10):C474–C478, October 2002.

[LMB+98] A. P. Li, F. Muller, A. Birner, K. Nielsch, and U. Gosele. Hexagonal pore arrays with a 50-420 nm interpore distance formed by self-organization in anodic alumina. *Journal of Applied Physics*, 84(11):6023–6026, 1998.

[LMB+99] An-Ping Li, Frank Muller, Albert Birner, Kornelius Nielsch, and Ulrich Gosele. Fabrication and Microstructuring of Hexagonally Ordered Two-Dimensional Nanopore Arrays in Anodic Alumina. *Advanced Materials*, 11(6):483–487, 1999.

[Lov77] D.R. Lovett. *Semimetals and Narrow Band Gap Semiconductors*. Pion Ltd, London, 1977.

[LSS+08] Woo Lee, Kathrin Schwirn, Martin Steinhart, Eckhard Pippel, Roland Scholz, and Ulrich Gosele. Structural engineering of nanoporous anodic aluminium oxide by pulse anodization of aluminium. *Nat Nano*, 3(4):234–239, April 2008.

[LSZ+08] Shanghua Li, Hesham M. A. Soliman, Jian Zhou, Muhammet S. Toprak, Mamoun Muhammed, Dieter Platzek, Pawel Ziolkowski, and Eckhard Muller. Effects of Annealing and Doping on Nanostructured Bismuth Telluride Thick Films. *Chemistry of Materials*, 20(13):4403–4410, 2008.

[LTS+06] S. H. Li, M. S. Toprak, H. M. A. Soliman, J. Zhou, M. Muhammed, D. Platzek, and E. Muller. Fabrication of nanostructured thermoelectric bismuth telluride thick films by electrochemical deposition. *Chemistry of Materials*, 18(16):3627–3633, August 2006.

[LW09] Feihui Li and Wei Wang. Electrodeposition of BixSb2-xTey thermoelectric thin films from nitric acid and hydrochloric acid systems. *Applied Surface Science*, 255(7):4225 – 4231, 2009.

[MBL96] Pierre Magri, Clotilde Boulanger, and Jean-Marie Lecuire. Synthesis, properties and performances of electrodeposited bismuth telluride films. *J. Mater. Chem.*, 6(5):773–779, 1996.

[MBL+06] E. J. Menke, M. A. Brown, Q. Li, J. C. Hemminger, and R. M. Penner. Bismuth telluride (Bi2Te3) nanowires: Synthesis by cyclic electrodeposition/stripping, thinning by electrooxidation, and electrical power generation. *Langmuir*, 22(25):10564–10574, December 2006.

[MDB+05] S. Michel, S. Diliberto, C. Boulanger, N. Stein, and J. M. Lecuire. Galvanostatic and potentiostatic deposition of bismuth telluride films from nitric acid solution: effect of chemical and electrochemical parameters. *Journal of Crystal Growth*, 277(1-4):274–283, 2005.

[MDS+08] S. Michel, S. Diliberto, N. Stein, B. Bolle, and C. Boulanger. Characterisation of electroplated BiTeSe alloys. *Journal of Solid State Electrochemistry*, 12:95–101, 2008. 10.1007/s10008-007-0362-9.

[MF95] Hideki Masuda and Kenji Fukuda. Ordered Metal Nanohole Arrays Made by a Two-Step Replication of Honeycomb Structures of Anodic Alumina. *Science*, 268(5216):1466–1468, 1995.

[MGPG+02] M. Martin-Gonzalez, A. L. Prieto, R. Gronsky, T. Sands, and A. M. Stacy. Insights into the electrodeposition of Bi2Te3. *Journal of the Electrochemical Society*, 149:C546–C554, 2002.

[MGSP+03] Marisol Martin-Gonzalez, G. Jeffrey Snyder, Amy L. Prieto, Ronald Gronsky, Timothy Sands, and Angelica M. Stacy. Direct Electrodeposition of Highly Dense 50 nm Bi2Te(3-y)Sey Nanowire Arrays. *Nano Letters*, 3(7):973–977, 2003.

[MHO97] Hideki Masuda, Fumio Hasegwa, and Sachiko Ono. Self-Ordering of Cell Arrangement of Anodic Porous Alumina Formed in Sulfuric Acid Solution. *Journal of The Electrochemical Society*, 144(5):L127–L130, 1997.

[MHP+08] Yi Ma, Qing Hao, Bed Poudel, Yucheng Lan, Bo Yu, Dezhi Wang, Gang Chen, and Zhifeng Ren. Enhanced Thermoelectric Figure-of-Merit in p-Type Nanostructured Bismuth

Antimony Tellurium Alloys Made from Elemental Chunks. *Nano Letters*, 8(8):2580–2584, 2008. PMID: 18624384 Bulk Nanograined BiSbTe.

[MLP04] E. J. Menke, Q. Li, and R. M. Penner. Bismuth telluride (Bi2Te3) nanowires synthesized by cyclic electrodeposition/stripping coupled with step edge decoration. *Nano Letters*, 4(10):2009–2014, 2004.

[MSS+03] S. Michel, N. Stein, M. Schneider, C. Boulanger, and J-M. Lecuire. Optimization of chemical and electrochemical parameters for the preparation of Bi2Te2.7Se0.3 thin films by electrodeposition. *Journal of Applied Electrochemistry*, 33:23–27, 2003. 10.1023/A:1022914615625.

[NBKB11] Kornelius Nielsch, Julien Bachmann, Johannes Kimling, and Harald Bottner. Thermoelectric nanostructures: From physical model systems towards nanograined composites. *Advanced Energy Materials*, 1(5):713–731, 2011.

[NCS+02] Kornelius Nielsch, Jinsub Choi, Kathrin Schwirn, Ralf B. Wehrspohn, and Ulrich Goesele. Self ordering Regimes of Porous Alumina: The 10 percent Porosity Rule. *Nano Letters*, 2(7):677–680, 2002.

[NSM+02] M. Nedelcu, M. Sima, A. S. Manea, M. F. Lazarescu, R. V. Ghita, F. Craciunoiu, and T. Visan. Bi(2-x)SbxTe3 thick thermoelectric films obtained by electrodeposition from hydrochloric acid solutions. *Journal of Optoelectronics and Advanced Materials*, 4(1):99–106, March 2002.

[NSW+11] H. P. Nguyen, J. L. Su, Z. Y. Wang, R. J. M. Vullers, P. M. Vereecken, and J. Fransaer. Measurement of Seebeck coefficient of electroplated thermoelectric films in presence of a seed layer. *Journal of Materials Research*, 26(15):1953–1957, August 2011.

[Pan07] Panco. Panco Potential Seebeck Microprobe. http://www.lot-oriel.com/files/downloads/panco/en/psm.pdf, 07 2007.

[Pet] Jens Petersen. Elektrochemie - Grundlagen und analytische Anwendungen. Script.

[PHM+08] Bed Poudel, Qing Hao, Yi Ma, Yucheng Lan, Austin Minnich, Bo Yu, Xiao Yan, Dezhi Wang, Andrew Muto, Daryoosh Vashaee, Xiaoyuan Chen, Junming Liu, Mildred S. Dresselhaus, Gang Chen, and Zhifeng Ren. High-Thermoelectric Performance of Nanostructured Bismuth Antimony Telluride Bulk Alloys. *Science*, 320(5876):634–638, 2008.

[PL90] Jean C Puippe and Frank Leaman. *Pulse-Plating*. Schriftenreihe Glavanotechnik 21. 1 edition, 1990.

[PSMG+01] Amy L. Prieto, Melissa S. Sander, Marisol S. Martin-Gonzalez, Ronald Gronsky, Timothy Sands, and Angelica M. Stacy. Electrodeposition of Ordered Bi2Te3 Nanowire Arrays. *Journal of the American Chemical Society*, 123(29):7160–7161, July 2001.

[PXY+09] K. Park, F. Xiao, B.Y. Yoo, Y. Rheem, and N.V. Myung. Electrochemical deposition of thermoelectric SbxTey thin films and nanowires. *Journal of Alloys and Compounds*, 485(1-2):362 – 366, 2009.

[QYZ+11] W. Qiu, S. Yang, T. Zhu, J. Xie, and X. Zhao. Antimony Telluride Thin Films Electrodeposited in an Alkaline Electrolyte. *Journal of Electronic Materials*, 40:1506–1511, 2011. 10.1007/s11664-011-1647-4.

[RDB10] V. Richoux, S. Diliberto, and C. Boulanger. Pulsed Electroplating: a Derivate Form of Electrodeposition for Improvement of (Bi1-xSbx)(2)Te-3 Thin Films. *Journal of Electronic Materials*, 39(9):1914–1919, 2010.

[Row95] D.M. Rowe. *CRC Handbook of Thermoelectrics*. CRC Press, Boca Raton, 1995.

[Row06] D.M. Rowe. *Thermoelectrics Handbook - Macro To Nano*. CRC Press, Boca Raton, 2006.

[RSM+11] G. Rampelberg, M. Schaekers, K. Martens, Q. Xie, D. Deduytsche, B. De Schutter, N. Blasco, J. Kittl, and C. Detavernier. Semiconductor-metal transition in thin VO(2) films grown by ozone based atomic layer deposition. *Applied Physics Letters*, 98(16):162902, 2011.

[RSM+12] Klaus-Georg Reinsberg, Christian Schumacher, Katharina Moss, William Toellner, Sonja Heiderich, Kornelius Nielsch, and Jose Alfons Clement Broekaert. Graphite furnace high resolution continuum source atomic absorption spectrometric determination of the main components Bi, Sb and Te in thermoelectric materials sampled as slurries of nanowires. *Spectrochimica Acta Part B*, submitted, 2012.

[RSN+12] Klaus-Georg Reinsberg, A. Schumacher, Christian Tempez, Kornelius Nielsch, Jose Alfons Clement Broekaert, and Ursula E. A. Fittschen. Investigation on The Homogeneity of Electrochemically Deposited Thermoelectric Films With Synchrotron XRF and XRD. in preparation, 2012.

[RSNCB11] Klaus-Georg Reinsberg, Christian Schumacher, Kornelius Nielsch, and Jose Alfons Clement Broekaert. Precision improvements by the use of principal component regression and pooled regression applied to main component determinations with ICP-OES for thermoelectric films. *J. Anal. At. Spectrom.*, 26(12):2477–2482, 2011.

[RSNCB12] Klaus-Georg Reinsberg, A. Schumacher, Christian Tempez, Kornelius Nielsch, and Jose Alfons Clement Broekaert. Depth-Profile Analysis of Thermoelectric Layers on Si Wafers by Glow Discharge Time-of-Flight Mass Spectrometry. in preparation, 2012.

[RSW11] Raimar Rostek, Vladimir Sklyarenko, and Peter Woias. Influence of vapor annealing on the thermoelectric properties of electrodeposited Bi2Te3. *Journal of Materials Research*, 26:1785–1790, August 2011.

[SBB+] Christian Schumacher, Tim Boehnert, Svenja Baessler, Klaus G. Reinsberg, and Kornelius Nielsch. Seebeck and Transport Measurement on p- and n-doped Thermoelectric Single Nanowires. in preparation.

[SGDH08] E. Schwyter, W. Glatz, L. Durrer, and C. Hierold. Flexible Micro Thermoelectric Generator based on Electroplated Bi(2+x)Te(3-x). *DTIP of Mems and Moems*, 2008.

[SGSS03] M. S. Sander, R. Gronsky, T. Sands, and A. M. Stacy. Structure of bismuth telluride nanowire arrays fabricated by electrodeposition into porous anodic alumina templates. *Chemistry of Materials*, 15(1):335–339, January 2003.

[SOV+10] Marcus Scheele, Niels Oeschler, Igor Veremchuk, Klaus-Georg Reinsberg, Anna-Marlena Kreuziger, Andreas Kornowski, Jose Broekaert, Christian Klinke, and Horst Weller. ZT Enhancement in Solution-Grown Sb(2-x)BixTe3 Nanoplatelets. *ACS Nano*, 4(7):4283–4291, 2010.

[SRA+12] Christian Schumacher, Klaus G. Reinsberg, Lewis Akinsinde, Sebastian Zastrow, Sonja Heiderich, William Toellner, Geert Rampelberg, Christophe Detavernier, Jose A. C. Broekaert, Kornelius Nielsch, and Julien Bachmann. Optimization of Electrodeposited p-Doped Sb2Te3 Thermoelectric Films by Millisecond Potentiostatic Pulses. *Advanced Energy Materials*, 2(3):345–352, 2012.

[SRR+12] Christian Schumacher, Klaus G. Reinsberg, Raimar Rostek, Lewis Akinsinde, Svenja Baessler, Sebastian Zastrow, Geert Rampelberg, Peter Woias, Christophe Detavernier, Jose Alfons Clement Broekaert Broekaert, Julien Bachmann, and Kornelius Nielsch. Optimizations of pulsed plated p and n-type Bi2Te3-based ternary compounds by annealing in different ambient atmospheres. *Advanced Energy Materials*, submitted, 2012.

[SS59] Karel Smirous and Ladislav Stourac. Feste Loesungen von Bi2Te3 und Sb2Te3 als p-leitende Werkstoffe fuer Halbleiter-Thermoelemente. *Zeitschrift fuer Naturforschung*, 14a:848–849, 1959.

[ST08] G. Jeffrey Snyder and Eric S. Toberer. Complex thermoelectric materials. *Nat Mater*, 7(2):105–114, February 2008.

[STOa] STOE. XRD Patterns PDF 49-1713. PKS-2.01.

[STOb] STOE. XRD Patterns PDF 50-954. PKS-2.01.

[TBP+03] K. Tittes, A. Bund, W. Plieth, A. Bentien, S. Paschen, M. Plotner, H. Grafe, and W. J. Fischer. Electrochemical deposition of Bi2Te3 for thermoelectric microdevices. *Journal of Solid State Electrochemistry*, 7(10):714–723, 2003.

[TP07] Kerstin Tittes and Waldfried Plieth. Electrochemical deposition of ternary and binary systems from an alkaline electrolyte - a demanding way for manufacturing p-doped bismuth and antimony tellurides for the use in thermoelectric elements. *Journal of Solid State Electrochemistry*, 11:155–164, 2007.

[TXL+07] Xinfeng Tang, Wenjie Xie, Han Li, Wenyu Zhao, Qingjie Zhang, and Masayuki Niino. Preparation and thermoelectric transport properties of high-performance p-type Bi2Te3 with layered nanostructure. *Applied Physics Letters*, 90(1):012102, 2007.

[vdP58] L.J. van der Pauw. A method of meauring specific resistivity and Hall effect of discs of arbitrary shape. *Philips Research Reports*, 13(13):1–9, 1958.

[VEE] VEECO. Vapor Pressure Chart 1. Technical report, VEECO.

[XHY+08] F. Xiao, C. Hangarter, B. Yoo, Y. Rheem, K. H. Lee, and N. V. Myung. Recent progress in electrodeposition of thermoelectric thin films and nanostructures. *Electrochimica Acta*, 53(28):8103–8117, 2008.

[XTY+09] Wenjie Xie, Xinfeng Tang, Yonggao Yan, Qingjie Zhang, and Terry M. Tritt. Unique nanostructures and enhanced thermoelectric performance of melt-spun BiSbTe alloys. *Applied Physics Letters*, 94(10):102111, 2009.

[XYLM07] F. Xiao, B. Y. Yoo, K. H. Lee, and N. S. V. Myung. Electrotransport studies of electrodeposited (Bi(1-x)Sbx)(2)Te(3) nanowires. *Nanotechnology*, 18(33):335203, 2007.

[YHSX04] J. H. Yuan, F. Y. He, D. C. Sun, and X. H. Xia. A Simple Method for Preparation of Through-Hole Porous Anodic Alumina Membrane. *Chemistry of Materials*, 16(10):1841–1844, 2004.

[YPM+10] Xiao Yan, Bed Poudel, Yi Ma, W. S. Liu, G. Joshi, Hui Wang, Yucheng Lan, Dezhi Wang, Gang Chen, and Z. F. Ren. Experimental Studies on Anisotropic Thermoelectric Properties and Structures of n-Type Bi2Te2.7Se0.3. *Nano Letters*, 10(9):3373–3378, 2010.

[Zas10] Sebastian Zastrow. Aufbau einer Hochtemperatur-Messanlage zur Charakterisierung der elektronischen Transporteigenschaften von thermoelektrischem Material auf Basis von Indium-gefüllten Kobalt-Antimon-Skutteruditen. Master's thesis, 2010.

[Zeh11] B. V. Zehgbroeck. *Principles of Semiconductor devices.* 2011.

[ZSTB07] Alexandre Zimmer, Nicolas Stein, Herman Terryn, and Clotilde Boulanger. Optical and thermoelectric characterizations of electroplated n-Bi2(Te0.9Se0.1)3. *Journal of Physics and Chemistry of Solids*, 68(10):1902 – 1907, 2007.

List of Figures

List of Tables

List of Acronyms

AC	Alternating Current
ALD	Atomic Layer Deposition
CV	Cyclovoltamogramm
DAUP	Diaminoura Polymer
DOS	Density of States
EDX	Energy Dispersive X-Ray Spectroscopy
Fig.	Figure
FWHM	Full Width Half Maximum
GD-TOF-MS	Glow-Discharge Time Of Flight-Mass Spectrometry
GF-AAS	Graphite Furnace Atomic Absorption Spectrometry
ICP-OES	Inductively Coupled Plasma-Optical Emission Spectrometry
IR	Infrared
ITO	Indium Tin Oxide
LSR	Linseis Seebeck and Electric Resistivity Unit
MBE	Molecular Beam Epitaxy
MOSFET	Metal-Oxide Field-Effect Transistor
NFET	Nanowire Field-Effect Transistor
NW	Nanowire
OCP	Open Circuit Potential
PLD	Pulsed Laser Deposition
PSM	Potential Seebeck Microprobe
SEM	Scanning Electron Microscope
SIMS	Secondary Ion Mass Spectrometry
Tab.	Table
TAGS	Thermoelectric Materials based on Te, Sb, Ge, Ag
TDTR	Time Domain Thermo-Reflectance measurement
TEG	Thermoelectric Generator
TEM	Transmission Electron Microscopy
UPD/OPD	Underpotential/Overpotential Deposition
XRD	X-Ray Diffraction

List of Symbols

A	Area
$\mathring{A}$	Angstrom
a	Lattice (Cell) Vector
a_i	Chem. Activity
a(T)	Thermal Diffusivity
α	Rhombohedral Angle
b	Sample Distance
b_0	Reciprocal Lattice Vector
β	Cell Angle
C	Capacitance
C_p	Specific Heat
c	Lattice (Cell) Vector
D	Distance from Film's Border
d	Distance
E_f	Fermi Energy
E_g	Energy of Band Gap
E	Chem: Cell Potential
e	Electron's Charge
F	Chem: Faraday Konstante=96485,33 C/Mol
F(E)	Fermi Distribution
G	Chem: Gibbs Energy
G(E)	Density of States
g	Optical Absorption Length
h	Planck's Constant
$\hbar$	Planck's Constant
h,k,l	Millers Indexes
I	Current
I_R	XRD Intensity
k_B	Boltzmann's Constant

$\vec{k_e}$	Wave Vecto Electrons
$\vec{k_h}$	Wave Vecto Holes
κ	Thermal Conductivity
L	Lorentz Number
L_i	Fermi Dirac Integral Coefficients
l	Length
λ	Wavelength (X-Ray - XRD)
M	Chem: Molaric
m^*	Effective Mass
n	Charge Carrier Censity (electrons)
o	Spot Size of Laser Pulse
p	Charge Carrier Density (holes)
Q	Heat
R	Resistance/Resistivity
R_F	Reflectance
$\vec{r}$	Position Vector
ρ(T)	Density
S	Seebeck Coefficient
σ	Electrical Conductivity
T	Temperature
t	Time
Δ T	Temperature Difference
τ_e	Relaxation Time
Θ	Reflection Angle (XRD)
Θ_1	Angle Between Γ_A and Γ_Y
Θ_2	Angle Between Γ_D and Γ
U	Voltage
ΔU	Potential Difference
V	Volt
V	Cell: Unit Cell Volume
W	Watt
ω	Frequency
Z	Thermoelectric Figure of Merit
ZT	Thermoelectric Figure of Merit (T dependent)
z_i	Chem: Charge of Ions
υ	Velocity
υ_i	Chem: Type of Ions
Γ_A	Lattice Cell Vector
Γ_D	Lattice Cell Vector

Γ_Z	Lattice Cell Vector
μ	Charge Carrier Mobility
μ_i	Chemical Potential
μ_i^0	Chemical Standard Potential
ϕ_i	Chem: Electric Potential
Π	Peltier Coefficient
χ	Reduced Energy

Appendix D

Versicherung an Eides statt

Ich versichere an Eides statt, dass ich die Inanspruchnahme fremder Hilfen aufgeführt habe, sowie, dass ich die wörtlich oder inhaltlich aus anderen Quellen entnommenen Stellen als solche kenntlich gemacht habe.

Hamburg, den 04. April 2012

(Christian Schumacher)